UNIVERSITY OF CANTERBURY

Department of Physics and Astronomy

CHRISTCHURCH NEW ZEALAND

A thesis submitted in partial fulfillment of requirements for the Degree of Master of Science in Medical Physics in the University of Canterbury, New Zealand

by

Ekta Jhala

Investigation of Dosimetric Characteristics and Exploration of Potential Applications of Amorphous Silicon Detector

Ekta Jhala

Year: 2004-2006

MSc Supervisors:
Assoc. Prof. Lou Reinisch, Lynne Greig & Anthony Johnson

Abstract

The ability of the electronic portal imaging device (EPID) to acquire a large two-dimensional array of digitized x-ray data in real time is extremely attractive for dosimetric measurements. To evaluate the potential use of an EPID for portal dose measurement in Wellington Blood and Cancer Centre, some dosimetric characteristics of the Varian's PortalVision^{TM} aS500 were investigated. PortalVision^{TM} incorporates an amorphous silicon detector (aSi) . Some potential applications of EPID in linac QA were also explored.

The EPID's performance for linearity with MU and dose rate was verified and it was found to be proportional over the entire measured range. Short term repeatability was found to be excellent. An investigation of calibration method to improve dosimetric accuracy demonstrated two methods of avoiding detector saturation. Firstly, acquiring flood field with the use of additional buildup and secondly, increasing the source to detector distance for calibration. A study of EPIDs behaviour under conditions of varying dose rate which commonly arise in EDW treatment techniques was carried out. The EPID exhibited a field size dependence in addition to a 8% discrepancy on the 'hot edge' of EDW profiles. Further investigation into the field size dependence and the discrepancy at hot edge is required. EPIDs ability to acquire asymmetric field profile was also investigated. The profiles acquired using EPID deviated in shape and magnitude by upto 16% from the ion chamber profiles.

Some potential applications of EPID to perform QA of linac beam properties, its ability to perform optical and mechanical linac QA have been explored. The EPID's capability to give constant output, flatness, symmetry, wedge angle and wedge factors with high level of accuracy and reproducibility was demonstrated. EPID was also found to be objective, efficient and feasible for performing optical linac QA. The use of EPID for linac QA could be simplified by improving the available software analysis tools thus making it more efficient.

"There is no region of regret when the dose you see is the dose you get. "(Peter Metcalfe 1994)

Acknowledgement

A journey is easier when you travel together. This thesis has been a 2 year long journey, whereby I had the honour of being accompanied and supported by many people. It is a pleasure to now get an opportunity to acknowledge and appreciate all those efforts that went into the completion of this work. This is perhaps the easiest and the hardest bit that I have to write. It is easy to remember and name all the people that helped to get this done but to express in words the enormous gratitude I owe, is impossible. I will nonetheless try.

I owe an enormous debt of gratitude to my supervisor Assoc. Prof. Lou Reinisch; for his unstinting commitment to help see this project through to its final completion, and his equally generous and wise guidance during its development. His efforts and willingness to travel between cities to ascertain the progress inspite of his busy travel itineraries and hectic schedules were endless. His constant encouragement to innovative thought process was a great motivator.

It is difficult to overstate my gratitude to my co-supervisor Lynne Greig, Chief Physicist at Wellington Blood and Cancer Centre (WBCC). Her knowledge, ideas, perceptiveness and analytical approach were vital to the completion of this thesis. Her critical sense, integral view on research and strive for perfection has made this thesis a work of art. Her suggested revision has made this thesis coherent and concise. But not even she could remove all of 'Ekta's vaguities' (as she termed them) from the thesis.

The episode of acknowledgement would not be complete without the mention of Anthony Johnson, senior physicist, WBCC, my clinical supervisor during the first year of this thesis. He was the prime mover of this project providing continual support in laying the foundation, opening doors to a wealth of knowledge and a thirst for learning more.

I am deeply indebted to Dr. Peter Greer and Dr. Randall Holt for their valuable input and suggestions during the tenure of this thesis. Their willingness to support and accommodate me in their hectic schedule is most appreciated.

I would also like to extend my gratitude to Varian Medical Systems, especially engineers Peter Williams and John Paisley for their continual support in resolving technical issues.

My colleagues have provided constant support, their willingness to share their knowledge is highly appreciated. I express my sincere thanks to Bryn Currie for the endless discussions, his great companionship and making the environment conducive to research. Other colleagues and staff at WBCC have been of utmost help in every way.

I wish to record the lasting gratitude that I owe to my loving family who taught me the value of hard work, their constant encouragement and motivation despite all odds was an essential ingredient for my successful completion and I hope to do them proud someday.

I feel a deep sense of love and gratitude for my surrogate family Dr. Rob McIlroy and Nemu Lallu for customising me to the New Zealand culture, teaching me work ethics and making this foreign city a home away from home.

Lastly, I acknowledge with appreciation the love and care of my many friends, especially Madhusudan Vasudevamurthy, who created a an environment with a strange balance of love, affection, heated discussions and passionate arguments, for truth springs from arguments with friends and personalities develop from the thrust of debate.

It is good to have an end to a journey, but it is the journey that matters in the end.

Contents

Figures

Tables

Nomenclature

Active matrix flat panel imaging	AMFPI
Amorphous silicon	aSi, a-Si
Analogue to digital converter	ADC
Beams eye view	BEV
Build up	BU
Calibrated units	CU
Central axis	CAX
Computed tomography	CT
Dark field	DF
Dose rate servo	DRS
Dosimetric portal image caluculation algorithm	DPIC
Electronic portal imaging device	EPID
Enhanced dynamic wedge	EDW
External beam therapy	EBT
Flood field	FF
Frame processing board	FPB
Golden segmented treatment table	GSTT
Gun pulse repetition frequency	GPRF
Image acquisition system	IAS
Imager vertical	img vrt
Imager longitudinal	img lng
Intensity modulated radiation therapy	IMRT
Inverse square law	ISL
Linear accelerator	Linac
Megavoltage computed tomography	MVCT
Monitor units	MU
Position readout	PRO
Predicted dose image	PDI
Pulse drop servo	PDS

Pulse frequency servo	PFS
Pulse length servo	PLS
Pulse rate frequency	PRF
Quality assurance	QA
Region of interest	ROI
Repetition rate	Rep rate
Segmented treatment table	STT
Signal to noise ratio	SNR
Source to detector distance	SDD
Source to surface distance	SSD
Thermoluminescent detector	TLD
Thin film transistor	TFT
Treatment planning system	TPS
Universal control board	UCB
Wellington blood and cancer centre	WBCC

Chapter 1

Introduction

This chapter discusses the project in a broader perspective and spells out its niche in radiation therapy. It also justifies the use of EPID for geometric and dosimetric verification.

1.1 Background

Cure of cancer patients require inactivation of all tumour cells of the primary lesion and if present, all regional and distant disease. Failure to eradicate the primary tumour will result in the death of the patient unless salvage treatment is effective, available and applied. Radiation therapy is a key treatment modality for cancer. One goal of radiation therapy is to maximize the radiation dose to a well defined target volume of the tumour while attempting to minimize the dose to the surrounding healthy tissue or organs. This results in eradication of disease, or improvement in quality of life for some terminally ill patients. High dose conformal therapy techniques are increasingly being used for tumor eradication, the success of which depends critically on the accuracy of treatment delivered.

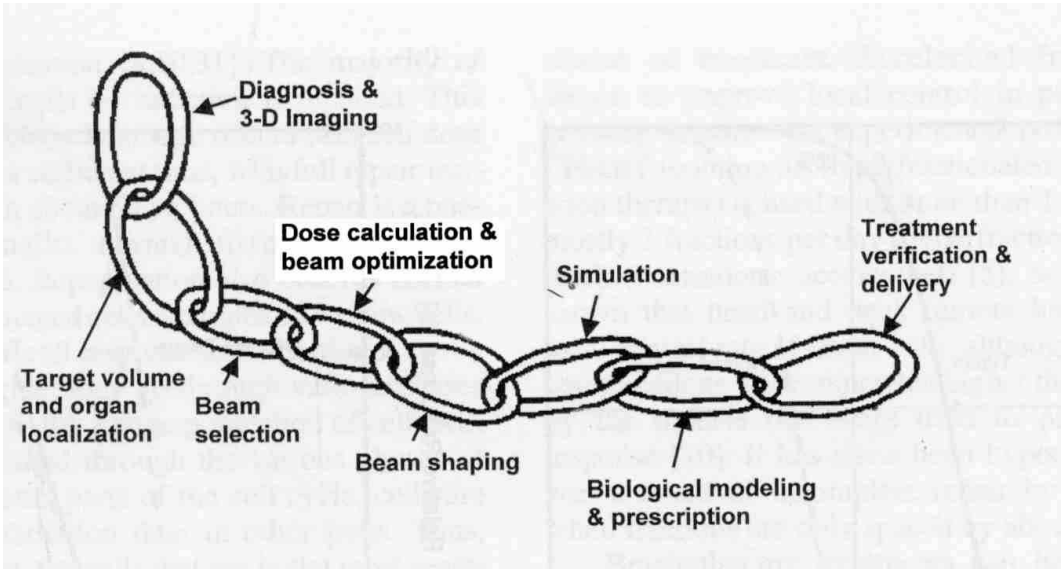

Figure 1.1: The various steps in treatment planning process represented by links in a chain [1].

The process of radiation therapy is complicated and involves many steps. Figure 1.1 explains the stages involved in a treatment planning process. A number of uncertainties are introduced at every step in the process of planning and delivery of treatment, which makes treatment verification a crucial step in ensuring accurate treatment delivery.

1.2 Treatment verification

A number of geometric and dosimetric inaccuracies introduced in the process of planning and treatment delivery could compromise clinical outcome. Errors due to some of these uncertainties could be prevented while others have to be accepted. Some uncertainties [2] in the treatment delivery may include the following:

1. Uncertainties in the position and extent of the target volume.
2. Inaccuracies in the treatment planning systems dose-calculation algorithm.
3. Inaccuracies in the calibration of linear accelerator.
4. Inaccuracies in the mechanical alignment of the treatment machine.
5. Inaccuracies in patient set-up.
6. Patient movement.
7. Variability of the patients internal anatomy.

Thus, to reduce the amount of uncertainties from affecting the clinical outcome a treatment verification program is necessary. A comprehensive treatment-verification programme should include the verification of dose, verification of field position, and verification that the correct treatment machine parameters are set.

1.2.1 Geometric treatment verification

The success of radiation therapy depends critically on the accuracy of patient alignment in treatment position day after day. Therefore, patient positioning is verified before treatment delivery. Traditionally film has been the gold standard for geometric verification of patient positioning due to its high spatial resolution. However, significant set-up and treatment delivery errors have been reported in film-based portal imaging studies [3, 4, 5, 6, 7] and it has been suggested that an increase in imaging frequency is associated

with improved clinical outcome [8]. Film imaging is time consuming, labour intensive and thus reduces the patient throughput in a busy department. In addition, motion during treatment and day-to-day variations are not recorded with weekly imaging. Furthermore, the non-digital format of imaging system introduces the subjective nature of visual analysis in quantitative interpretation of geometric discrepancies making it difficult and tedious.

The advent of electronic portal imaging device (EPID) helped overcome these issues and soon replaced film. However, images produced using high energy x-rays are often unsuitable for verification purposes due to their low contrast. To solve this problem, different imaging systems were developed. The earliest EPID systems were cumbersome to operate, lacked the spatial resolution of film, but already demonstrated improved contrast resolution over film [9]. Early array systems used diodes, scintillator or liquid based ion chambers. Early fluoroscopic systems were precursors of screen-mirror systems. Recently developed amorphous silicon (aSi) system offers better resolution and faster response.

Due to the significant advancement of aSi EPID in image quality over film [10, 11], dose saving acquisition mode [12] and all the other advantages EPID offers, it has been widely accepted as a film replacement. Conclusions from early studies were that EPID was in general as good as film in delivering localization quality images. They are better than film imaging with respect to acquisition speed and the potential to use computer aided analysis. For these reasons, electronic portal imaging has become an important tool in radiation therapy, in that it offers the ability to verify the accuracy of patient set-up in a quick and convenient manner.

1.2.2 Dosimetric verification

Verifying the distribution of dose delivered to the patient is vital to ensure that the patient recieves the planned high dose to the tumor volume and minimal dose to the surrounding structures. With increasing complexity in intensity modulated radiotherapy (IMRT) plans, the verification of dose distribution becomes critical to successful clinical outcome. Conventional practices of dosimetric verification consists of placing detectors such as thermoluminescent dosimeters (TLD) or diodes, on the entry or exit surface of the patient. However, these detectors could only measure point doses and could not be used for measurement of the entire dose distribution of a field. In addition, the implementation of this type of verification could be limited by time and labour required to place properly the dosimeters and analyze the data. It is only natural for researchers to be highly inter-

ested in developing a simple method for dosimetric verification that would give the entire dose distribution. Much effort has been devoted over the last several years to expand the use of megavoltage imaging to include dosimetric applications. Many researchers have been working on the subject, the following are only few of the many references found [13, 14, 15, 16, 17, 18, 19, 20, 21]. With the advent of amorphous silicon EPIDs the possibility seems more viable than ever before because of their ease of deployment, positional accuracy, large number of measurement points, and automated signal digitization.

Although originally designed for imaging, the ability of the EPID to acquire rapidly a large two-dimensional array of digitized x-ray data is extremely attractive for dosimetry measurements. Studies have demonstrated a stable dose-response [22] of the detector that is independent of dose rate and linear with integrated dose [23, 24]. Later dosimetric properties of EPID have proved its worth over film and other dosimetry systems [25, 26, 27, 28, 29, 30].

Dosimetric treatment verification using EPID can potentially be approached via two ways. Firstly, a simple yet effective way which has been discussed by Leong et al. [13] is a direct comparison between measured portal dose image with a theoretically predicted portal dose image at the plane of the detector. Another dosimetric treatment verification application of EPID involves back-projecting the primary component of the measured portal dose image after removal of scatter through the patient computed tomography (CT) data set. This allows a calculation of deposited dose in the patient. Other simpler ways of relating the measured portal image to the patient mid-plane or exit dose estimates have also been studied by researchers [17, 18, 31].

All of these dosimetric verification methods require the scatter to be removed from the measured portal image. Rather, the primary component of the beam to be separated from the scatter component for independent computation. This makes it very complicated for small conformal IMRT segments, especially due to the large air-gaps present between the patient and the detector. Although, many researchers have developed effective and accurate algorithms, and the advantages of online 2D dosimetric verification are obvious, portal dosimetry using EPID has still not been widely used clinically. One of the reasons for its limited use being the need to develop in-house algorithms for prediction of dose images, since these options are not yet widely available in commercial treatment planning systems. However, development of such an algorithm is beyond the scope of this thesis. It could be several years before such a product could be developed

and feasible for clinical use. A better understanding of the dosimetric characteristics is required for the development of an efficient and effective algorithm. Many researchers have studied the dosimetric characteristics of aSi detector but certain issues still need to be resolved. Hence, we propose to investigate some of the dosimetric characteristics of Varian's PortalVision^{TM} aS500. In particular, study the effect of calibration distance on dosimetric accuracy, EPIDs behaviour under conditions of varying dose rate and its ability to acquire asymmetric fields. Its linearity with Monitor Units (MU) and dose rate were confirmed and short term repeatability verified.

1.3 Other potential applications

Apart from geometric and dosimetric verification of treatment delivery, EPIDs are being used for measuring transmission through multileaf collimators (MLC), verifying the leaf position accuracy of MLC and also physical quality assurance (QA) of linear accelerator (linac).

Asi EPIDs have demonstrated their stable dose response making them an attractive option for QA of linac beam properties. In this thesis, we investigate its use for measuring output constancy of linac, flatness and symmetry of the beam, EDW factors and also wedge angle constancy for EDW fields.

Due to all the advantages offered by EPIDs over film, film is rapidly being phased out from clinical imaging making wet processing redundant in the process. In such an environment, holding on to the wet processor and films only for linac QA becomes highly inefficient and wasteful of resources. Hence developing linac QA tests using EPID becomes essential. EPIDs have already been employed for some aspects of linac QA in many centres [32, 33]. However, to date their primary clinical use has been in geometric verification of patient positioning. At Wellington Blood and Cancer Centre (WBCC) also, the current use of EPID has been only for geometric treatment verification. Hence, development of tests using EPID to enable reduced film dependence and phase out the wet processor, formed one aspect of this thesis. We have explored some potential applications of EPID to study its feasibility as a QA tool to verify the coincidence of light field vs radiation field, verify the calibration of independent jaws and also verify the radiation isocentre.

To summarise, this thesis is an investigation of portal dosimetry with an aim to better

understand some dosimetric characteristics of an aSi detector. We will also explore some of its potential applications as a tool for linac QA. In the following chapter we will discuss the construction of the imager in order to gain more insight on its working and behaviour. We will also give a brief overview of implementing portal dosimetry at WBCC. Following these the experimental methods used for our studies will be detailed, results presented with discussions and conclusions.

Chapter 2

PortalVision^{TM} aS500 Electronic Portal Imaging Device

2.1 Background

The electronic portal imaging began in 1980's with the advent of fluoroscopic systems used to acquire megavoltage transmission images. The scanning liquid ionization chamber system was soon introduced, followed by camera-based fluoroscopic EPID's from various manufacturers. These devices did not meet the standard required for imaging, due to a number of limitations in existing technology. Poor resolution, image quality, high dose required for imaging were some of the factors hindering their usefulness. In recent years, with the development of the active-matrix flat panel display technology a number of applications in the medical imaging devices have evolved. Active matrix flat panel imaging (AMFPI) is a unique technology incorporated in aSi detectors which will be discussed in detail in the following sections.

2.2 Technology of aSi detectors

The flat panel imaging devices are developed in two forms, amorphous silicon and amorphous selenium arrays. Since the EPID used in this study is an amorphous silicon (aSi) EPID, amorphous selenium will not be discussed further.

A-Si arrays are large area integrated circuits (Figure 2.1) called active-matrix arrays fabricated from aSi, a material which exhibits high resistance to radiation damage. Active-matrix technology allows the deposition of semiconductors, across large-area substrates in a well-controlled fashion such that the physical and electrical properties of the resulting structures can be modified and adapted for many different applications. Coupling traditional x-ray detection materials as phosphor or photoconductor with a large-area active-matrix readout structure forms the basis of flat-panel x-ray imagers.

The aSi is deposited onto a thin substrate (typically 1mm thick glass) using semicon-

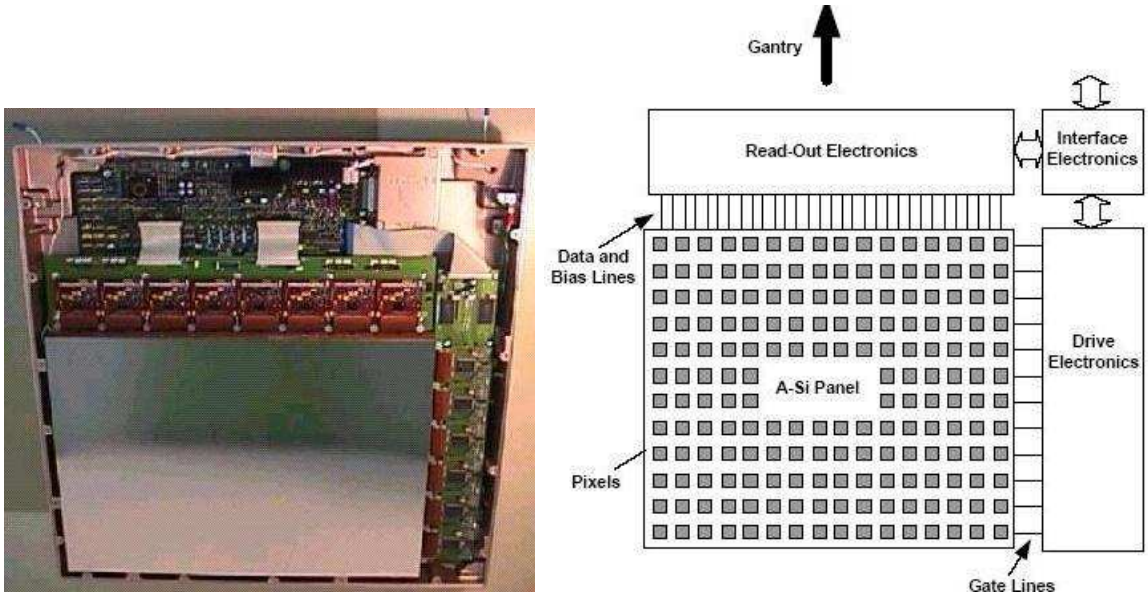

Figure 2.1: aSi electronic portal imager (Reproduced from Varian document library [34])

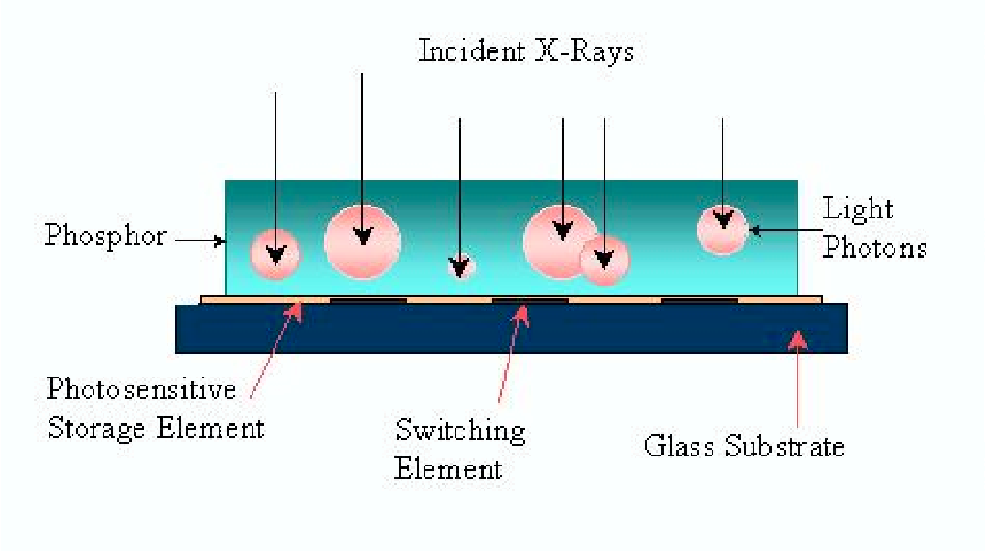

Figure 2.2: Indirect detection approach (Reproduced from J. Pouliot web tutorial on EPID [35])

ductor fabrication techniques, such as plasma enhanced chemical vapour deposition, to form a two dimensional matrix of thin film transistors (TFTs) and photodiodes. These integrated circuits form a thin, large-area light sensor, which, because the arrays have direct contact with the metal plate/phosphor screens form the x-ray detector for the EPID.

Each pixel in the aSi array consists of a light sensitive photodiode connected to a TFT. The incident x-rays are converted by the scintillator screens to visible light which

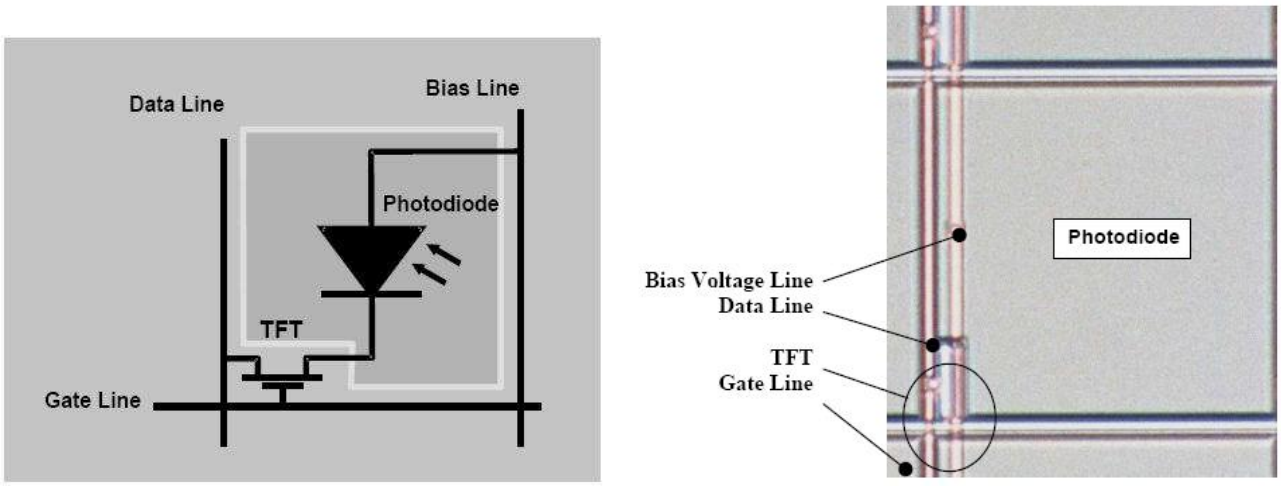

Figure 2.3: aSi pixel generation & microscopic view of an aSi Pixel (Reproduced from Varian document library [34])

generates electron hole pairs in the photodiode. The photodiode acts like a capacitor because the received light is integrated and captured as an electric charge. The charge carriers are stored in the capacity of the photodiode. The TFTs control the readout of the recorded signal, they are switched transparent when the gate lines are enabled, and the charge held in the photodiode is then read out over the data line.

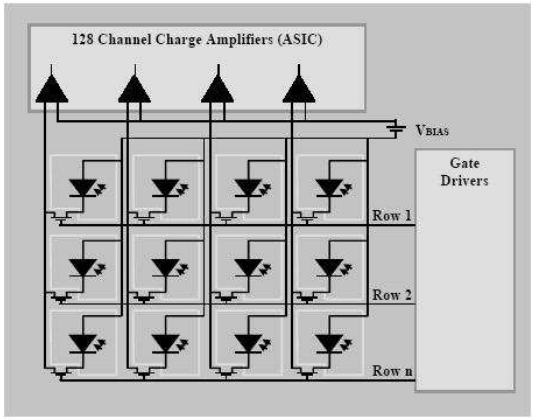

Figure 2.4: Schematic diagram of an aSi 2D imaging array (Reproduced from Varian document library [34])

During irradiation, light that is generated in the x-ray detector discharges the photodiode which has had a bias voltage applied before the irradiation. The TFT is non-conducting during the irradiation. During readout, the TFT is controlled by applying a control voltage to their associated gate lines and this allows charges to flow between the

photodiodes of all columns in parallel to external amplifiers. The current recharges the photodiode to its original bias voltage and a charge amplifier records the charge, which is proportional to the light reaching the photodiode during the irradiation. To acquire an image, the aSi pixels are arranged in a matrix as shown in Figure 2.4. The gate driver electronics enable the first row, i.e. all the TFTs of the entire pixel row are switched transparent. The charges held in all photodiodes (capacitors) of this particular row are conducted to the read-out electronics which have a single charge amplifier per column. As soon as one row is read out, the system switches to the next row and so on until the whole image is generated. All signals of the columns are amplified in charge amplifiers and converted to digital format by analogue to digital converters (ADC's) [1, 34, 35].

Figure 2.5 explains the data flow for Varian clinacs. The x-rays enter the imager and are converted into electrons. The stored charge is then read out and transferred to a digitization unit. The digitization unit converts the analogue pixel information into digital data which is transmitted via a serial high-speed link to the universal control board (UCB).

The UCB is one of the two PCI cards in the workstation. It receives the pixel data stream, encodes and buffers it, and eventually transfers it to the frame processing board (FPB). The video data stream is buffered and synchronized in the UCB. Machine and status information is attached to the image in real-time and the data stream is converted into a standard parallel digital video format. The FPB is the second of the two PCI cards in the workstation. In the FPB the image is further processed (gain, offset, defective pixel correction, averaging, etc.) and transmitted to the graphics adapter card or, if the image is to be stored, to the host memory. The entire acquisition process as well as the synchronization and interaction with the machine is controlled by the UCB [34].

2.3 PortalVision™

PortalVision™ is an application supporting the acquisition of electronic portal images before, during and after treatment and provides tools for quantitative portal image registration and review. The following table gives the specifications of PortalVision™ .

2.4 Theory of operation

This section discusses the beam pulse synchronization during image acquisition for C-Series clinac.

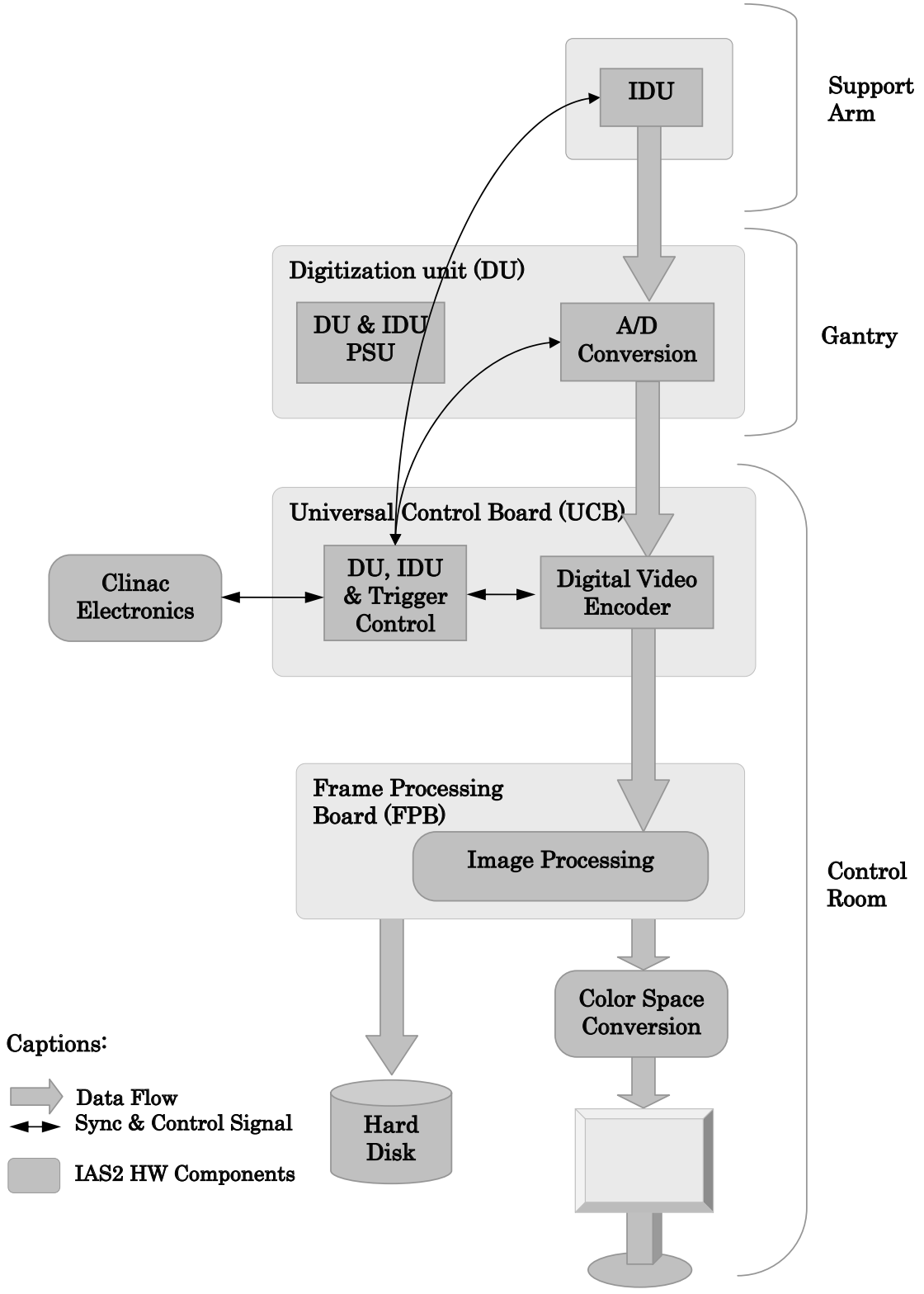

Figure 2.5: Diagram of the IAS data path for clinacs (Reproduced from Varian document library[34])

Table 2.1: PortalVision^{TM} aS500 specifications [36]

Detector	**(A-Si)**
Active Imaging Area	40 x 30cm^2
Resolution	512 x 384 = 196,608 pixels
Absolute Spatial Resolution	0.784mm
Image Acquisition Rate	3 frames/second (frames averaged in hardware)
Image Storage Rate	2 seconds/image (images acquired in cine mode, each stored in PortalVision^{TM} system)
Energy Range	4-25 MV
DR Range	50-600 MU/min

2.4.1 Verification of clinac settings

The actual clinac settings have to be determined before an image can be acquired. This is done with the IAS 2 trigger board PCB.

2.4.2 Detecting the rep rate for C-series clinacs

The dose rate of the clinac is varied by applying different pulse patterns to its output beam. It provides two signals to verify repetition rate (Rep rate)

- Gun pulse repetition frequency (GPRF) masks the Rep rate
- Synchronisation (SYNC) is a frequency that depends on clinac energy.

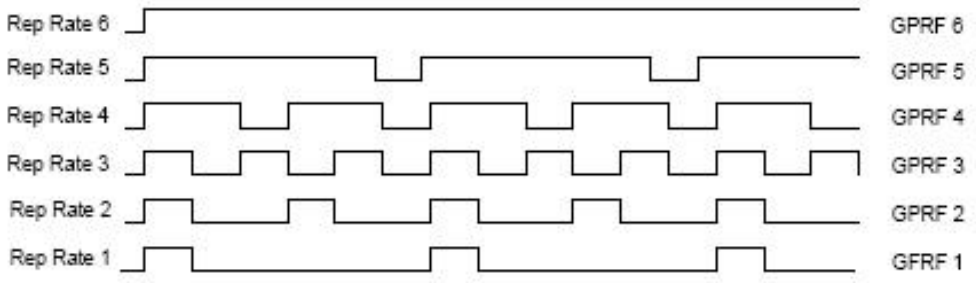

Figure 2.6: Clinac GPRF Signals (Reproduced from Varian document library [34])

The two signals are logically AND-linked. The pulses of the resulting signal are counted and stored as the verified Rep rate. Thus the repetition rate of the clinac is verified.

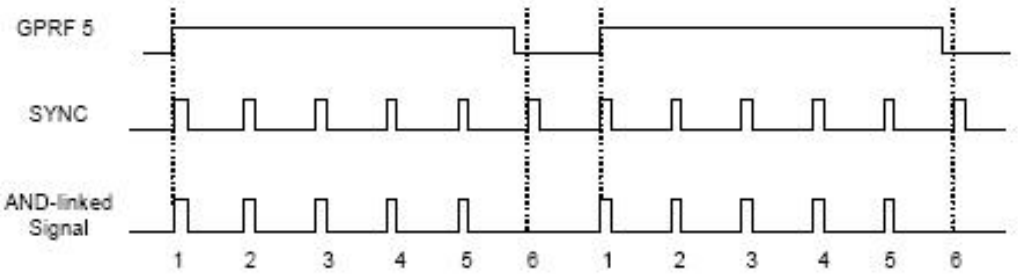

Figure 2.7: Verification example for repetition rate 5 (Reproduced from Varian document library [34])

2.4.3 Detecting the clinacs energy.

Determination of clinac energy is important to verify and synchronise pulses with portal imager. The clinacs dose rate servo (DRS) provides two signals to verify its energy, namely low photon energy (LOX) (6MV) and high photon energy (HIX)(18 MV)

2.5 Electronic readout of aSi detectors

Three electronic readout schemes are used for three acquisition modes of an aSi EPID. All three modes work towards a common goal of acquiring images with optimal Signal to Noise Ratio (SNR). The acquisition modes are [35]

- Single Mode
- Continuous Mode
- Cone Beam Mode

Single mode

During single mode acquisition, the configured number of frames are readout prior to the start of irradiation. This cycle is called the refresh cycle, it clears the accumulated dark current and residual data. No readout occurs during the delivery of the radiation and the signal is integrated over the entire exposure period. The trailing edge of the Rad-on signal, generates one trigger pulse initiating one frame readout and also the accumulated data of the pixels during exposure interval. This readout scheme reduces the effects of readout noise and eliminates the pulsing effects of the linac on the final image. Since the signal is integrated during the exposure time and the readout is performed after the exposure, this improves the signal to noise ratio (SNR). The single mode acquisition is

routinely used clinically and allows the acquisition of clinical images with a small amount of exposure ($\leq$ 2 MU) [35].

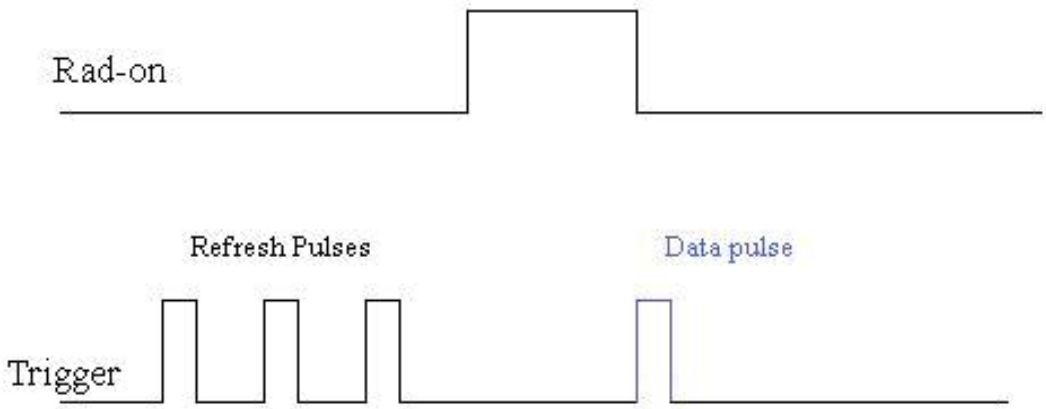

Figure 2.8: Single mode with forced sensor discharge (Reproduced from J. Pouliot web Tutorial on EPID [35])

Continuous mode - high dose imaging

Continuous mode is primarily used for monitoring the patient during intensity modulation radio therapy (IMRT) treatment. This acquisition mode includes movie images and the verification image (average of movie images). Implemention of this mode can be done with either the use of free running mode or external trigger mode. The linac pulsing artefact cannot be removed by using free running mode due to the absence of synchronization between frame readout and linear accelerator. The external trigger continuous mode synchronizes the frame readout with linac pulses thus eliminating the pulsing artefacts. This not only improves the image quality of movie images but also increases the accuracy of dosimetric verifications for applications such as IMRT. The external continuous mode can be further divided into two synchronization modes; line synchronization and frame synchronization. In line synchronization, each lines can be triggered and readout individually. In frame synchronization mode, the start of frame is synchronized with linac pulses. The sensors are forced to be discharged prior to the start of radiation (Rad-on) to eliminate the dark current accumulation (Figure 2.9).

The linac beam pulses are synchronised to the external trigger pulses which in turn are synchronised with the start of each frame scan. All the linac pulses that occur during a frame scan are ignored by the flat panel imager. Pulsing artefacts are corrected by linking the gain image to the acquired image in frame synchronization mode. An offset correction

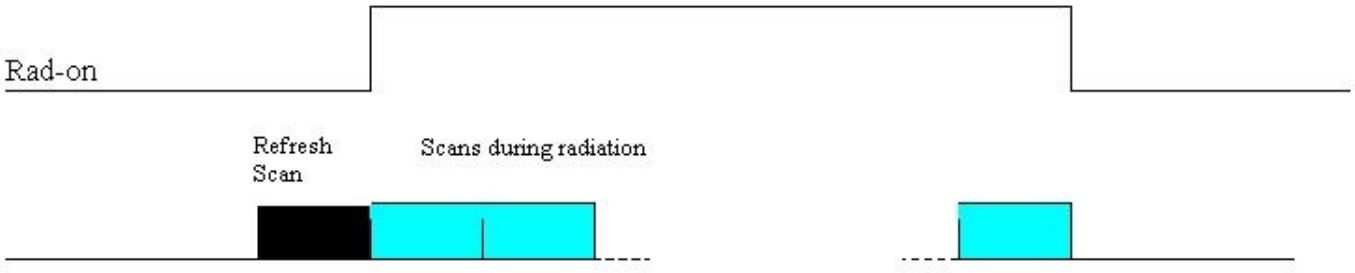

Figure 2.9: External continuous mode with frame synchronization (Reproduced from J. Pouliot web tutorial on EPID [35])

image is used to correct the dark current of each pixel. During the gain correction, the median value of the pixel data of the whole sensor is evaluated and each individual pixel value is mapped to the median value. The final verification image is the average of the frame scan during radiation exposure. During IMRT, a refresh scan occurs before the start of each treatment segment [35].

Cone beam mode

Cone beam acquisition mode is used to perform volume (multislice) megavoltage CT (MVCT) in the cone beam geometry to visualize 3D (three dimensional) anatomy during patient positioning. In this mode image acquisition is synchronized with the linac enabling the imager to remove the pulsing artefacts from the image while also improving the SNR [35].

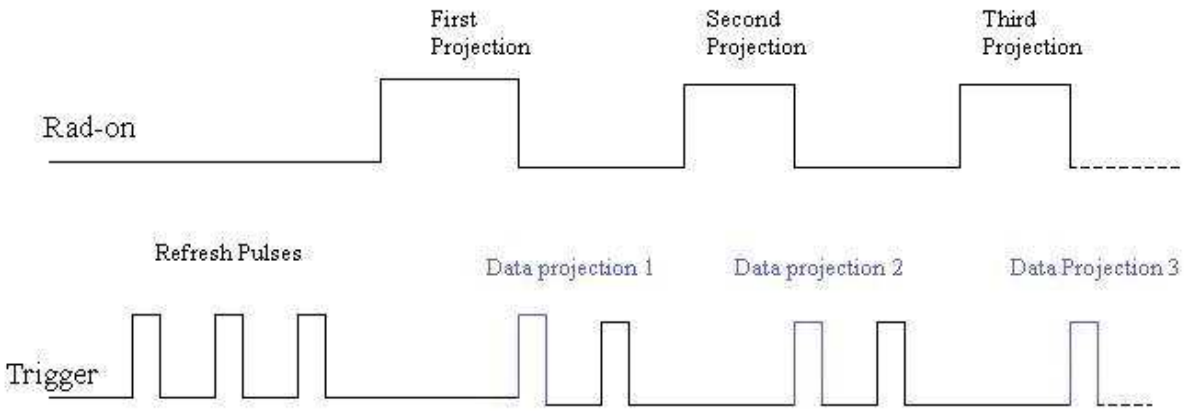

Figure 2.10: Cone beam mode (Reproduced from J. Pouliot web Tutorial on EPID [35])

2.6 Dose rate servo control

Dose rate servos are an integral part of the beam dosimetry control system discussed in Appendix C. The dose rate of the linac is stabilised by these dose rate servo's. There are three different dose rate servos (DRS) achieving the same goal in different ways:

- Pulse Drop Servo (PDS).
- Pulse Length Servo (PLS)
- Pulse Frequency Servo (PFS).

Dose rate servos tend to cause slow dose fluctuations appearing in images as horizontal bars with different grey scale levels. The width of the bars may vary from image to image and from dose rate to dose rate.

Pulse drop servo

The original DRS built in the clinac is pulse drop servo (PDS). This servo cuts off beam pulses irregularly to stabilise the dose rate, making it unsuitable for acquisition of portal images. However, PDS is required for any sort of dynamic beam delivery such as arc therapy or dynamic wedge. Since portal images can only be taken for x-ray beams, the PLS2 is switched off for electron treatments, so the PDS is still used for electrons [34, 37].

Pulse length servo

The Pulse length servo (PLS) is used with PortalVision^{TM} on high energy clinac and replaces the PDS. The PLS functions by varying the length of each beam pulse ('Gun I') in order to maintain a stabilized dose rate.

The averaged dose rate is maintained by changing the dose per BEAM pulse. The length of the GUN pulse is controlled, instead of dropping pulses completely as in PDS. The DRS is switched into a stable mode during image acquisition . The PLS freezes its output voltage so that the pulse length does not vary. However, it is not frozen during flood field calibration and IMRT image verification.The PLS2 has control over the PDS, it switches itself off and the PDS on if required, and also monitors the energy code [34, 37].

Pulse frequency servo

The pulse frequency servo is used with PortalVision^{TM} on low energy clinacs. The PFS keeps the repetition rate constant during image acquisition. Both PLS and PFS are used

to synchronize the PortalVision^{TM} with the clinac.

The PFS2 delivers trigger pulses without pulse dropping and without pulse pattern as long as no image is being acquired. The DR is stabilized by suitably varying the PRF of these trigger pulses. During image acquisition, the new PFS2 delivers trigger pulses with a stable PRF, without pulse dropping but with a pulse pattern. The DR is not stabilized during the image acquisition [34, 37].

2.6.1 DRS control during image sequence

The *Start delay* is the time between switching the beam on and starting an image acquisition. This is applied only to the first image or frame in a sequence. There is no delay, if the machine is already irradiating when acquisition is enabled.

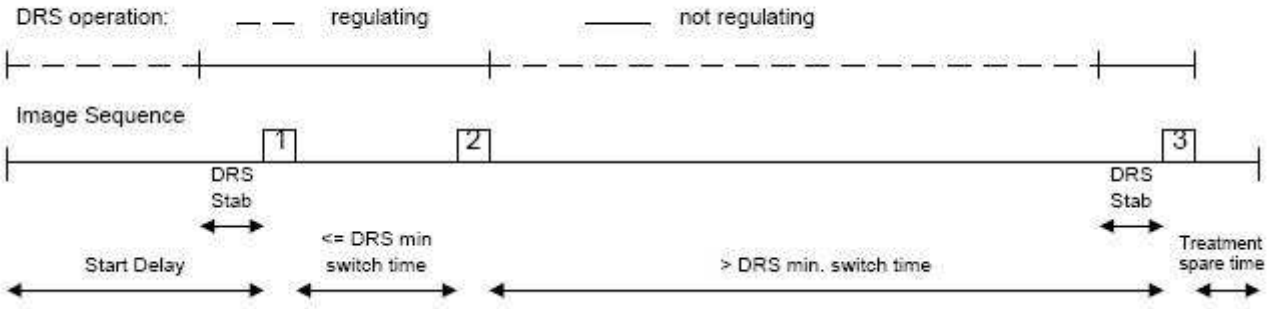

Figure 2.11: DRS control (Reproduced from Varian document library [34])

DSR stabilization time to stabilize output after switching from regulating into non-regulating mode. If *Start Delay* is less than or equal to the *DSR stabilization Time*, the DRS is switched into non-regulating mode while waiting for beam state.

If the time between two images is less than or equal to *DRS minimal switch time*, the DRS is kept in non-regulating mode.

The *Treatment spare time* is applied between the last image and the end of the planned treatment to cover dose variations of the clinac [34].

2.7 Effect of dose rate variations

The clinac can be tuned to minimise the effect of dose rate variations. The dose rate servos stabilise the dose rate by counting the pulses and hence are too slow to correct these small but quick dose variations from pulse to pulse. PortalVision^{TM} imager has a contrast resolution of 0.25%, hence is sensitive enough to show these variations in dose rate. These show up as light bands of brighter or darker hue across the acquired image. The bands are only visible in images presented with an extremely high contrast; but this is exactly where the strength of EPI is. The width of the bands depends on how fast the dose rate 'toggles'.

Another type of dose rate variations consist of short 'hiccups' i.e. a singular pulse or a short train of pulses that are smaller than all others. This causes one or two bright horizontal lines to appear across the image. It has been noted in the literature with clinac 600C that such hiccups can result from an arc and thus be eliminated by purging the SF_6 gas [34].

2.8 Portal dosimetry

'Dosimetry' is a process of measuring dose. Portal dosimetry is the capability of a system to carry out that process. Portal dosimetry in itself is not a novel technique, it has been carried out for decades using films, diodes, MOSFETS, TLD's etc. However, these devices have been very inconvenient and time consuming, affecting patient throughput and the efficiency of a department. The principle limitation being the inability to acquire entire dose distributions thus enabling only point dose measurements. With techniques becoming more conformal and plans complicated, dosimetric verification was a cumbersome process. Hence, there was a requirement for development of a simple and efficient system to enable dose acquisition in a fast and easy manner.

The capabilities of an EPID to acquire large two dimensional arrays of digitized x-ray data, proven in the imaging field, were very apt and attractive for use in dosimetric verification. Varian explored this potential and developed portal dosimetry using amorphous silicon EPID also known as EPID dosimetry. Hence, portal dosimetry is the use of an EPID to produce 2-dimensional dose maps in the plane of the imager in addition to the grayscale images. The averaged grayscale image is converted into a portal dose image in the dosimetric workspace by multiplying it by the total acquisition time. A correction for beam profile is applied followed by absolute dose calibration. The entire process has been detailed below.

2.9 Varian's portal dosimetry system

To enable acquisition of dosimetric images, various aspects of the system are required. Wellington Blood and Cancer Centre (WBCC) has Varian's Portal Dosimetry System. This system can be divided in three main categories namely

Portal dose acquisition: For acquisition of dosimetric images some hardware components integrated with the software are needed. WBCC has aS500 amorphous silicon detector plate which has been discussed in detail. This image detector is mounted on a retractable (R-arm) or an exact arm (E-arm) which is integrated with the clinac.

Portal dosimetry software in addition to the image acquisition system (IAS) is also required for the EPID to acquire dose maps. A special licence is needed to activate the 'Dosimetry Workspace'.

Portal dose prediction: Algorithms on treatment planning system (Eclipse) are required to enable prediction of dose maps. These predicted dose images (PDI) are compared to the measured dose maps for dosimetric verification of treatment plans. This algorithm becomes mandatory if one would like to perform pre-treatment verification of treatment plans. However, for the sole purpose of acquiring dose maps, the prediction algorithm is not necessary. WBCC has not yet commissioned the algorithm, as this was not required for the purposes of this research.

Comparison of predicted to actual dose maps: An evaluation module is required for comparison between PDI and measured dose maps. The *Review* workspace in Vision caters for this module. All tools for analysis and comparison of dosimetric images like 'Gamma evaluation', ' Dose difference' etc are available in this workspace. However, this is not a mandatory requirement as such analysis can be carried out using other analytical softwares.

Fig 2.12 clarifies the entire workflow of the process.

2.10 Commissioning of portal dosimetry

Commissioning of the portal dosimetry system starts with configuring the Varis \ Vision system. This is accomplished partially by the Varian representative alongside input from the responsible medical physicist.

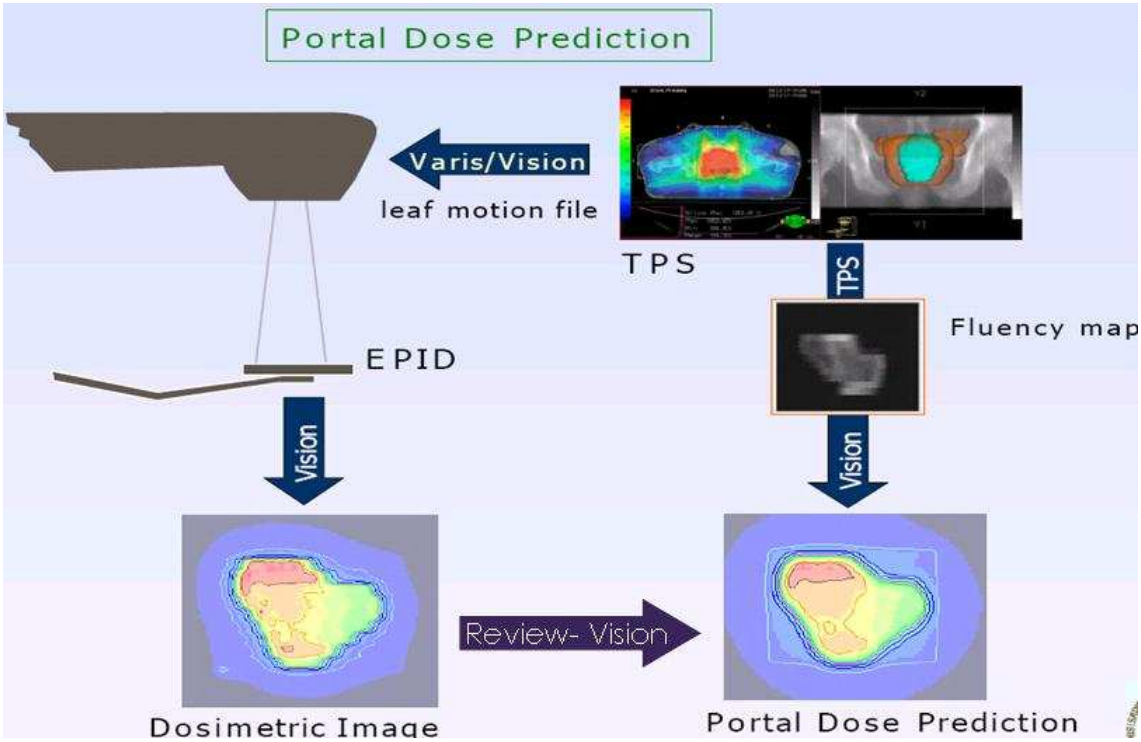

Figure 2.12: Portal dosimetry process (Reproduced from Ann Van Esch et al. Univ of Leuven [32])

2.10.1 Varis \ Vision system

'Administration Task' of the system needs to be configured as a first step of commissioning by defining the portal imager parameters for the selected treatment unit in 'Radiation and Imaging Device Workspace'. After these parameters are set, the 'Template and Processing Workspace' also needs to be configured. A *Sequence Template* for integrated image is defined along with isodose level template for portal dose evaluation.

Integrated images facilitate the scheduling of portal doses. Image frames are continuously acquired during the treatment beam-on time. When the treatment beam is completed, all frames are integrated into a single density image so as to calculate the dose. A dose image in addition to the density image is recorded.

2.10.2 Portal imager

The integrated image acquisition mode and the sequence template for 'AM Maintenance' also needs to be configured.

The aSi detector is not water equivalent. Hence dosimetry calibration of the detector

is required to force it to read doses equivalent to an ion chamber. Dosimetric calibration has to be performed for every treatment acquisition mode to be used for portal dose measurements. The dosimetric calibration also corrects for the variation in x-ray intensity across the x-ray beam. The calibration process also involves correction of dark current and pixel to pixel sensitivity variations as part of standard imaging calibrations, performed prior to the dosimetric calibration. This section discusses the calibration procedure in detail as recommended by Varian.

Imager calibration

The system requires a set of calibration images for each combination of acquisition mode, energy and dose rate parameters of the treatment machine used. An imager calibration set comprises of two images, a dark-field image and a flood-field image. Each set is stored in the IAS database. Both images consist of upto 10 individual images taken in succession. The dark-field image, is taken without radiation passing through the cassette. PortalVision^{TM} uses the averaged result of all images for correction.

Dark field image: In the dark-field image (DF), individual pixel-by-pixel values are measured by periodically acquiring an image without radiation. The DF correction image is synchronized. An average of several images measured in quick succession is taken for minimum noise. Its contents reflect array imperfections and electrometer offsets. The DF looks different for different sets of acquisition timing parameters but is independent of the linac. Figure 2.13 displays a typical dark field image exhibiting bright and dark vertical stripes, quite narrowly spaced [34].

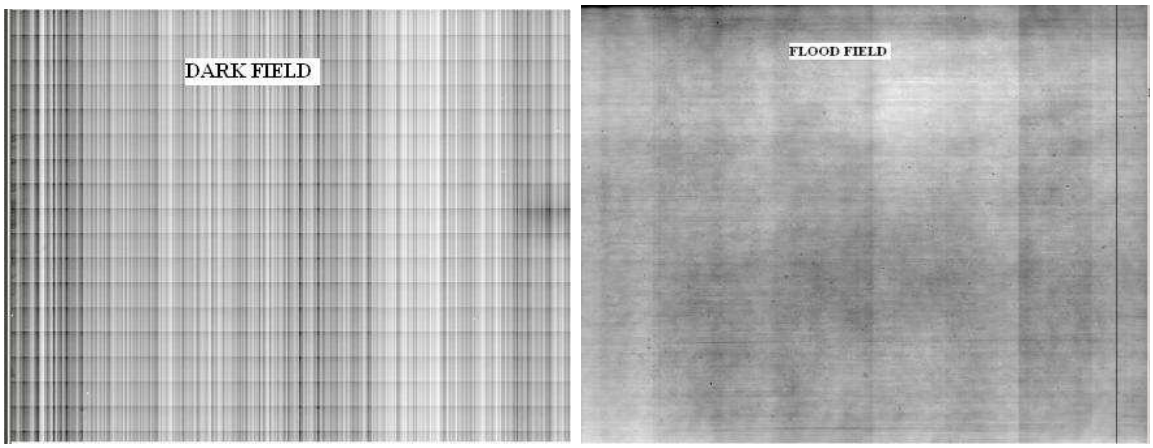

Figure 2.13: Dark field and flood field

Flood field image : The flood-field (FF) image, like dark field, is also measured several times in quick succession and averaged for minimum noise. Its contents represent the field homogeneity, individual cell sensitivities and electrometer gains. The sensitivity of each pixel is determined periodically by acquiring an image with radiation for a wide-open field without an object. The FF image looks different for different sets of acquisition timing parameters, it is also dependent on the linacs' properties. In particular, dose rate variations occurring during the acquisition of the FF image will lead to a wrong FF correction.

The flood field (figure 2.13) image in general exhibit vertical bands of varying brightness, not so narrowly spaced as in the dark-field. Due to beam artifacts, a horizontal line may appear on the first row scanned between beam pulses [34].

These images are used for corrections following the standard correction scheme as explained below

Offset correction The stored dark field image is subtracted from the acquired raw image. The total magnitude of this correction is about 5%

Gain correction The offset corrected image is divided by the stored normalised flood-field image. The total magnitude of this correction can be upto 40%. FF_{mean} is the mean value of the flood field image.

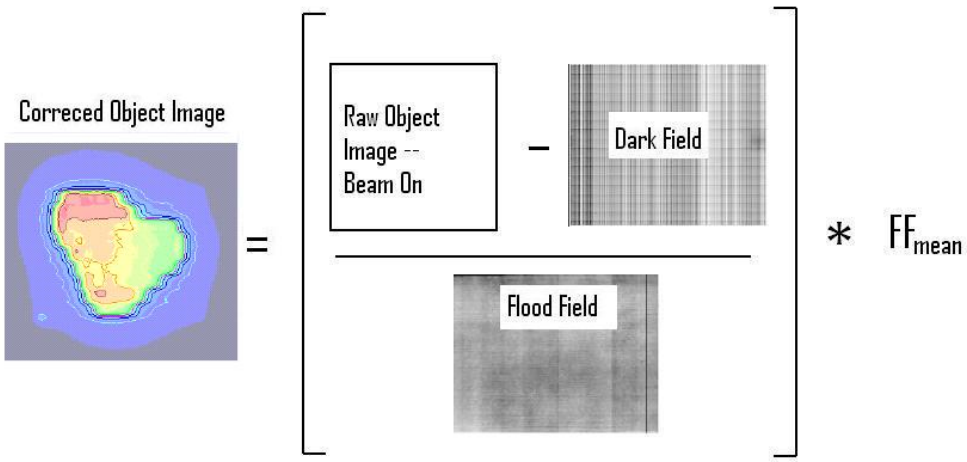

Figure 2.14: Standard correction scheme (Reproduced from Varian PortalVision^{TM} aS500 system manual [37])

Dosimetry calibration

Dosimetry calibration involves defining the SSD value at which the imager is positioned for calibration, import of a diagonal profile for beam profile correction explained below and finally the absolute calibration of calibrated units (CU).

Beam profile correction: This step corrects for some simplifications used by the standard imaging calibration. During the flood field calibration the cassettes are irradiated using an open field from the treatment beam. The flood field calibration then corrects the signals generated by the cassette assuming that the treatment beam has uniform intensity. While ignoring the beam horns is fine for imaging applications it is not sufficiently accurate for dosimetry purposes. This step in the dosimetry calibration allows the user to provide a single diagonal profile of the largest field size opening of the accelerator. The software automatically generates a radially symmetric correction based on the entered profile [34].

Dose normalization: In this step the portal imager is calibrated so that the signals generated by the radiation beam are related to dose as measured by more conventional dosimeters, such as farmer ionization chambers. If this calibration has been performed, the acquired portal doses will be displayed in calibrated units (CU), otherwise in percent.

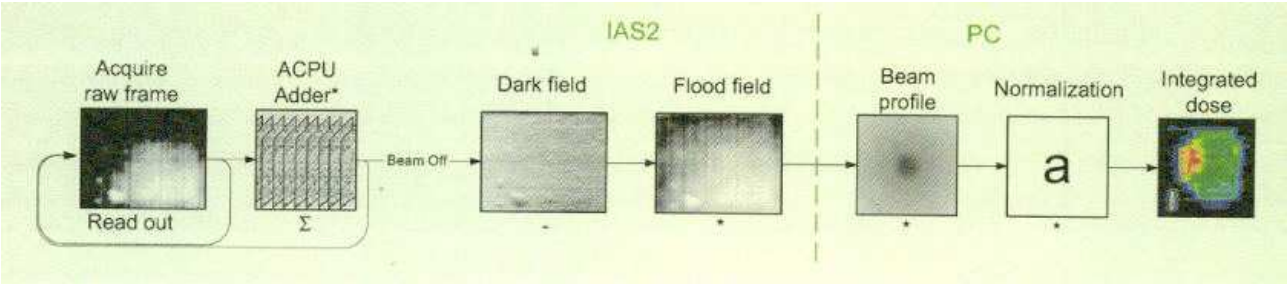

Figure 2.15: Correction scheme for aSi detector aS500(Reproduced from Varian PortalVision^{TM} and dosimetry 6.5 document library [38])

2.10.3 Dosimetric portal image calculation algorithm (DPIC)

The Dosimetric Portal Image Calculation (DPIC) algorithm calculates a predicted dosimetric image. The prediction is performed at the detector plate of EPID without accounting for the couch or patient in the beam. Hence, currently portal dosimetry using Varian's software is essentially verifying the plan and not the dose delivered to the patient.

The algorithm is part of Eclipse treatment planning system, commissioning it involves defining the new algorithm which is the responsibility of the Varian representative. However the algorithm configuration remains a medical physicist task. This process requires beam data, an intensity profile, definition of output factors, dosimetric images acquired for calibration fluence and an actual fluence. The procedure for the commissioning can be found in Varian documentation. Since the algorithm is not yet commissioned at WBCC, it will not be discussed further in this thesis.

2.11 Implementation at WBCC

At WBCC, intensity modulated radiation therapy (IMRT) has not been implemented yet. But almost 95% of patients here undergo EDW treatments. So as a first step towards transit dosimetry, it was imperative to investigate how varying dose rate impacts the ability to acquire a dose image. But the system was configured to disable image acquisition during the arc therapy, electron treatments, and even during the dynamic phase of an EDW treatment.

Most linacs operate on pulse length servo to stabilize dose rate, which also facilitates image acquisition as discussed above. But the dynamic wedge treatments are carried out under the control of pulse drop servo, which is required to vary the dose rate. However, varying dose rate deteriorates image quality. Hence initially, the PortalVision^{TM} system was configured to disable image acquisition under PDS control i.e. during arc therapy, electron treatments, and during the dynamic phase of an EDW treatment to maintain the image quality. Although this is a perfectly justified reason, it did not permit imaging or dosimetry in any treatments other than static.

To enable image acquisition during the dynamic phase of an EDW treatment modifications to the clinac settings were required. These modifications have been described in Appendix B.

The portal imager was commissioned as per the Varian procedure, to obtain some EDW images. Following are some of the first EDW images acquired.

Although the image acquisition for EDW was enabled, these were not dose images, which suggested an incorrect setup. The sequence template, calibrations and all the standard Varian parameters and procedures were verified without much success. On

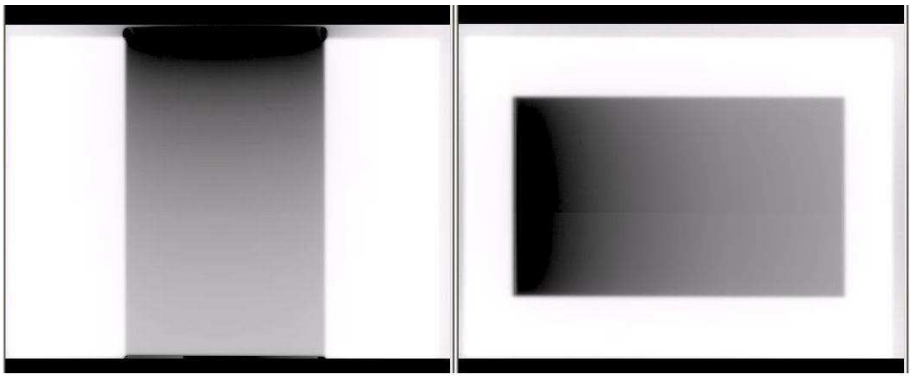

Figure 2.16: EDW images using portal dosimetry

configuring the integrated image template and acquiring a dose image in IMRT mode, the system sets the number of frames to be acquired as '9996'. Initially, realizing that the suggested '9996' number of frames was a very large number it was changed to a more realistic number of a few hundreds. However, it was later understood that the number '9996', besides being a big number to accommodate every treatment length, is also a code which tells the system to acquire a dosimetric image as opposed to a grayscale image. Figure 2.17 are the first EDW dose images obtained and the profile across it.

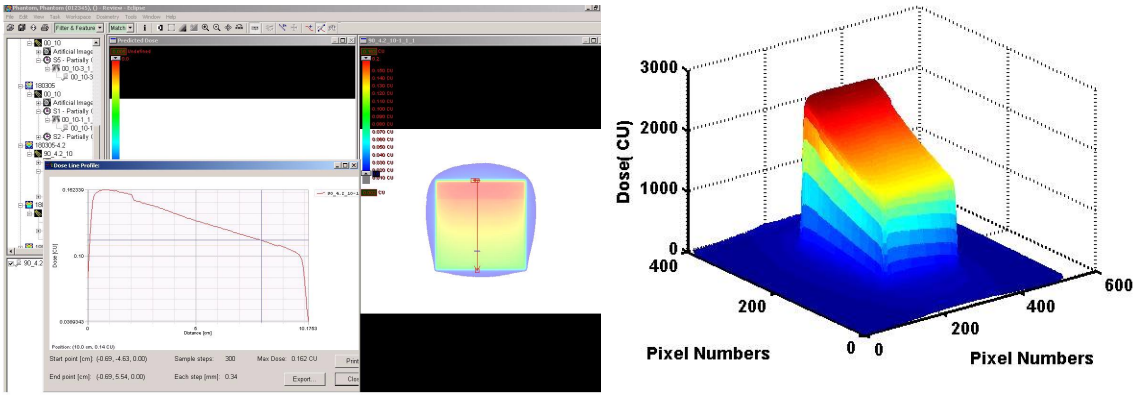

Figure 2.17: First EDW dose image

Step issue

There were some further issues that came to light with the success in acquisition of dose images. The dose images presented with a 'step' of approximately 4-8% discrepancy. The following is a test image, showing the step very distinctly, going back a step to flood fields, the step was present there too.

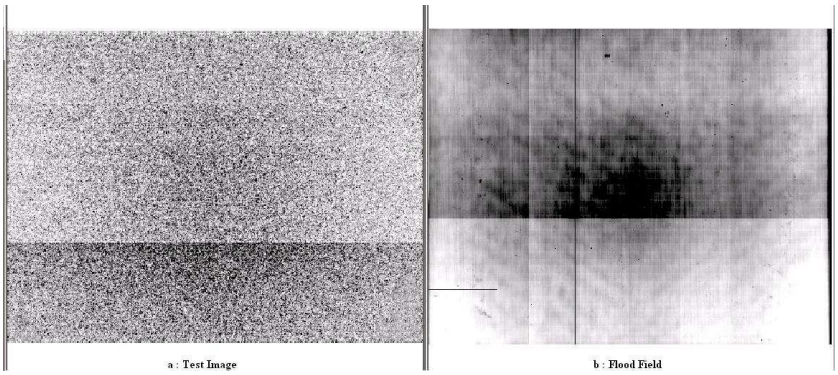

Figure 2.18: Step in test image and flood field

Increasing the number of frames used to acquire a flood field got rid of the step in the flood field, but was still present on the test image. However, interestingly, they did not appear on the clinical images. This was due to the wide contrast levels on clinical images as opposed to very small range on the test image.

Artefact's due to varying dose rate during calibration was ruled out experimentally, by acquiring the flood field after the dose rate was stabilized. There was one other explanation for the occurrence of the step, an incomplete frame readout, which meant that the beam was switched off before the last frame was read completely. Hence the imager read N plus a fraction of frames. However, one partial frame should not have such a pronounced effect for a large number of frames acquired, this invalidated the theory of partial frame acquisition at the time.

Step resolution

Although, the understanding of the step was a little skewed, the partial frame theory wasn't completely invalidated. On acquiring an image the IAS (image acquisition system) takes a few seconds of preparation, during that time if the beam is activated, the system misses out on the initial few frames as opposed to the last frame that we contemplated. Hence, after the upgrade of the software to version 7.3.10 it was understood that if the beam is activated after a few seconds of starting the image acquisition, rather wait for the IAS to send a message 'Waiting for beam pulses' to activate the beam the system is enabled to accumulate all the dose from the first beam pulse and hence a complete frame readout takes place. These few seconds wait thus eliminates the step from the dosimetric images. Having resolved the step issue enabled the acquisition of the dosimetric images

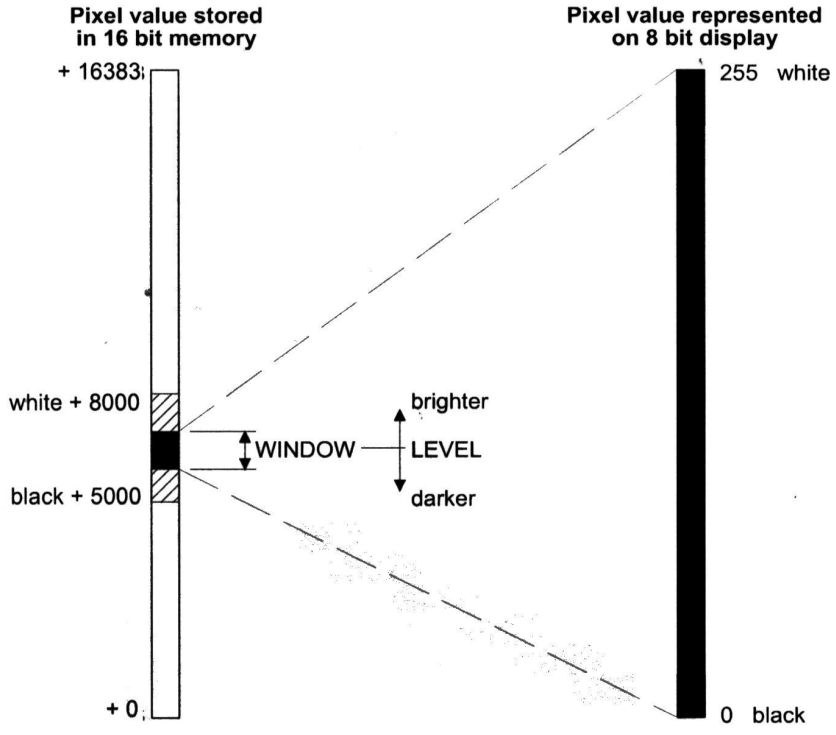

Figure 2.19: Image/level windowing (Reproduced from Varian document library [34])

accurately for exploring various dosimetric characteristics.

2.12 Dosimetric characteristics

Dosimetric characteristics of the aSi detectors have been studied extensively by many researchers some of which have been summarised here.

2.12.1 Energy response

Previous studies for aSi systems have established that the EPID exhibits an increase in energy response for lower energy (< 1 MeV) photons. This hypersensitivity is attributed to the high atomic number phosphors such as Gd_2O_2S:Tb due to the dominance of photoelectric effect in low energies [39, 40, 41].

2.12.2 Response to dose rate fluctuations

The EPID is calibrated for every energy and fixed dose rate settings of the linac to be clinically used. Since the readout of the EPID is synchronised to the linac beam pulses the dark field and the flood field are different for each dose rate due to the difference in

pulse timing and hence in image acquisition timing. For dynamic treatments like EDW or some cases of IMRT the dose rate is varied during the treatment. As the EPID signal is calibrated for fixed dose rates the fluctuations in dose rate can potentially influence the response of EPID. To understand the behavior of EPID response in situations of varying dose rate Greer et al. [42] studied the response of dose rate fluctuations by examining the EPID signal under a 'step-wedged' IMRT pattern with and without beam hold-offs. They noted fluctuations of less than 1% between the signal recorded for with and without beam hold-offs. Hence varying dose rate did not seem to hinder the accuracy of EPID signal inspite of fixed dose rate calibrations.

These results were very promising for EDW dosimetry using EPID and seems feasible theoretically. However, no detailed study of EDW using EPID was found. One reason could be that the system was not enabled to acquire dose images during a dynamic phase of EDW until recently. But at WBCC, 95% of patients undergo EDW treatments, hence enabling its acquisition and studying the behaviour of EPID under EDW conditions was required for optimal use of portal dosimetry.

2.12.3 Detector saturation

As discussed earlier the detector consists of an array of photodiodes. The capacitance of each photodiodes is adequately large to ensure charge accumulation during subsequent readouts. However, since the analogue signal from the pre-amplifiers are converted into signed 13 bit values via a 14 bit A/D component saturation occurs for pixel counts exceeding an absolute value of 8192 (including dark field pixel count) [43]. Detector saturation was found to be very pronounced for dose rates higher than 300 MU/min for SDD = 105cm. It was concluded to be negligible at SDD = 145cm for all dose rate settings (Figure 2.20). Hence a suggestion for limiting the clinical dose rate to 300 MU/min was made to maintain good accuracy of dosimetric data for all SDD's.

This could be beneficial and achievable for IMRT enabled departments, but would be highly restrictive at WBCC since the typical dose rate used for treatment is 600MU/min. Hence an alternate approach to allow accurate dosimetry is required.

The detector saturates under two scenarios. Firstly, during the calibration process of the EPID where the flood field acquired can be saturated and secondly during the dosimetric measurements. Since the typical measurements are performed at larger SDD's

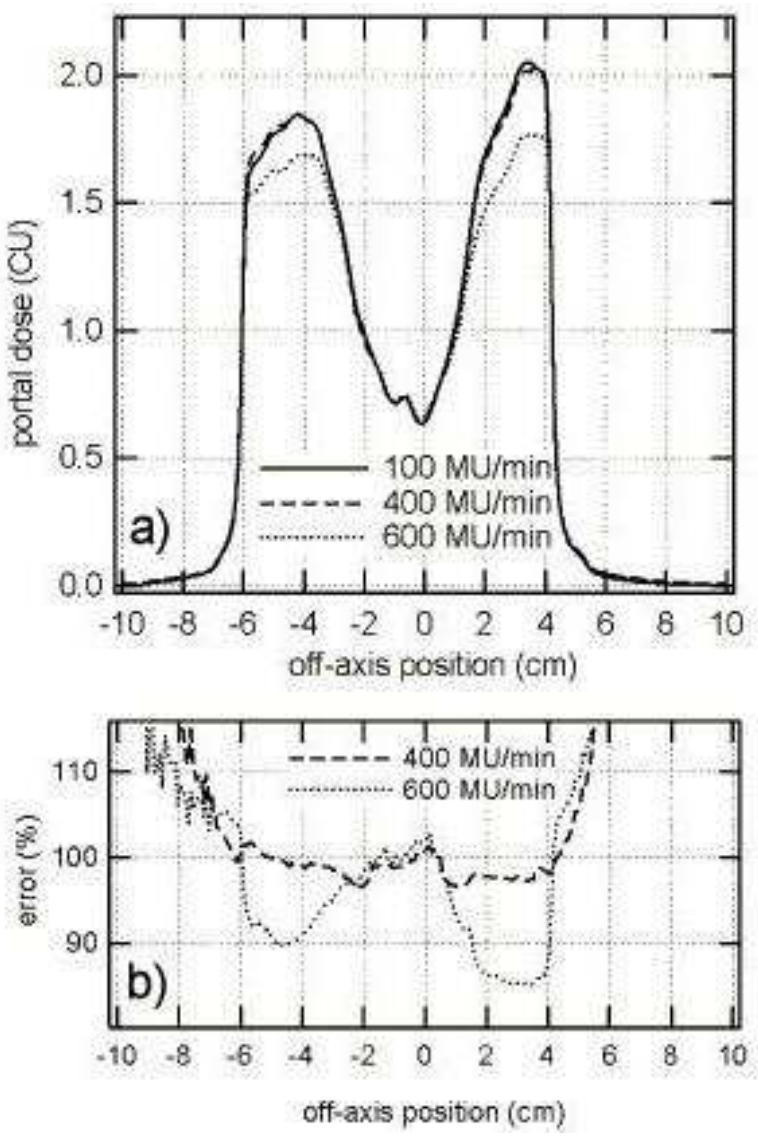

Figure 2.20: Line profiles extracted from the absolute portal dose detection of a dynamic field delivery with 6 MV at SDD = 105cm. No saturation effects are present in the image acquired with a dose rate of 100 MU/min, minor discrepancies are present at 400 MU/min, whereas unacceptable distortions (i.e. by large exceeding the gamma evaluation criteria of 3%, 3mm) are noticeable at 600 MU/min. (b) Relative distortions, i.e. the ratio of the line profiles for 400 and 600 MU/min to the line profile at 100 MU/min. (Graph taken from Ann Van Esch et al. Radiotherapy and Oncology (2004) [43])

or with a patient or phantom in the beam, this is less likely to cause detector saturation. Therefore, it is necessary to avoid saturation of the flood field during the calibration process. Varian recommended calibration distance is SDD = 105cm which causes detector to saturate at dose dose rates higher than 300MU/min. Therefore a study to determine the effect of calibrating the detector at the measurement distance SDD = 150cm was performed as an attempt to improve dosimetric accuracy.

2.12.4 Linearity

Several investigators have studied the linearity of detector response to incident radiation with two experiments [42, 43, 44, 45].

Frame averaging

Linearity of dose response with respect to frame averaging has been reported in literature. This is studied by examining the linearity with respect to number of acquired frames, since EPID image is the average of acquired frames. This translates as two images acquired with different dose or monitor unit settings should result in the same pixel values if the dose rate and hence dose per frame is kept constant. A simple way of determining the relation is to acquire images for different monitor unit settings for the same dose rate. The detected total dose was found to be proportional to the amount of MUs, over the entire measured range. The detector responded with better than ± 2% of ideal linearity.

Dose rate

The linearity due to variations in the dose rate was investigated by monitoring the signal on the beam axis for a static field, same monitor units but varying the detector distance from the source to invoke inverse square law (ISL). The detector response agreed within 2% with the ionisation chamber measurements and 1% with the ISL behaviour (Fig 2.21).

Since linearity of detector is well established in literature and proven to be linear with dose rate and MU, no detailed study was required. Hence only a verification was performed in this thesis to establish that the EPID at WBCC performs as expected.

2.12.5 Asymmetric field profiles

The ability to acquire accurate dosimetry for asymmetric fields is another aspect which needs to be addressed for portal dosimetry. Theoretically, EPID should be able to accurately acquire symmetric and asymmetric fields as the beam information has been provided in the form of diagonal profile. However, the accuracy of portal dosimetry is not well defined under asymmetric field conditions which could require displacing the EPID from the central axis positions. Therefore, a study to understand the behaviour of EPID under asymmetric field conditions has been performed in this thesis.

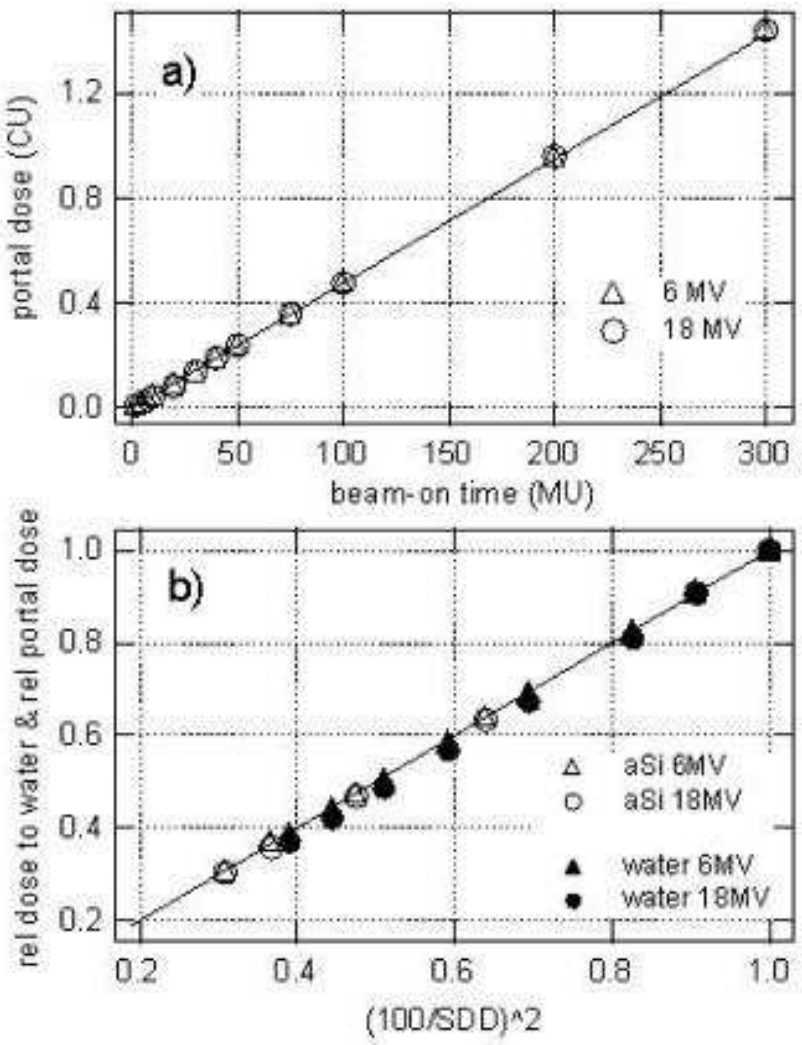

Figure 2.21: Portal dose dependence on the beam axis as a function of beam on time, measured at SDD = 145cm for a field size of 10 x 10cm^2 (6 and 18 MV). (b) Inverse square law behaviour, measured for a field size of 10 x 10cm^2 with the aSi detector and with an ionisation chamber in water at 8mm depth, for varying SDD. The solid lines in both graphs represent ideal linearity. (Graph taken from Ann Van Esch et al. Radiotherapy and Oncology (2004) [43])

2.12.6 Ghosting

The modification of dose response of the detector due to previous irradiations is termed as 'ghosting'. This effect is exhibited by EPID's which are based on semiconductor materials. Image lag is defined as residual signal, the charge generated in one image which could be read out in subsequent image frames. For amorphous silicon, the image lag is primarily caused due to the trapping and release of charge in sensor elements. While the charge trapping is an issue another type of ghosting is associated with the change in gain(or sensitivity). During exposure the electric field strength within the photodiode bulk and

interface layers is altered by the charge stored in deep trapping states resulting in a change in the sensitivity of the aSi layer. If EPID's demonstrate a variation in its dose response due to any of these effects as a result of foregoing irradiations, it could have a considerable influence on dosimetric measurements. This could give adverse results especially for IMRT treatments, where a number of fields are delivered in a short span of time.

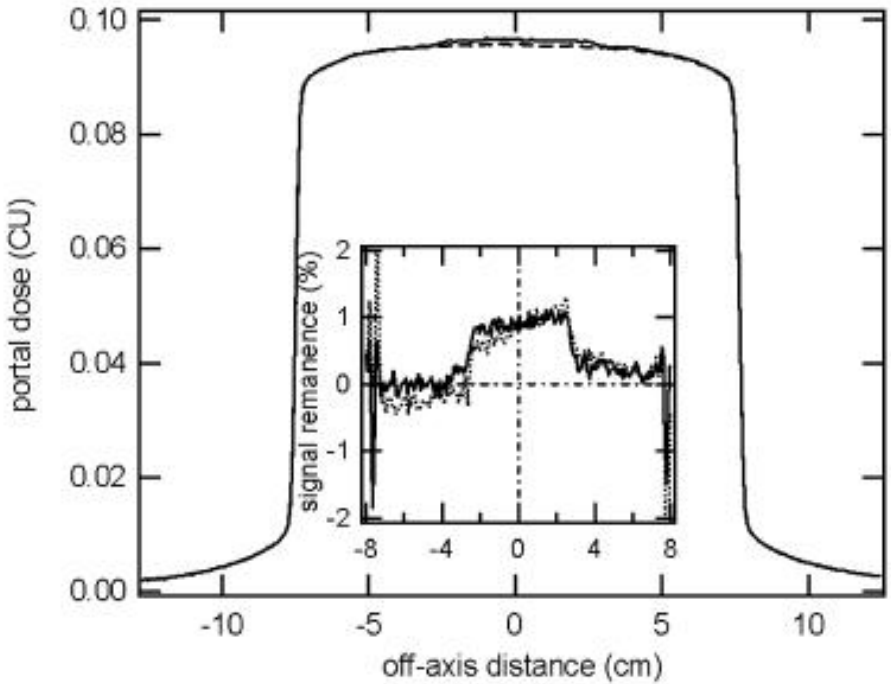

Figure 2.22: Line profiles of a 15 x 15cm^2 static field (6 MV, 10 MU) with (solid line) and without (dashed line) preceding irradiation of a 5 x 5cm^2 field (500 MU). The ratio of both line profiles is displayed in the insert for 6 MV (solid line) and 18 MV (dotted line) (Graph taken from Ann Van Esch et al. Radiotherapy and Oncology (2004) [43])

Ghosting characteristics to assess the existence of memory effect of aSi detector of EPID has been studied. Elekta's amorphous silicon EPID's [46] have shown that an increase in the ratio of dose of the first field to the second field could result in more pronounced ghosting effects. Shorter time intervals between two fields was shown to raise the magnitude of ghosting. McDermott et al. suggests that the ghosting effect is not merely an image lag and an alternative correction factor based on irradiation time is required, as the decay rate of the EPID signal depends primarily on the beam on time (hence the number of acquired frames) not on dose. They have modelled a ghosting correction for the change in response as a function of beam time to obtain a constant dose-response to within $\pm 1\%$ up to 1000 MUs [39]. These are shown to be corrected by dynamically correcting for dark field [22].

Some experiments were carried out using aS500 by another group which irradiated a 20 x 20cm^2 field shortly after a 5 x 5cm^2 which reported 'faint ghosting' of less than 0.2% in the time interval between two image acquisitions [42]. However, a signal remnant of below 1% for a 6MV beam has been reported [43] as shown in Figure 2.22. These effects with Varian EPID's were only exhibited for extreme cases and is not believed to have any clinical relevance. Hence the ghosting effect have been ignored for all experiments performed in this thesis.

2.12.7 Field size dependence

A field size dependence of EPID was noted to be different with respect to dose measured with an ion chamber in a water phantom. The EPID was compared to ion chamber readings normalised to the field size of 10 x 10cm^2 as shown in Figure 2.23. Second order polynomial fit was applied to the data which showed a field size response relative to the ion chamber of -2% for a 4 x 4cm^2 field and +2.5% for a 24 x 24cm^2 field [42, 43].

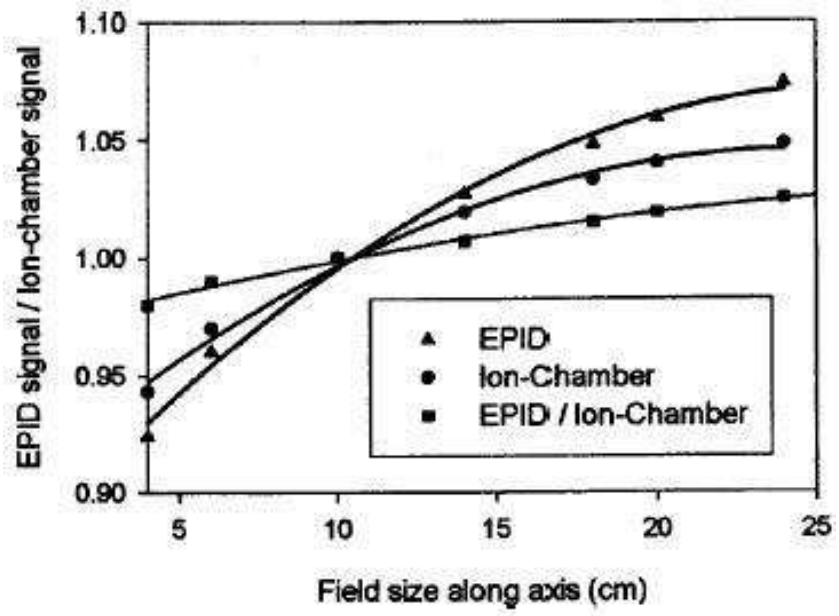

Figure 2.23: Field size response of the EPID. The EPID signal change with the field size is compared to the change in dose with field size measured with an ion chamber at 1.5cm depth in a solid water phantom. Data is normalised to the 10 x 10cm^2. (Graph taken from Greer et al. Med. Phys.(2003) [42])

Grein at al. developed empirical corrections to compensate for similar observed effects [45]. The causes of the differential response of EPID (Gd_2O_2S sensitive volume) with ion chamber are reported to be the varying energy absorption and spectral scattering properties of the different atomic compositions that make the detector and the surrounding

media. Since the behaviour of EPID although different from ion chamber was found to be self-consistent at different source to detector distances (SDD) and with ability to apply the concept of equivalent field size, the field size dependence can be modelled through a single analytical function. It was concluded that although the field size dependence of the EPID differed from that of an ion chamber in water phantom, it was useful for relative dosimetry.

2.12.8 Build up depth

In an attempt to improve the accuracy of dosimetry data acquired using an EPID it was important to investigate the effects of build up material in addition to the inherent buildup of 1mm copper plate and the scintillator plate. Alongwith determining the influence of the material, the required thickness of the build-up layer has also been investigated by a number of researchers [42, 43, 39].

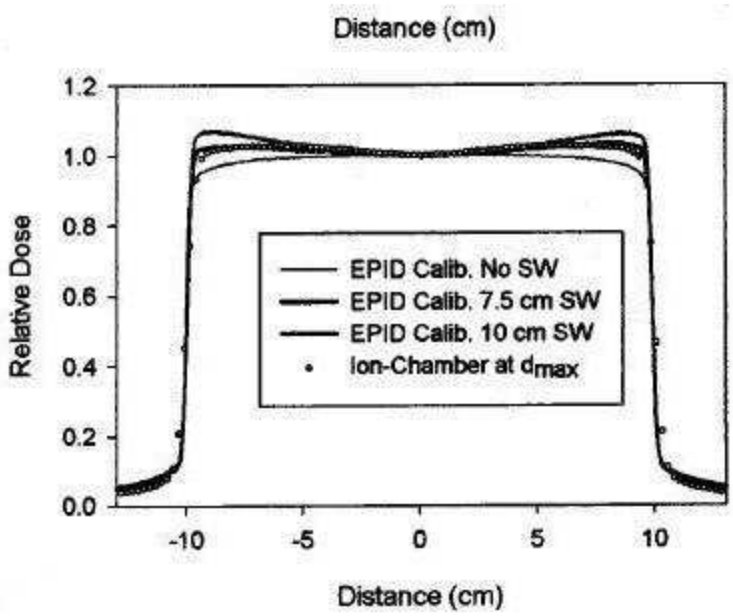

Figure 2.24: EPID image profiles (without build up) through the central axis of an open 20 x 20cm^2 field. The EPID images have been divided by the FF calibration images taken with the three different buildup thicknesses. These open field profiles are compared to ion-chamber measurements at d_{max} depth in a water phantom (Results taken from Greer et al. Med. Phys. 2003 [42])

These experiments highlighted the benefits of using Cu as a buildup material for absorption of patient scatter at smaller air-gaps. However, additional buildup was shown to have adverse effects on the image quality [39]. Greer et al. reported an optimal buildup of 0.5cm for 6 MV where a reduction in signal was observed for larger thicknesses as shown

in Figure 2.24. The EPID signal corresponding to no extra buildup was found to be within 1% of the maximum due to the inherent buildup. Besides the effect of the extra buildup was only evident in a slight blurring of the penumbra. Hence it was concluded that for dosimetric measurements without a patient or scattering material additional buildup was not required. Therefore no extra buildup has been used for any dosimetric measurements performed here.

Although, the use of buildup is not required in absence of scattering material and is not conventionally used in calibration, it does have its advantages. It ensures that the measurements are made beyond the dose maximum and also helps in attenuation of scattered radiation from the patient when present. But, this is not very desirable either, firstly, since it would compromise the efficiency of a clinical routine, secondly as it would be restrictive for non-zero gantry positions. It is believed that although measuring in high gradient region is not desirable the addition of buildup will neither facilitate nor complicate the prediction of PD. Even if the depth is not accurately known, it is accurately fixed leading to reproducible data. However, this belief is only applicable when compared to predicted dose images, hence poses limitations for absolute dosimetry.

2.12.9 Other characteristics

Other characteristics of aSi EPIDs have been studied for some prototypes. EPIDs were shown to exhibit excellent short term stability with some influence of warm up effects [46]. The reproducibility of aSi EPIDs at the central pixel region was found to be better than 0.5% (1 SD) when tested over a period of 23 months [22]. Louwe et al. showed that aSi EPID response is independent of temperature fluctuations. However, some degradation of the imager response was shown over longer periods which was fully explained by temperature effects and radiation history. This proved that the EPID response was not influenced by any other factors [22].

2.13 Linac QA tool

It could be sometime before portal dosimetry can be implemented clinically. Meanwhile many centres have been using EPID effectively for QA of beam properties and as a film replacement. However an extensive literature and set methods for QA could not be found. Therefore, we have studied the potential applications of EPID as a linac QA tool to perform routine verification of linac beam properties and also for reduced film dependence. Since clinical imaging is almost digital, wet processing and films are rapidly being phased

out, use of EPID for these tests would be extremely beneficial.

The following chapter details the experimental methods adopted to perform measurements to further study the characteristics of EPID as a dosimeter for better adaptation at WBCC and also its use in linac QA.

Chapter 3

Experimental Methods

This project is an investigation of portal dosimetry with the aim to study some dosimetric characteristics. Some potential applications for linac QA using electronic portal imaging device (EPID) as a QA tool have also been explored. Experiments and feasibility studies were performed to study the behaviour of EPID in various conditions such as under varying dose rate specifically for dynamic wedge treatments. The effect of calibration distance was studied for better dosimetric accuracy. Experiments were also performed to study the behaviour of EPID for asymmetric fields, linearity and short term repeatability of the detector. Potential for use of EPID as a QA tool was explored for reduced film dependence and also for other routine dosimetric linac QA.

All measurements were performed on an amorphous silicon, aS500 EPID (Varian Medical Systems) mounted with an R-arm on a Varian clinac 2100C/D, sn 1027. The clinac is equipped with 120 multileaf collimators (Millenium MLC, Varian Medical Systems). The PV Client software version was 6.1.13 with IAS2 software version 6.1.11 and the detector IDU11 model. The treatment planning system (TPS) used is Eclipse (Varian, Palo Alto, CA), Vision applications version 7.3.10 and AM Maintenance version 7.1.2005.628. This work was done in the WBCC treatment room without any modifications to the bunker. Some modifications to linac to enable EDW acquisition were made which are detailed in Appendix B.

While some of these tests appear in literature and in depth analysis has been published, it was necessary to verify that the EPID at WBCC functioned in a similar way as expected. Hence some of the tests below were performed as spot checks to assure proper functioning.

3.1 Dosimetric characteristics

3.1.1 Linearity with MU

To verify the linear response with dose, images of a 10 x 10cm^2 open field were acquired. The EPID was placed at a fixed detector distance of 150cm, and varying dose was delivered

with monitor unit (MU) settings of 10, 20, 50, 100, 150 and 200. For each monitor unit settings an integrated image was acquired. The integrated response of EPID after dosimetric calibration is displayed as calibrated units. A median of Calibrated Units (CU) of 11 x 11 pixel region on the central axis was recorded.

3.1.2 Dose rate linearity

The linearity of EPID to dose rate variations was verified against the results from literature. To modify the dose rate the SDD was varied by varying the distance of EPID below the isocentre. The EPID was placed at 5, 10, 20, 40, 50, 60.1, 70, 83cm below the isocentre. At each distance a dose of 100 MU was delivered to a 10 x 10cm^2 open field, integrated image was acquired and median of CU for 11 x 11 pixel region on the central axis was recorded for 6 MV beam at 600 MU/min.

3.1.3 Short term repeatability

The short term repeatability of the EPID was evaluated for 10 consecutive images acquired for a 18 x 18cm^2 field delivering 100MU for each image acquisition. Only time elapsed between two consecutive image acquisition was the time to set up the second acquisition (order of 10-15 seconds). Some images were also acquired after repositioning the imager (i.e. retracting and positioning it back). All images were acquired at SDD= 150cm.

3.1.4 Effect of calibration distance

The saturation characteristics of the EPID is a limitation in use of dose rates higher than 300 MU/min at distances shorter than 140cm. At WBCC, 600 MU/min is the typical dose rate used for most patients. Hence to be able to use EPID for dosimetry in the centre a work around was required. This study was undertaken to evaluate the effect the calibration distance has on dosimetric accuracy. Dosimetric images at SDD = 150cm were acquired with the detector calibrated under two different conditions. The typical source to detector distance used at WBCC is 150cm, hence the SDD = 150cm was agreed upon for measurements of this study. Firstly, calibrations at the Varian recommended distance of SDD = 105cm were performed and this method will be referred to as 'Varian method' further in this thesis. Secondly, keeping the calibration position same as the typical measurement distance of SDD = 150cm and this is henceforth called 'WBCC method' of calibration. The profiles obtained from these images were then compared with the profiles acquired in water phantom using semiflex ion chamber.

Half diagonal profiles were acquired using a semiflex 0.125cc ion chamber in a water phantom at two different SSDs for dosimetric calibration of EPID. Varian recommends acquiring a half diagonal profile at SSD = 100cm, D_{max} = 1.5cm , for the largest field size of 40 x 40cm^2. For calibration using WBCC method half diagonal profile at SSD = 148.5cm, D_{max} = 1.5cm (SDD = 150cm), field size of 40 x 40cm^2 was acquired. This was performed with the water tank set-up to acquire only one quadrant to enable acquisition of the entire magnified field. Half diagonal profiles of the largest field in all four quadrants were compared to verify the symmetry of the beam, hence justifying the use of any one diagonal. Also the half diagonal profile acquired at SSD = 100cm was compared to the half diagonal profile obtained at SSD = 148.5cm to justify the experimentation.

Dosimetric calibration of EPID under 'Varian method' was performed as per the conventional Varian recommended set-up conditions explained in chapter 2. So dark field and flood field were acquired at SDD = 105cm. The flood field was acquired with 6cm buildup to avoid flood field saturation (this is not part of the recommended procedure). Buildup material was placed on the couch positioned at the highest position. The beam correction was performed using the diagonal profile acquired at SSD = 100cm, D_{max}. The dosimetric calibration was performed at SDD = 105cm delivering 100MU to a field of 10 x 10cm^2 and dose normalized incorporating the inverse square factor. The procedure was repeated for WBCC method with calibrations performed at SDD = 150cm. Both dark field and flood field were acquired at SDD = 150cm (img vrt = -50, long = 0.0 , lat = 0.0) and beam correction performed using the diagonal profile obtained at SSD = 148.5cm D_{max} = 1.5cm. The dosimetric calibration was done at SDD = 150cm delivering 100MU to a field of 10 x 10cm^2 and accounting for the inverse square correction. Buildup material of 6cm thickness was placed on the couch for flood field acquisition.

Measurements were made by scanning profiles using semiflex ion chamber in a water phantom for a 6MV beam using a repetition rate of 600MU/min, at SSD = 148.5cm, D_{max} = 1.5cm for field sizes of 10 x 10cm^2 and 18 x 18cm^2. EPID measurements were made by acquiring images under similar set-up conditions delivering 200MU at SDD = 150cm (img vrt = -50) for open fields of 10 x 10cm^2 and 18 x 18cm^2. These images were analysed to obtain radial profiles which were compared to the radial profiles acquired using semiflex ion chamber.

The EPID was then calibrated for Varian and WBCC method without using any additional buildup for flood field acquisition, keeping the rest of the set-up same. All the

measurements were repeated for this calibration procedure. The profiles thus acquired were compared to the semiflex profiles. Table 3.1 details the set-up conditions used for the calibration of EPID and also for the profile measurements obtained.

Table 3.1: Parameters used to evaluate effect of calibration distance

Measurement type	**Varian method**	**WBCC method**
Half diagonal profile using semiflex	SSD = 100cm, depth = D_{max} (1.5cm), 40 x 40cm^2	SSD = 148.5cm, depth = D_{max} (1.5cm), 40 x 40cm^2
EPID calibration	with (6cm) and without buildup for flood field only	with (6cm) and without buildup for flood field only
	SDD = 105cm; inverse square factor (dosimetric calibration = 0.907)	SDD = 150cm; inverse square factor (dosimetric calibration = 0.444)
Measurements using semiflex	SSD=148.5cm; D_{max} (1.5cm); open fields: 10 x 10cm^2 & 18 x 18cm^2	
EPID Measurements	SDD = 150cm; open fields: 10 x 10cm^2 & 18 x 18cm^2	SDD = 150cm; open fields: 10 x 10cm^2 & 18 x 18cm^2

3.1.5 Behaviour with varying dose rate

To study the behaviour of EPID under varying dose rate we compared profiles from the acquired images of an EDW field with profiles measured in a water phantom using PTW linear array LA48.

PTW Linear Array LA48 consists of 47 detectors embedded in it. These detectors enable acquisition of an EDW profile. Figure 3.1 is an image of LA48. The LA48 array requires calibration against a single chamber to eliminate the effect of any differences in response of the 47 individual detectors/channels. The calibration is performed under identical measuring conditions against the semiflex ion chamber at depth= D_{max}). The calibration factors for LA48 are calculated by the system and stored in a calibration file.

To acquire EDW profiles using linear array LA48, it was necessary to be confident

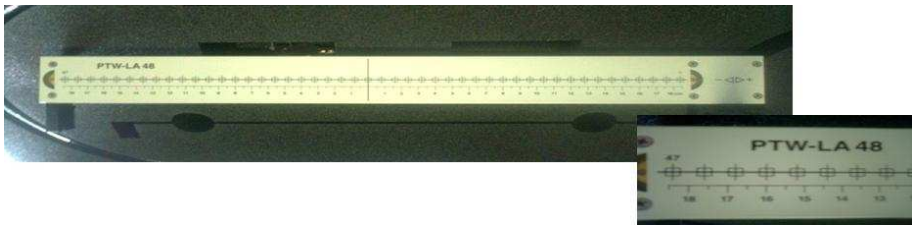

Figure 3.1: PTW Linear Array LA48

that the response of LA48 was similar to semiflex ion chamber, in order to validate the use of LA48. Hence, measurements using semiflex and LA48 were acquired under similar conditions, i.e. SSD = 100cm, depth=1.5cm (D_{max}), for a field size of 10 x 10cm^2. PTW Linear Array LA48 was henceforth used for all EDW measurements in water phantom.

Profiles were acquired at SSD = 148.5cm, D_{max}= 1.5cm for EDW fields in the wedged direction for field size of 10 x 10cm^2 & 18 x 18cm^2 and EDW angles of 60°, 45°, 30° & 15°. These profiles were then compared with profiles of images obtained with EPID at SDD = 150cm calibrated using the Varian method and using the WBCC method for the field sizes of 10 x 10cm^2 & 18 x 18cm^2 and EDW angles of 60°, 45°, 30° & 15°.

Table 3.2: Measurement conditions for EDW profiles

Measurement type	**Varian method**	**WBCC method**
EPID calibrations	SDD = 105cm, with and without 6cm buildup for flood field only	SSD = 150cm, with and without 6cm buildup for flood field only
EPID measurements	SDD = 150cm; 10 x 10cm^2 & 18 x 18cm^2, EDW angles 60°, 45°, 30°, 15°	
LA48 measurements	SSD = 148.5cm; depth = D_{max}; 10 x 10cm^2 & 18 x 18cm^2, EDW angles 60°, 45°, 30°, 15°	

3.1.6 Asymmetric field profiles

The measurements for the study of calibration distance and EDW profiles were performed for fields symmetric about the central axis. The EPID calibration process does not, at any point register position of the EPID with respect to the central axis. Response of the

EPID is known to be field size dependent, and the pixel sensitivities are also known to vary with off axis distance. With all these factors, it was necessary to see how the EPID treated asymmetric fields. Does the EPID incorporate the beam horns appropriately and does it know the central axis position to incorporate the beam horns?

A study was performed for profiles of asymmetric fields to answer the above questions. Some open field and EDW profiles using semiflex and LA48 respectively for asymmetric fields were acquired as per Table 3.3. The asymmetry was introduced on the upper jaws in the radial direction and radial profiles were measured using semiflex. These profiles were then compared to the profiles acquired using EPID under similar conditions with Varian and WBCC method of calibration. The WBCC method was used in symmetric and asymmetric modes, i.e. EPID calibrated with symmetric and asymmetric fields. For asymmetric mode of calibration the detector was displaced in the longitudinal direction to encompass the entire asymmetric field. Even though calibration was performed in two modes, the measurements were always done in asymmetric mode. The field size used was Y1 = 1, Y2 = 17, X = 18 (symmetric), hence giving us a 18 x 18cm^2 field size.

Table 3.3: Parameters for measurements of asymmetric fields

	Varian method	**WBCC method**
Symmetric calibration	SDD = 105cm, EPID center aligned to beam central axis (CAX)	SDD = 150cm, EPID center aligned to beam central axis (CAX)
	without any buildup for flood field	
Asymmetric calibration	–	SDD = 150cm; img lng = -11.4cm, flood field acquired with jaws set asymmetrically about central axis to cover the detector
LA48 measurements	SSD=148.5cm; D_{max} (1.5cm); 18 x 18cm^2 (open & EDW fields); lower jaws = 18cm; Y1 = 1cm; Y2 = 17cm	
EPID measurements	SDD=150cm; img lng = -11.4cm; 18 x 18cm^2 ; (open & EDW fields) lower jaws = 18cm; Y1 = 1cm; Y2 = 17cm	

3.2 Applications for linac QA

3.2.1 Output constancy

The output of linac is checked daily using the Keithley tracker which has five detectors including one on the central axis. The Keithley tracker is set-up at SSD = 110 cm, for a field size 22 x 22cm^2 delivering 120 MU. However, the set-up is irrelevant here, as what is analysed is the constancy of the readings day after day. These readings obtained from Keithley tracker were compared to the response of EPID for 10 consecutive days of measurements.

A patient was set-up in Vision, with two fields. Firstly, a 6 MV open field of 18 x 18cm^2 with 120 MU was delivered on a daily basis. Secondly, the same field delivering 100 MU and 60° EDW was acquired. These were then analysed using Matlab. These images were also used to evaluate the following tests for routine linac quality assurance. Constancy of linac output was evaluated by analysis of these images.

3.2.2 Wedge factor constancy

The wedge factors were calculated using the above obtained EDW fields and open fields for the same field size under similar conditions. All images are acquired for a 6MV beam and factors measured for a 60° & 45° for a 10x10cm^2 & 18 x 18cm^2 field.

3.2.3 Wedge angle constancy

Measuring wedge angle is extremely tedious and cannot be done accurately on a routine basis. At WBCC, verification of wedge angle constancy is done via an indirect method. The Keithley tracker is used to measure the ratio of outputs at two points equidistant from the central axis on the profile and the constancy of symmetry is accepted as a constancy of wedge angle. In this work, EPID as a tool to verify the constancy of wedge angle is studied. The concept followed is the same as Keithley, by verifying constancy of symmetry of the profile. Therefore, EDW profiles were acquired for 10 consecutive days. The profiles are acquired at SDD = 150cm, for a 18 x 18 cm^2.

3.2.4 Flatness & Symmetry

The flatness and symmetry were also calculated with the images obtained for 10 consecutive days according to the Varian definition. These measurements were only investigated with the purpose of testing the feasibility of the EPID for daily linac QA. Therefore in

depth analysis is not conducted. However, following the IEC recommendations of evaluating over an area of less than 1cm^2, we have taken an average of 5x5 pixel region. The flatness and symmetry thus calculated are compared to the Keithley tracker measurements, which calculates the constancy of flatness and symmetry of the linac beam. Keithley tracker measures output at 5 set positions, and calculates flatness and symmetry using the two opposite equidistant points from the central axis.

3.2.5 Coincidence of light field vs radiation field

A QA patient is created and set-up in Varis/Vision to facilitate ease of repeated measurements and also simplify the evaluation process. The gantry angle used were 0° and 180°, a phantom plate of 22 x 22cm^2 was placed on the couch at 100cm SSD. The phantom has 1mm diameter steel balls inserted in it at the edges of various field sizes and also at the center. This test was developed by The IRO Medical Physics and Engineering Group and hence was verified in this study for feasibility of using EPID as a film replacement for testing coincidence of light field vs radiation field [47].

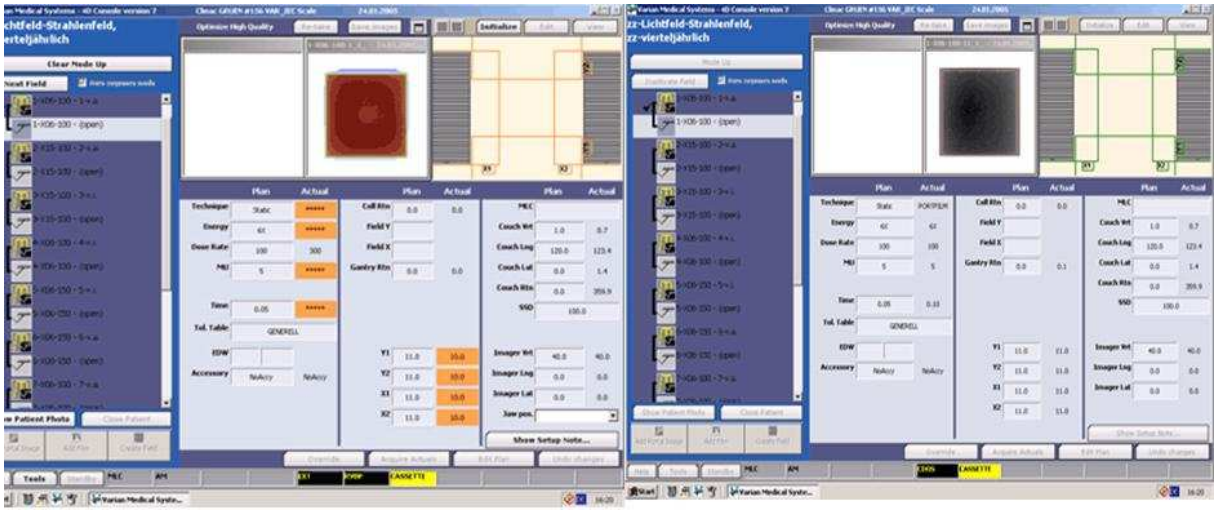

Figure 3.2: 'Integrated' image and 'after' image

The jaws are aligned to the marks on the phantom such that the 50% edge of the light field coincides with the marks center, as nearly as possible. This is not much different than scribing lines on the films. The patient is then treated and images acquired. We acquire two images, one integrated image which is acquired during the treatment and then an 'after' image which opens the jaws by 1 cm and acquires an image. The reason for opening the jaws by 1cm is to be able to analyze the discrepancy between light field

and radiation field, even if the radiation field is smaller than the light field, when it will not be possible to image the steel balls. These images are then analyzed in the review workspace of Vision.

3.2.6 Verification of independent jaw calibration

This test is performed to verify the calibration of independent jaws and their alignment with the central axis. Any overlap / gap seen between the jaws indicate the need for their re-calibration. A test patient was set-up in Vision. Here, 4 separate images of 8 x $8cm^2$ field covering the four quadrants of a 16 x $16cm^2$ area are acquired. Edge of each individual image is detected and dose profiles plotted. This profile gives us the start and end positions or co-ordinates of the edges. So, this information for each quadrant gives us an accurate measurement of the gap or overlap present between them (Figure 3.3).

Another way of evaluating overlaps between jaws is to 'combine' the two quadrant images, find their edges and measure the distance between them, as shown in figure 3.4. However, this method works well for overlaps but has discrepancies when it comes to measuring gaps between jaws as the edge detection fails to differentiate between the two quadrants.

A known gap and overlap of 1cm, 0.4cm, 0.2cm, 0.1cm were introduced and images were acquired over a one month period. Images were acquired without introducing any gap or overlap and compared to the conventional method of using films. The jaw settings for quadrant 1 are shown in the table below. The results of this study are presented in chapter 4.

Table 3.4: Jaw settings for 4 quadrants

Jaw	Quadrant 1(Q1)	Quadrant 2 (Q2)	Quadrant 3 (Q3)	Quadrant 4 (Q4)
X1	5cm	5cm	0cm	0cm
X2	0cm	0cm	5cm	5cm
Y1	5cm	0cm	0cm	5cm
Y2	0cm	5cm	5cm	0cm

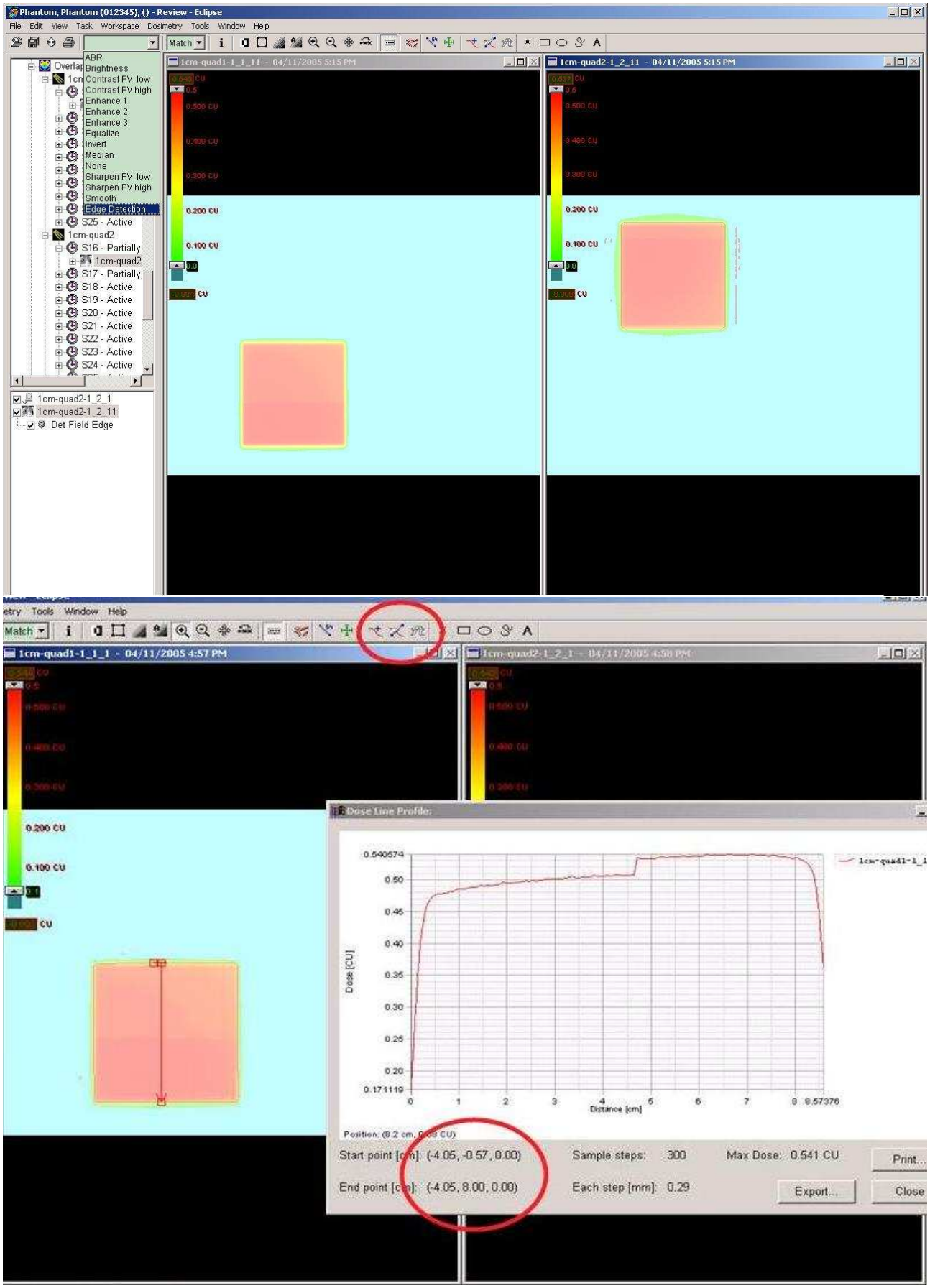

Figure 3.3: 4 Quadrant imaging

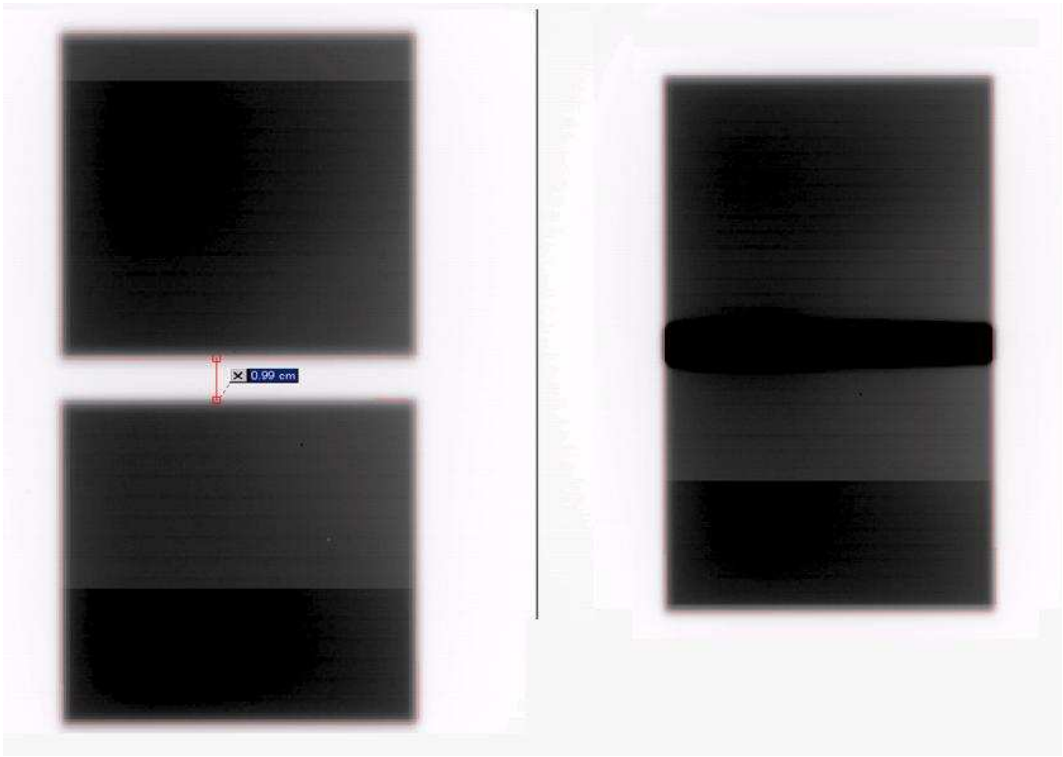

Figure 3.4: 'Combine' images

3.2.7 Verification of radiation isocentre

The radiation isocentre of the linac needs to be verified routinely. This is done with collimator and gantry rotation about a sphere of 1mm radius. This test is conventionally performed with the use of films.

Collimator spoke shot

A QA patient was set-up in TPS, a plan was created with the upper jaws opened to 40cm and the lower collimator jaws were closed to give a slit of 0.5cm width symmetrically. Images were acquired with collimator angles 0°, 60°, 120°, 270° & 330° as shown in Figure 3.5. These images were then reviewed and analyzed in the Dosimetry workspace under Review Task.

Gantry spoke shot

To verify the gantry rotation using EPID, needs to account for various factors like the EPID sag. The offset and the magnification due to gantry rotation need to be separated from the sag of the EPID, the pixel values need to be rescaled, image orientation and

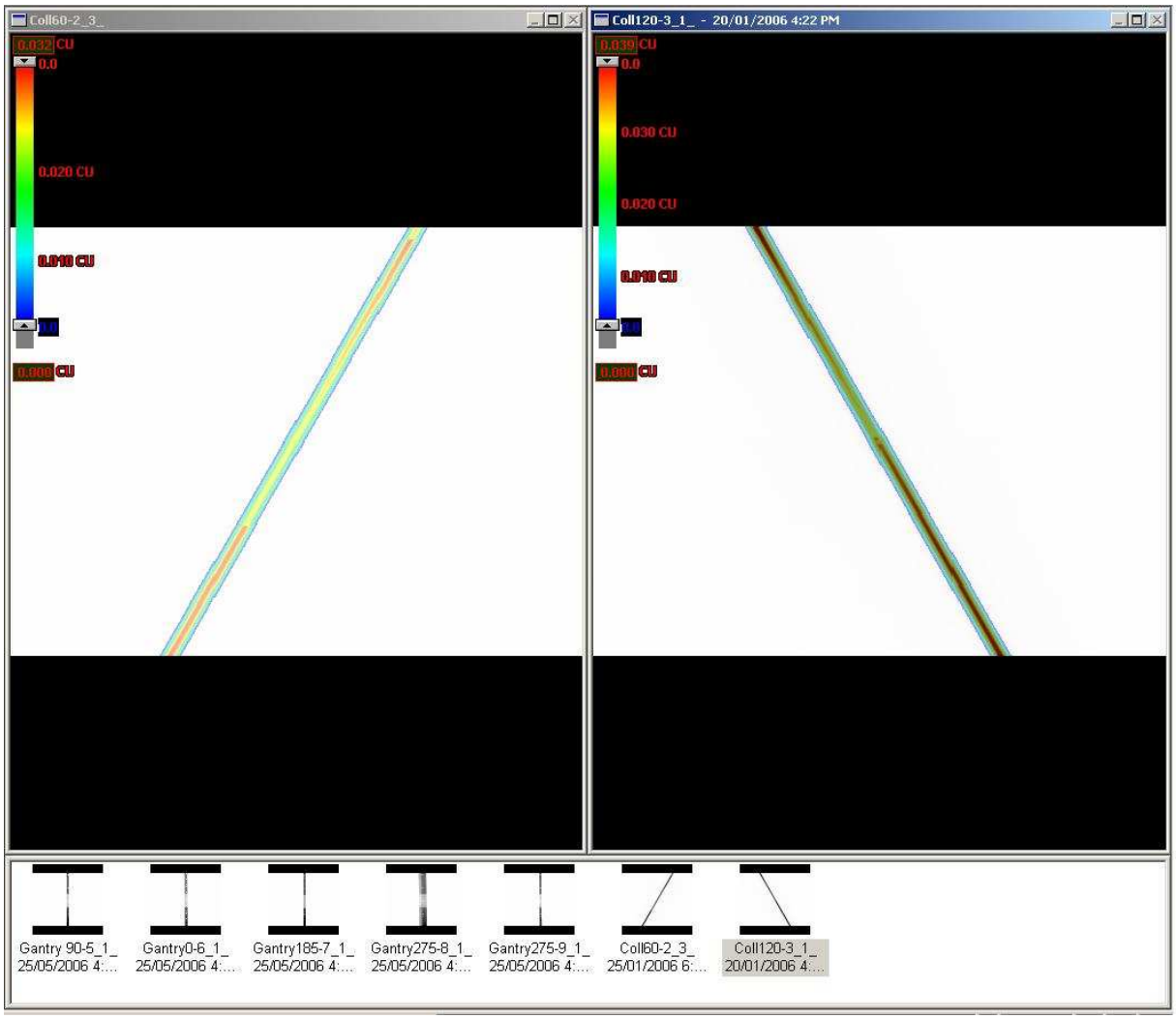

Figure 3.5: Collimator rotation images

alignment to be consistent. Therefore, to separate the sag of EPID and gantry an external independent source is required. Hence images were acquired with a port film graticule fixed at the treatment head and using a phantom placed on the couch at SSD = 100cm. The phantom has a 2mm diameter steel ball inserted in it, this is aligned with the central cross hair indicating the central axis. The relative difference between the graticule center and the center of the ball embedded in the phantom can be evaluated to test for gantry rotation about a sphere. The effect of gantry and EPID sag can then be ignored, as the images acquired for the external source would be independent of the detector position.

Chapter 4

Results

The measurements were processed using Matlab for dosimetric aspects and Vision for some optical applications. Vision is used to take a simple approach so as, not to complicate the QA by adding use of another software and hence keeping it efficient for routine analysis.

4.1 Dosimetric characteristics

4.1.1 Linearity with MU

The images acquired using the EPID for different monitor units were analysed using Matlab. An average of a pixel region of 9 x 9 pixels was calculated for each image obtained. These factors were then plotted against the respective monitor units to study the proportionality of the detector.

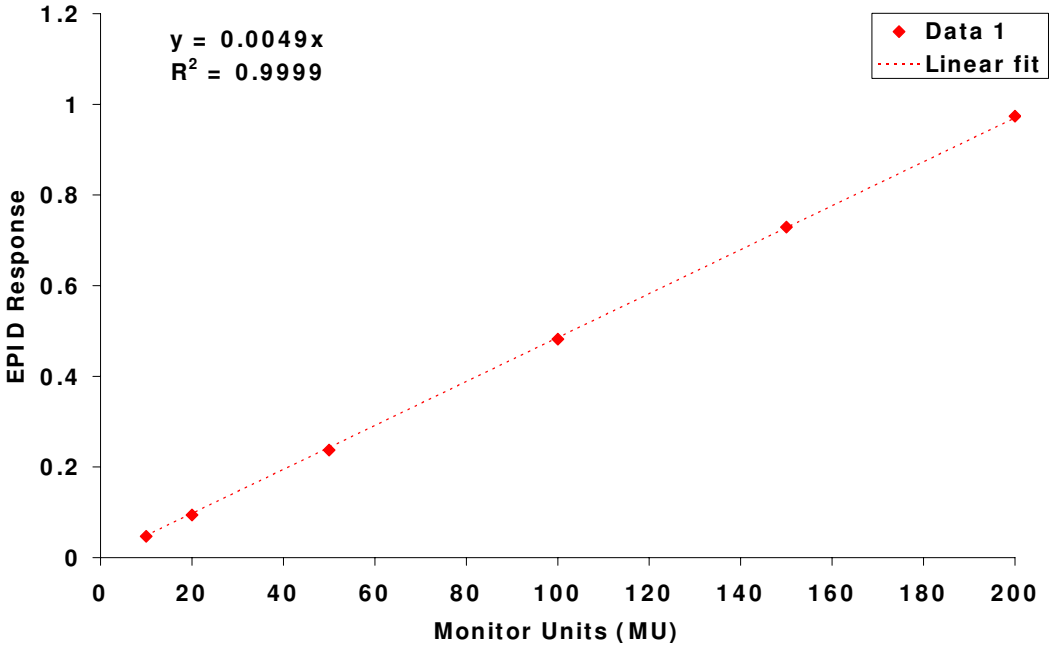

Figure 4.1: Proportionality of the detector response with monitor units measured for 6MV, 600MU/min with varying MU at SDD = 150cm

The detector exhibits excellent linearity with monitor unit (MU) as shown in Figure 4.1. A linear function was fit to the data using an equation:

$$y = 0.0049 * x \tag{4.1}$$

A linear regression analysis produced a co-efficient of determination $R^2 = 0.9999$. The linear fit gives a proportionality constant of 0.0049 proving that the detected portal dose is proportional to the amount of MUs over the entire measured range from 10 MU to 200 MU.

4.1.2 Dose Rate Linearity

The images were obtained at different SDD's delivering 100MU at a repetition rate of 600MU/min. These images were analysed, the mean value of the central 9x9 pixel region was caluclated and plotted. The distance from the source to the detector gives a inverse square factor which can then be converted into dose rate (Gy/min).

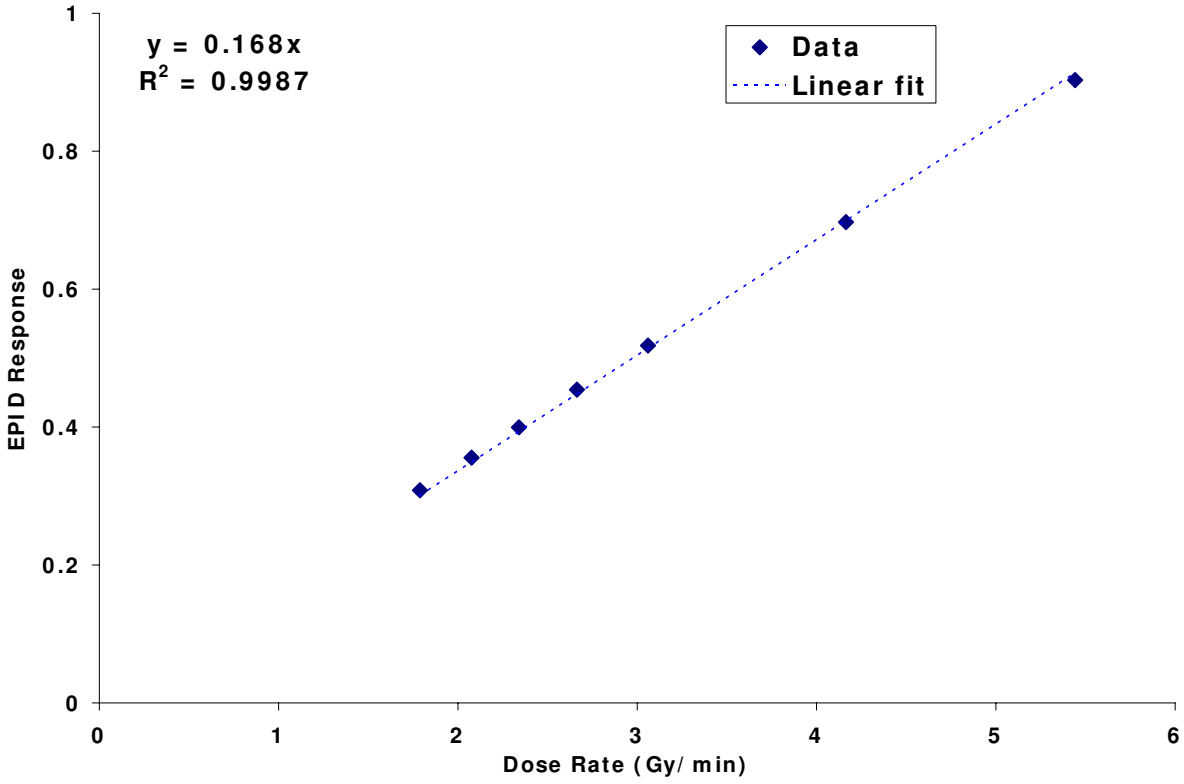

Figure 4.2: Dose rate linearity of detector measured for 6MV at varying SDD's for a field size 10 x 10cm^2 delivering 100MU for each acquisition

This data is plotted as shown in Figure 4.2. A linear function was fit to the data using an equation:

$$y = 0.168 * x \tag{4.2}$$

The linear regression analysis produced a co-efficient of determination $R^2 = 0.9987$. The linear fit also gave a proportionality constant of 0.168 showing that the detector is proportional over the entire measured range and does not deviate from the inverse square behaviour.

4.1.3 Short term repeatability

The short term repeatability of the detector was studied with 10 consecutive images acquired at SDD = 150cm for a field size of 18 x 18cm^2. The mean value of the central region was then compared to find excellent short term repeatability giving a standard deviation of 3.17 x 10^{-4}. A student t-test with 9 degrees of freedom corresponding to 95% confidence interval gave a mean value of 0.480 CU $\pm$ 2 x 10^{-4}. Figure 4.3 show the comparison of the profiles obtained from the 10 images. The central region has been magnified to show the different profiles in Figure 4.4.

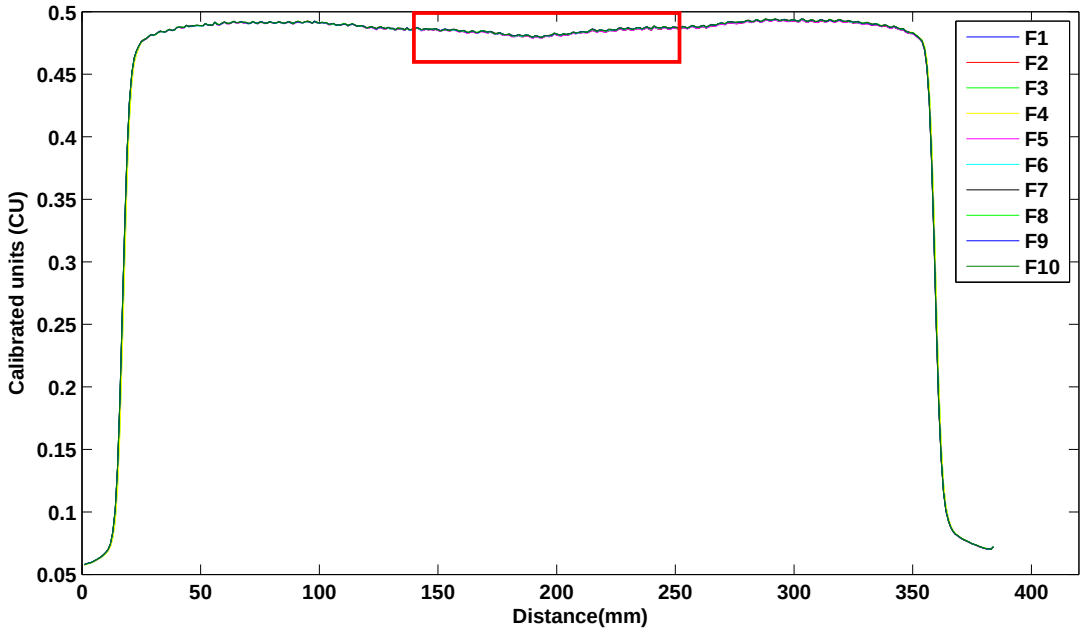

Figure 4.3: Central axis profiles of 10 consecutive images acquired for a field size of 18 x 18cm^2 at SDD = 150cm.

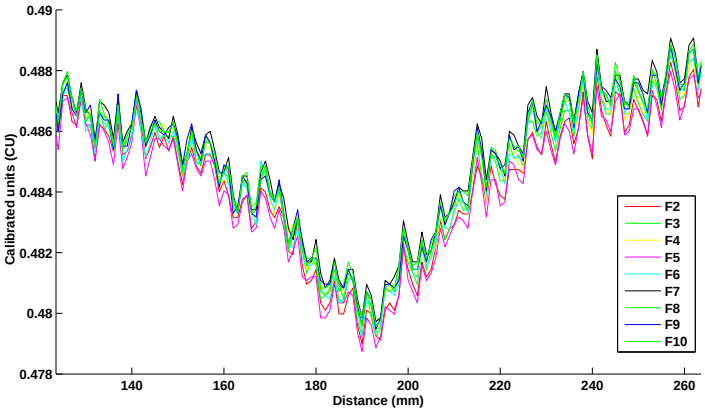

Figure 4.4: Magnified central region of the profiles acquired for short term repeatability.

4.1.4 Effect of calibration distance

Half diagonal profiles of the largest field (40 x 40cm^2) acquired using the semiflex ion chamber in all four quadrants of the beam orientation were compared. Figure 4.5 shows very good agreement between the half diagonal profiles compared for all beam quadrants proving good symmetry of linac and validating the choice of diagonal orientation.

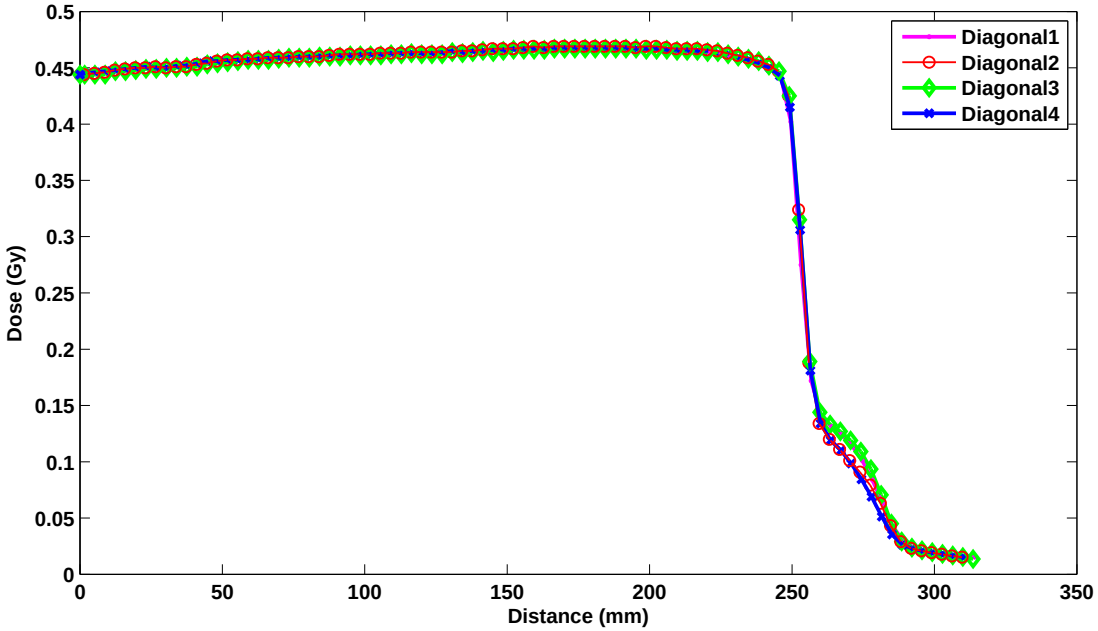

Figure 4.5: Half diagonal profiles for all 4 quadrants acquired using semiflex ion chamber at SSD = 100cm depth= D_{max} for a 40x40cm^2 field

Half diagonal profiles obtained to correct the beam profile of the EPID for dosimetric calibration were also compared. These profiles were acquired at SSD = 100cm (green) for Varian method and SSD = 150cm (red) for WBCC method. Figure 4.6 shows a comparison of the profiles acquired at two SSD's demonstrating a 2% variation between these diagonals. A 2% variation in a calibration profile could result in bigger deviation in measurements compromising the dosimetric accuracy. These half diagonal profiles are used for dosimetric calibration of EPID under Varian method and WBCC method respectively.

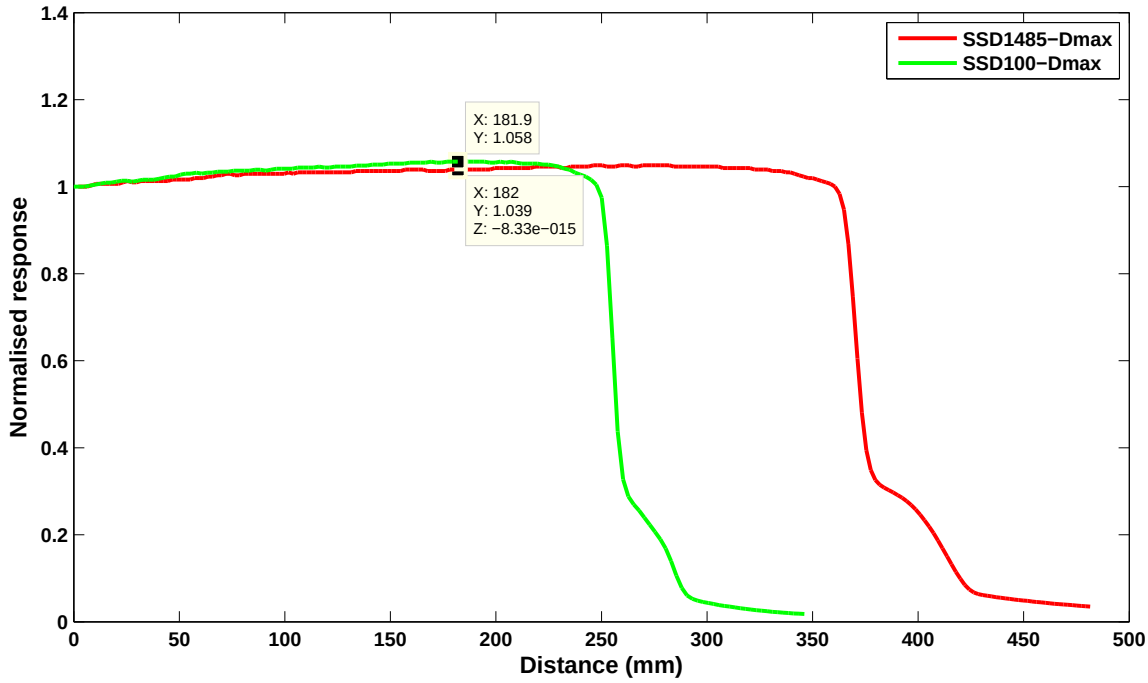

Figure 4.6: Half diagonal profiles acquired using semiflex ion chamber at SSD = 100cm and SSD = 148.5cm for 40x40cm^2 field

The radial profiles measured at SDD = 150cm using semiflex and EPID, when EPID was calibrated using Varian and WBCC method were normalised at central axis (CAX). The following figures show comparison of these radial profiles acquired at SDD = 150cm for field sizes of 10x10cm^2 and 18x18cm^2.

Open field profiles acquired using 6cm of buildup for flood field calibration of EPID under two calibration methods namely Varian method and WBCC method can differ upto 1.5% as shown in Figure 4.7 and 4.8. However, it is also clear that the maximum difference between any open field EPID measurement and LA48 is within 1%. The 'shoulders'

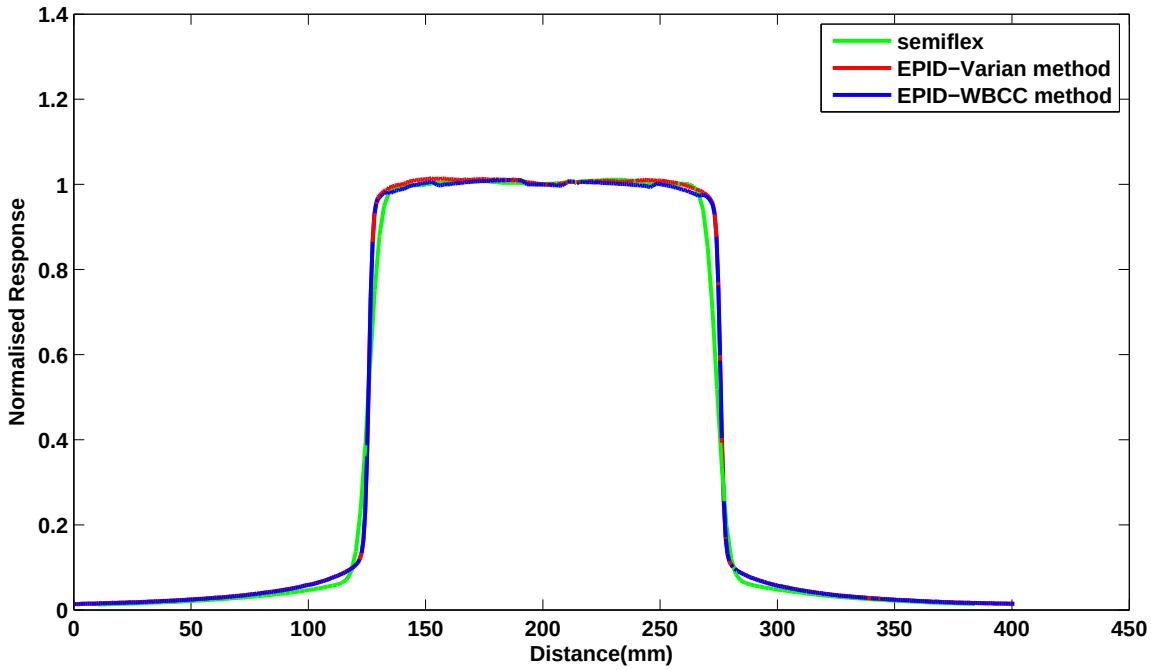

Figure 4.7: Comparison of 10 x 10cm^2 open field profiles acquired with semiflex & EPID using 6cm buildup for flood field

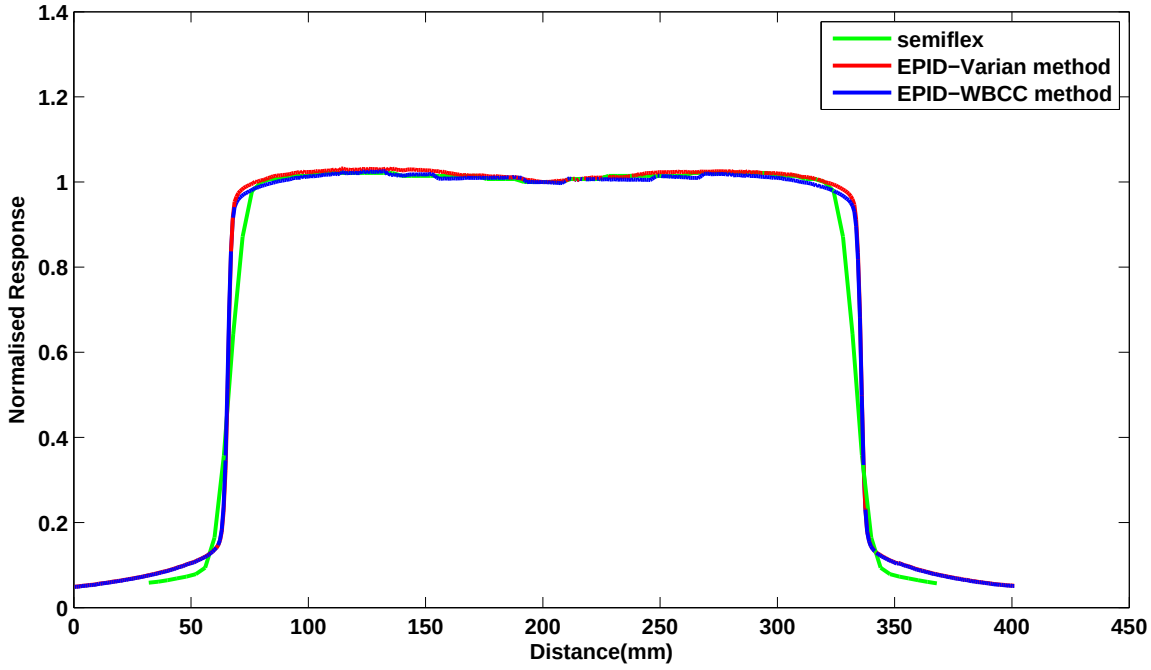

Figure 4.8: Comparison of 18 x 18cm^2 open field profiles acquired with semiflex & EPID using 6cm buildup for flood field

of the EPID profiles show almost a 3mm discrepancy from the profiles acquired using semiflex. The EPID profiles seem to be more rounded than the ion chamber profiles. A deviation in the tails of the profiles is evident in addition to some overlaying discrepancy in the penumbra region.

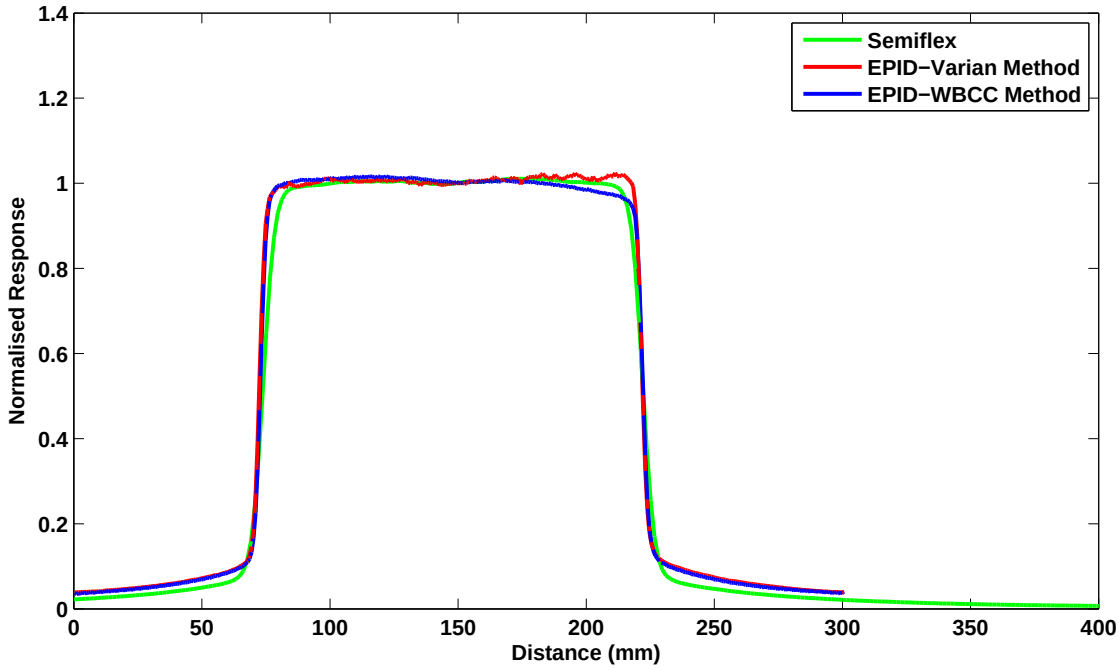

Figure 4.9: Comparison of 10 x 10cm^2 open field profiles acquired with semiflex & EPID without buildup for flood field

Open field profiles acquired without using any buildup for flood field calibration of EPID differed up to 8% from the LA48 profile when calibrated using Varian method. These profiles also showed unacceptable distortions. The distortions worsened with increase in field size. However, when the EPID was calibrated using the WBCC method, the profiles agreed with ion chamber measurements to better than 1% without any noticeable distortions as seen from Figure 4.9 and 4.10. The discrepancy seen in the shoulder region for profiles with use of buildup for flood field did not appear in these profiles. Although, the penumbra region did show similar overlaying discrepancies as with use of buildup. The results are tabulated in Table 4.1.

The EPID profiles exhibit a deviation from the ion chamber profiles at the tail beyond the penumbra region in addition to the non-zero values of the EPID profiles. Also noticed

are the shorter tails of EPID profiles as compared to ion chamber for field sizes 18x18cm^2.

Table 4.1: Comparison of profiles obtained using semiflex and EPID with two calibration methods

Measurement type	**Varian method**	**WBCC method**
with buildup	1%	1%
without buildup	up to 8%	approx 1%
Distortion (without buildup)	unacceptable	none

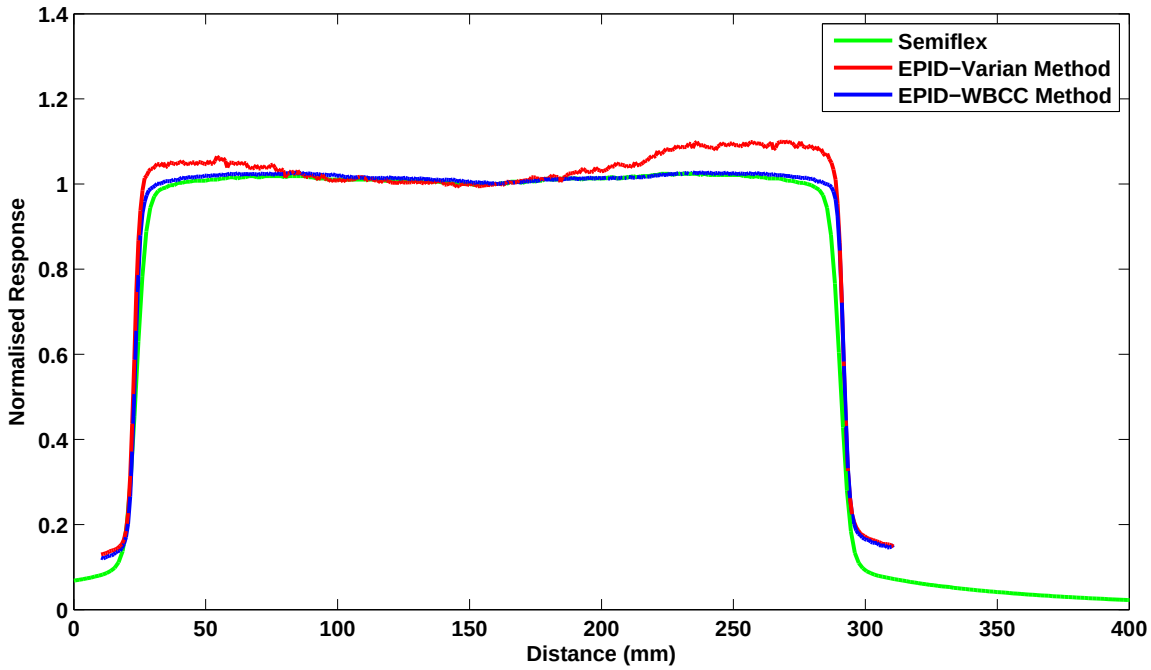

Figure 4.10: Comparison of 18 x 18cm^2 open field profiles acquired with semiflex & EPID without buildup for flood field

4.1.5 Behaviour with varying dose rate

The excellent agreement between the response of the two devices namely semiflex ion chamber and LA48 justified the use of LA48 for further use in EDW profiles. Figure 4.11 shows a comparison of response of LA48 against semiflex 0.125cc ion chamber measured at SSD = 100cm for a 10x10cm^2 field, depth = D_{max}.

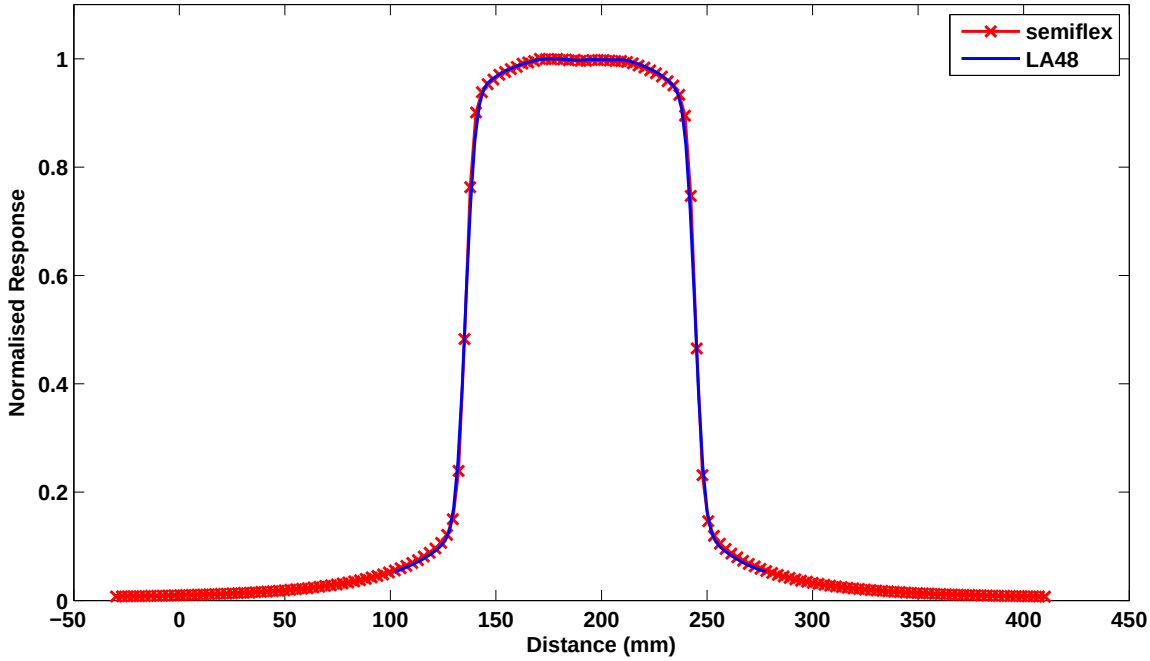

Figure 4.11: Response validation of LA48 with semiflex ion chamber measured at SSD = 100cm, depth = D_{max}, for a 10x10cm^2 field

The EDW profiles of the wedged direction acquired using EPID calibrated with buildup for flood field acquisition under both, Varian and WBCC method calibration were found to be within 5% with the LA48 ion chamber measurements. Figures 4.12, 4.14, 4.15 and 4.16 show a comparison of profiles acquired with EPID and LA48. These figures show that the profiles acquired using EPID agree within 1% of LA48 profiles in all regions except for the 'hot edge' of the EDW profiles where the discrepancy up to 5% is seen. These results agree well with the results of a previous study [48]. However, for larger field size of 18 x 18cm^2 the agreement at the 'hot edge' of the profile is better than 1.5%. The EDW profiles also exhibit a discrepancy in the penumbra region as seen in open field profiles. Similar discrepancies as in the tail region of open field profiles are also noticed in EDW profiles.

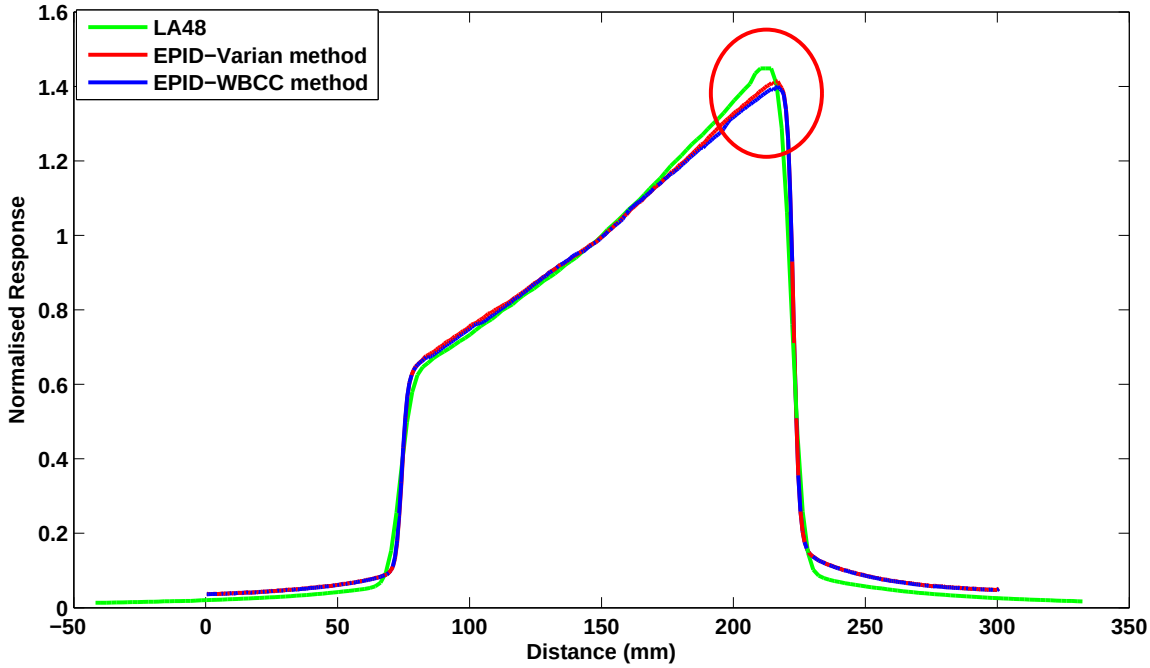

Figure 4.12: Comparison of 10 x 10cm^2 EDW 60° profiles acquired using LA48 & EPID with 6cm buildup for flood field.

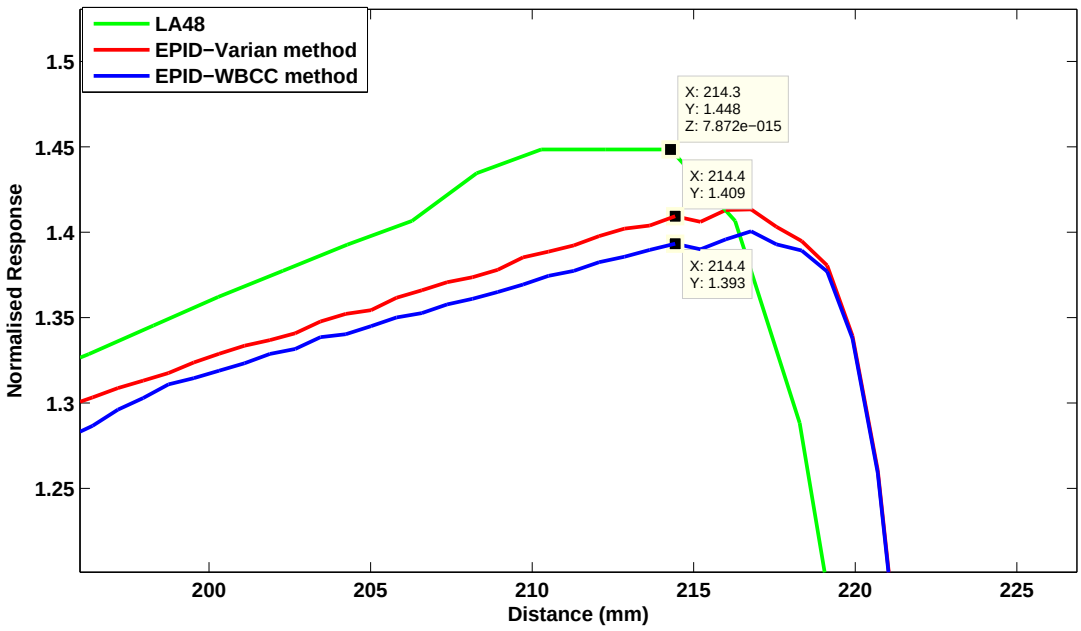

Figure 4.13: Magnified image of the marked region of above profiles.

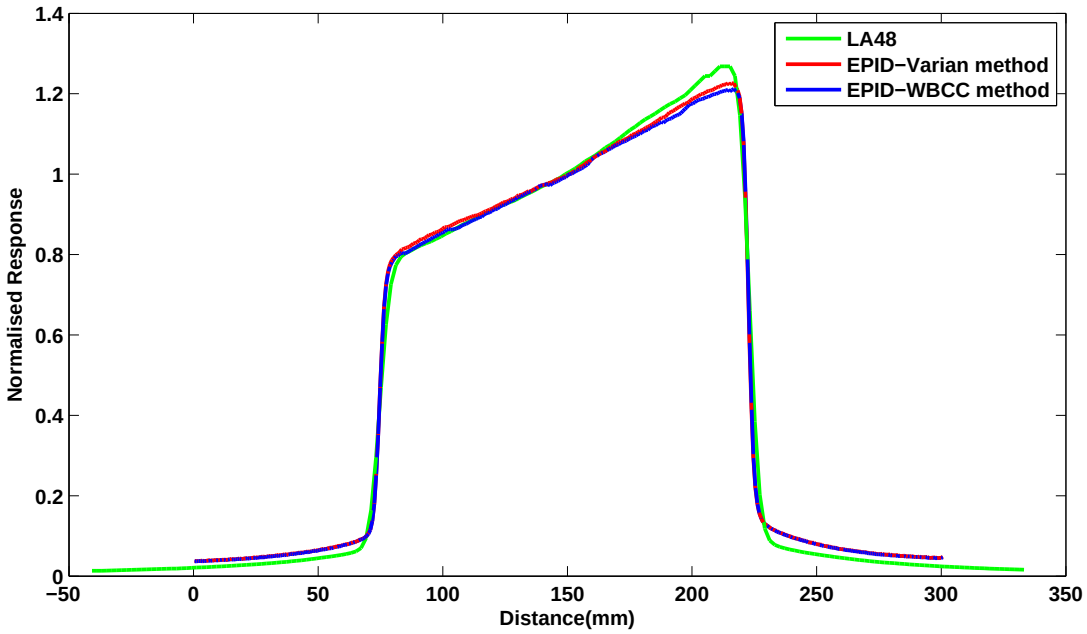

Figure 4.14: Comparison of 10 x 10cm^2 EDW 45° profiles acquired using LA48 & EPID with 6cm buildup for flood field.

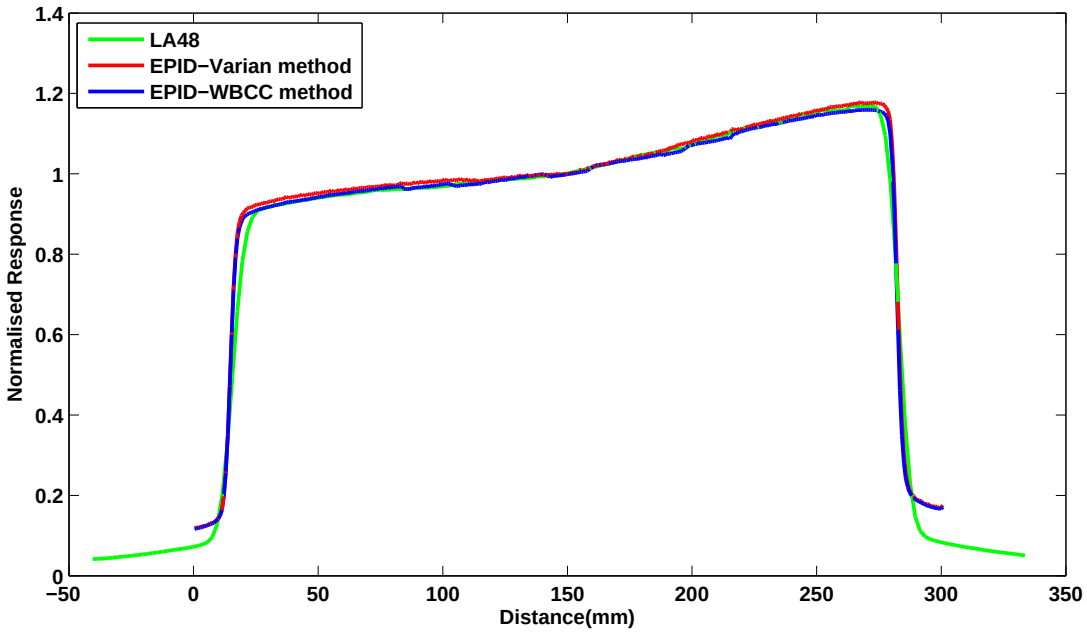

Figure 4.15: Comparison of 18 x 18cm^2 EDW 15° profiles acquired using LA48 & EPID with 6cm buildup for flood field.

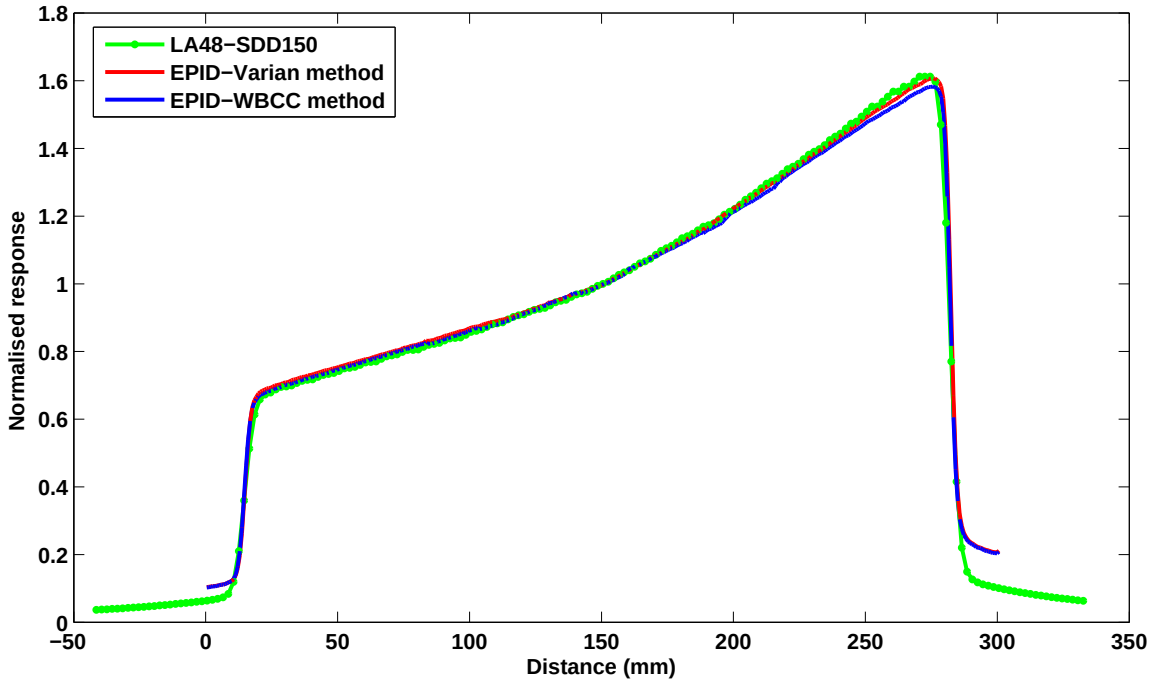

Figure 4.16: Comparison of 18 x 18cm^2 EDW 45° profiles acquired using LA48 & EPID with 6cm buildup for flood field.

The wedged profiles acquired with EPID calibrated under both methods without using any buildup material for flood field differed in agreement with LA48 and exhibited a field size dependence. For field size of 10 x 10cm^2 the profiles obtained with Varian calibration method show better than 2% agreement in comparison to approximately 4% discrepancy seen between EPID profiles calibrated under WBCC method and LA48. For the larger field size of 18 x 18cm^2 the profiles acquired using Varian method of calibration for EPID deviated from LA48 profiles up to 8% at the 'hot edge' or the high dose region of the EDW profile. These profiles also showed considerable distortion. However, the agreement between the profiles acquired using the WBCC method of EPID calibration with LA48 was better than 1.5% for 18 x 18cm^2 even at the 'hot edge'. These results obtained from Figure 4.17, 4.18, 4.19 and 4.20 are tabulated below (Table 4.2) for simplicity.

Also seen from the figures is a change in detector response at the hot edge of the profile. For profiles acquired without using any buildup do not exhibit the discrepancy pronounced at 'hot edge'. Instead the agreement extends to the entire profile.

Table 4.2: Comparison of EDW profiles obtained using LA48 and EPID with two calibration methods

Measurement type	**Varian method**	**WBCC method**
with buildup	5%	5%
without buildup	up to 2% (for 10 x 10cm^2) up to 8% (for 18 x 18cm^2) unacceptable distortion	up to 4% (for 10 x 10cm^2) up to 1.5% (for 18 x 18cm^2) no noticeable distortion

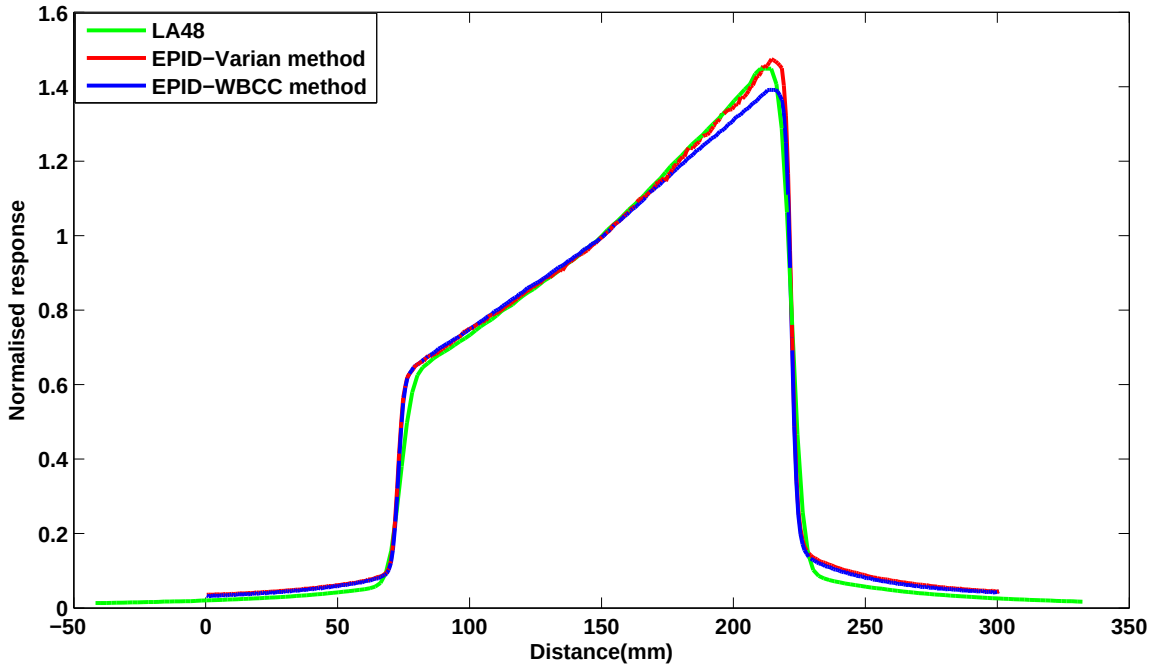

Figure 4.17: Comparison of 10 x 10cm^2 EDW 60° profiles acquired with semiflex & EPID without buildup for flood field.

Similar to the open field profiles, the EDW profiles exhibit a deviation from ion chamber in the tails and the penumbra region. The shorter tails and non-zero initial response are all similar characteristics as seen and discussed for open field profiles.

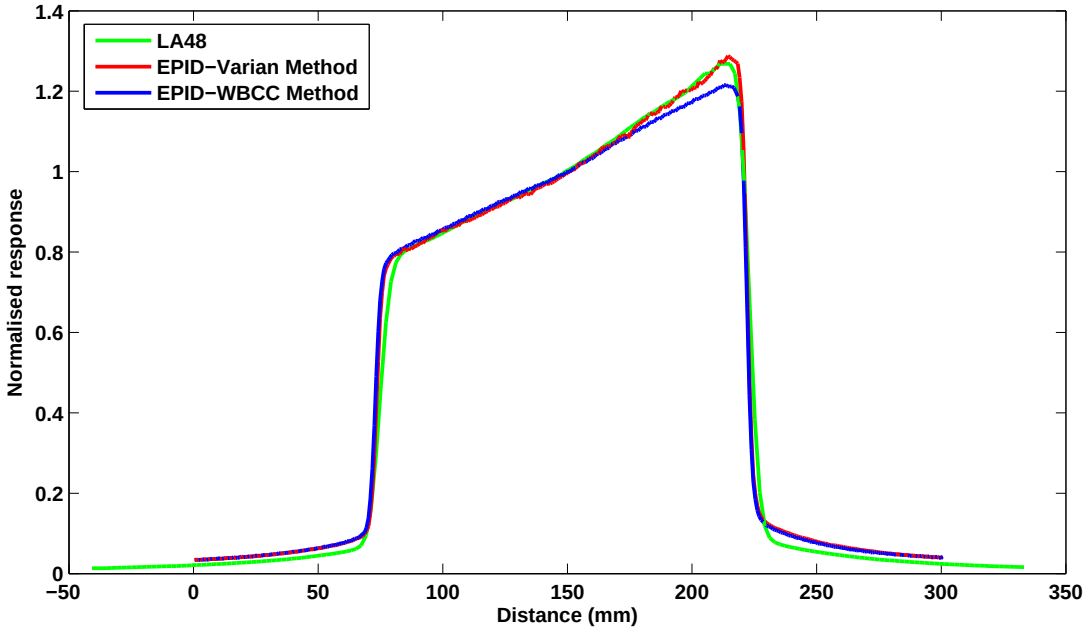

Figure 4.18: Comparison of 10 x 10cm^2 EDW 45° profiles acquired with semiflex & EPID without buildup for flood field.

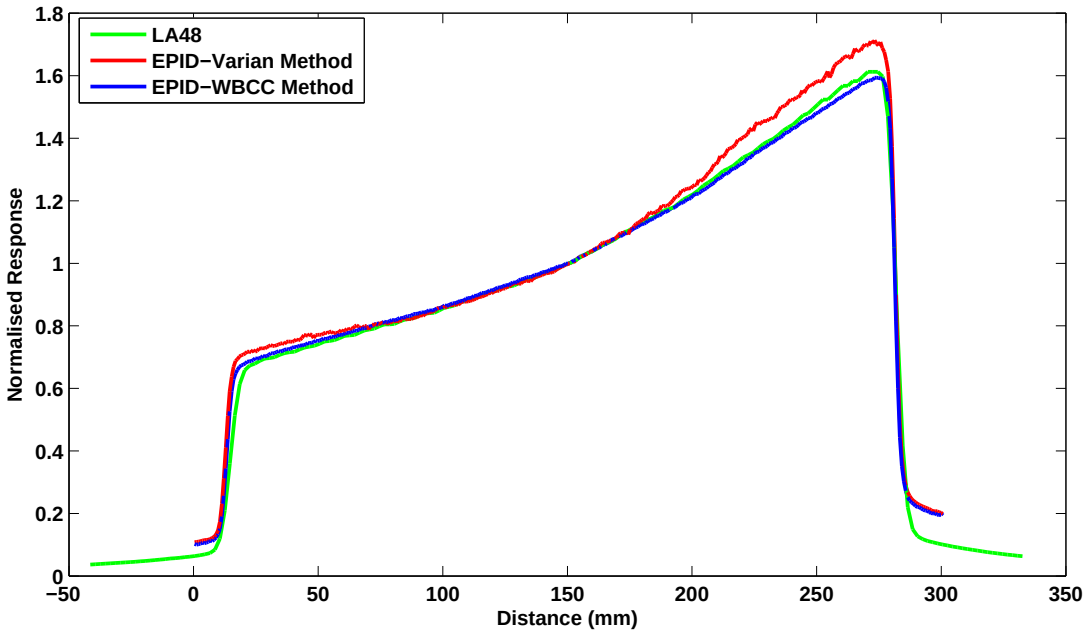

Figure 4.19: Comparison of 18 x 18cm^2 EDW 45° profiles acquired using LA48 & EPID without buildup for flood field.

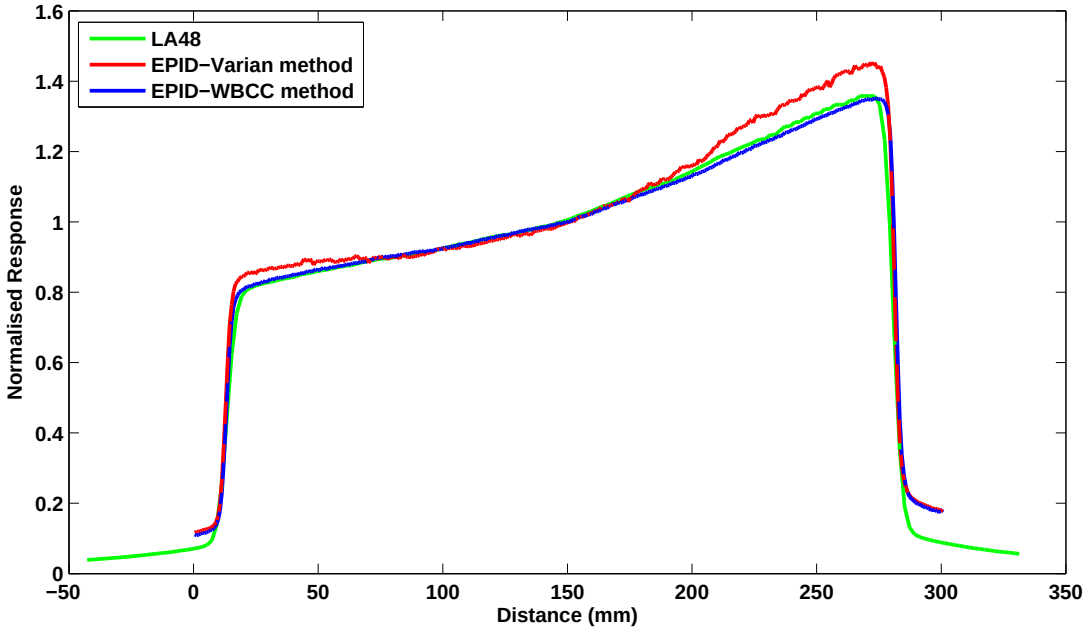

Figure 4.20: Comparison of 18 x 18cm^2 EDW 30° profiles acquired using LA48 & EPID without buildup for flood field.

4.1.6 Asymmetric field profiles

Asymmetry was introduced along the radial axis of the linac with the Y jaws asymmetric about the central axis, keeping the X jaws symmetric. Y1 = 1cm; Y2 = 17cm, X = 18cm. Figure 4.21 and 4.22 show the comparison between open and EDW field profiles acquired using semiflex and LA48 respectively. These profiles are acquired at SDD = 150cm for field size of 18 x 18cm^2.

The profiles acquired using EPID showed huge discrepancies from ion chamber profiles. The EPID open field profiles varied not only in the magnitude of dose but also in the shape of profiles acquired. The EPID acquired profiles under both calibration methods exhibited a difference of upto 16% from open field profiles acquired using semiflex. Though profiles of EDW fields acquired using EPID calibrated under both methods showed a discrepancy of upto 8% and 6mm at the 'hot edge' from profiles acquired using LA48.

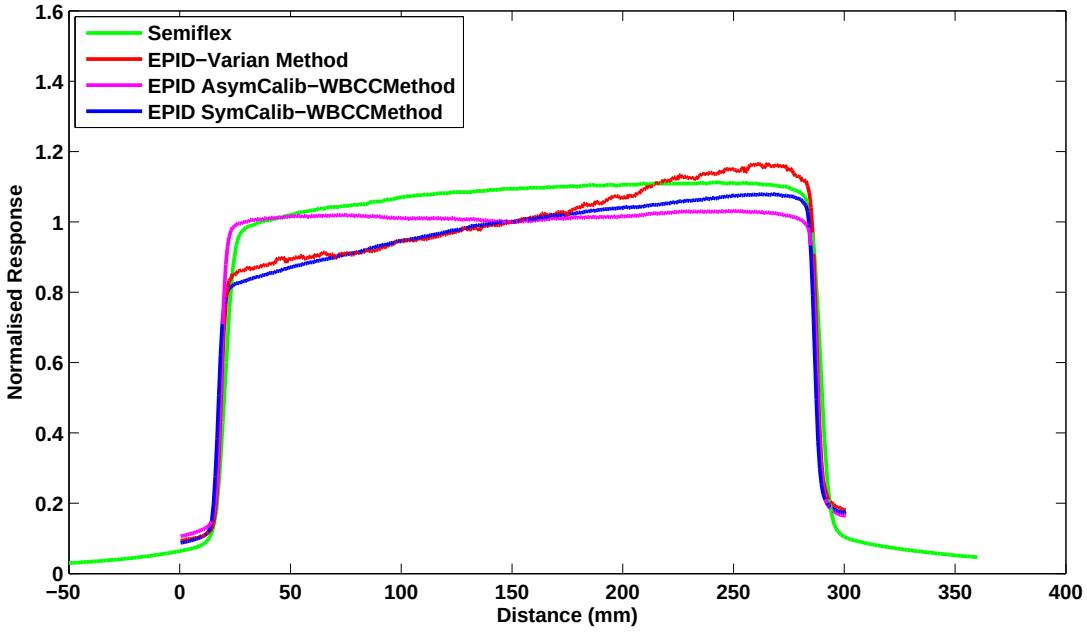

Figure 4.21: Comparison of 18 x 18cm^2 asymmetric open field profiles acquired using semiflex & EPID without buildup for flood field.

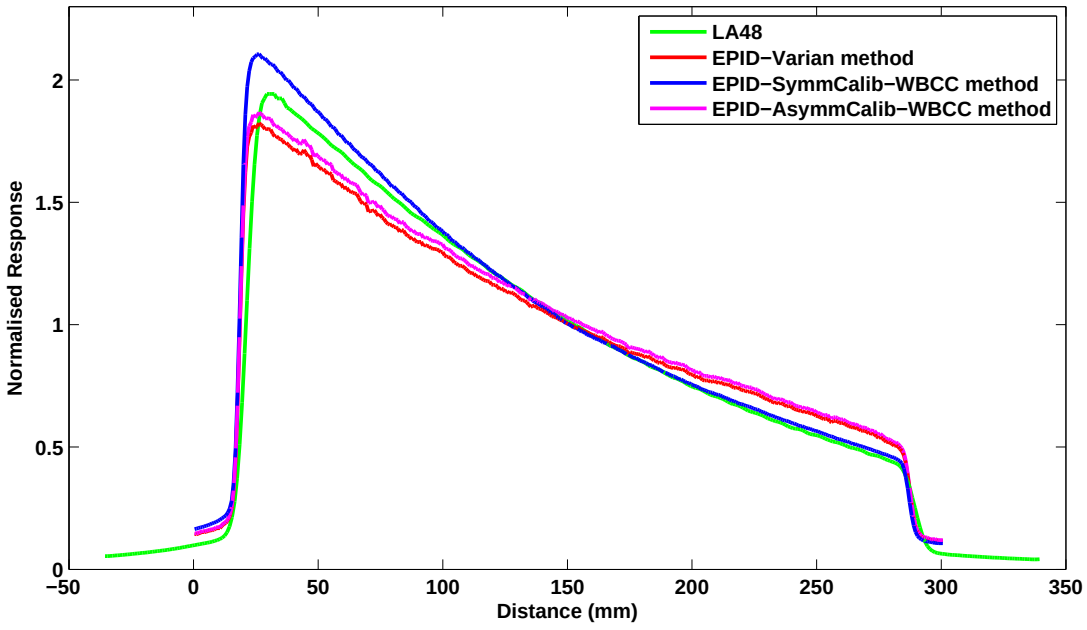

Figure 4.22: Comparison of 18 x 18cm^2 asymmetric EDW 60° field profiles acquired using semiflex & EPID without buildup for flood field.

4.2 Applications for linac QA

4.2.1 Output constancy

The images obtained using EPID were analysed for evaluating the central axis output. These were compared to Keithley tracker measurements. The uncertainty on the readings obtained using the repeatability measurements have been plotted as error bars on the EPID readings. A combined uncertainty of 1% can be assigned to the readings of Keithley tracker as its response is temperature and pressure dependent. Also the day to day variations in set-up adds to the uncertainty apart from the tracker variability of at least 0.5%. These uncertainties have been used for all the further measurements. Figure 4.23 is a comparison of EPID and Keithley tracker measurements showing good agreement within experimental uncertainty.

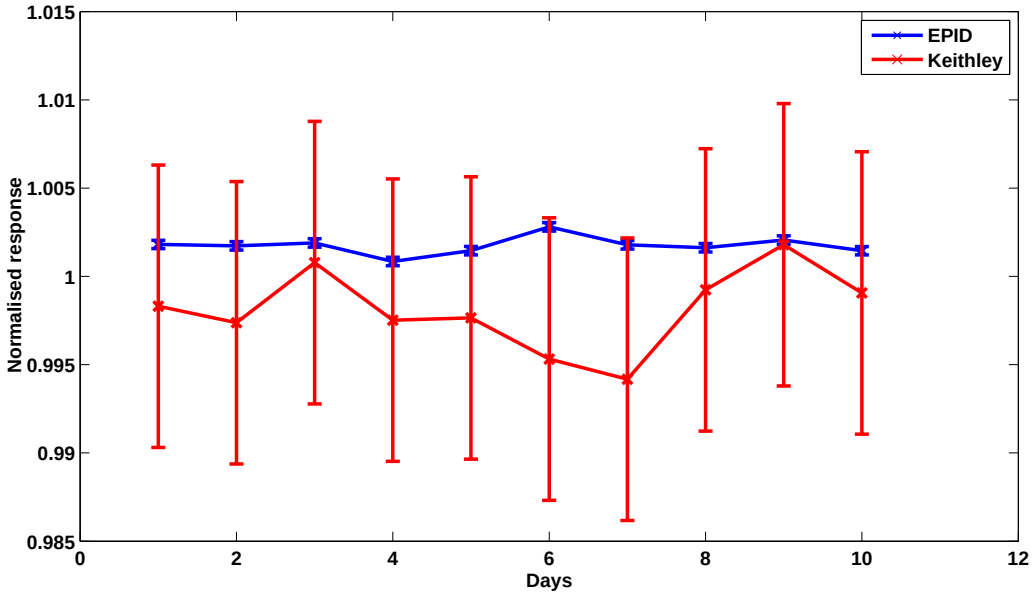

Figure 4.23: Comparison of daily linac output constancy measured using Keithley tracker and EPID

4.2.2 Wedge factor constancy

The EDW factors measured using EPID in this study are are only a measure of constancy. These factors have been calculated from the open and EDW field images acquired at SDD = 150cm for field sizes of 10 x 10cm^2 and 18 x 18cm^2. The EPID measured wedge-factors are given in Table 4.3. These were also found to be within 1% of the theoretically calculated EDW factors illustrated by Gibbons [49].

Table 4.3: Reproducibility of EPID measured EDW factors

	10 x 10cm^2		**18 x 18cm^2**	
	45°	**60°**	**45°**	**60°**
Calculated	**0.773**	**0.665**	**0.600**	**0.468**
EDWF 1	0.780	0.668	0.60	0.473
EDWF 2	0.774	0.670	0.605	0.474
EDWF 3	0.778	0.670	0.607	0.477
EDWF 4	0.777	0.667	0.605	0.474
EDWF 5	0.777	0.670	0.605	0.474
EDWF 6	0.779	0.667	0.607	0.477
EDWF 7	0.776	0.668	0.605	0.475
2 Standard Deviation	0.39%	0.25%	0.2%	0.31%

4.2.3 Wedge angle constancy

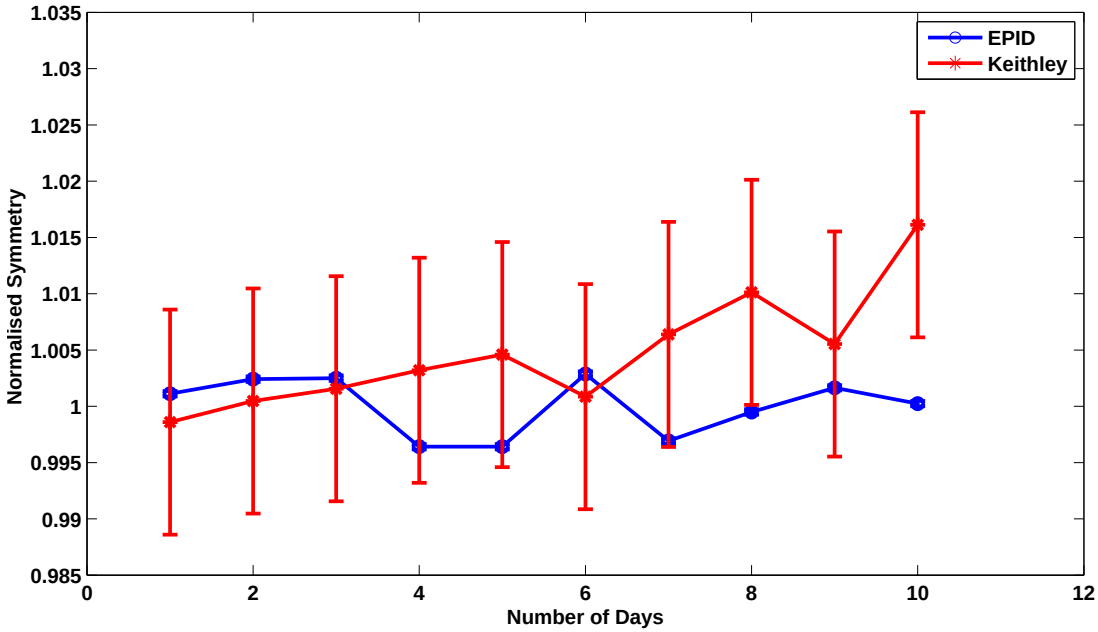

Figure 4.24: Wedge angle constancy verification using Keithley tracker and EPID

The symmetry of the EDW field in the wedged direction was calculated from the acquired profiles. The comparison between Keithley tracker and EPID is shown in Figure 4.24 proving good agreement within experimental uncertainty with one outlier. The

uncertainty of 1% is attributed to the Keithley tracker measurements as explained for output constancy. The uncertainty on the EPID measurements is calculated from the repeatability measurements.

4.2.4 Flatness & Symmetry

The flatness and symmetry have been calculated using the Varian definitions for the profiles acquired using EPID. These are then compared to Keithley tracker measurements of flatness and symmetry constancy. Figure 4.25 shows the EPID measured flatness offset by approximately 1%. Figure 4.26 compares the constancy of the beam symmetry as measured by EPID and tracker also demonstrating an offset of approximately 1%.

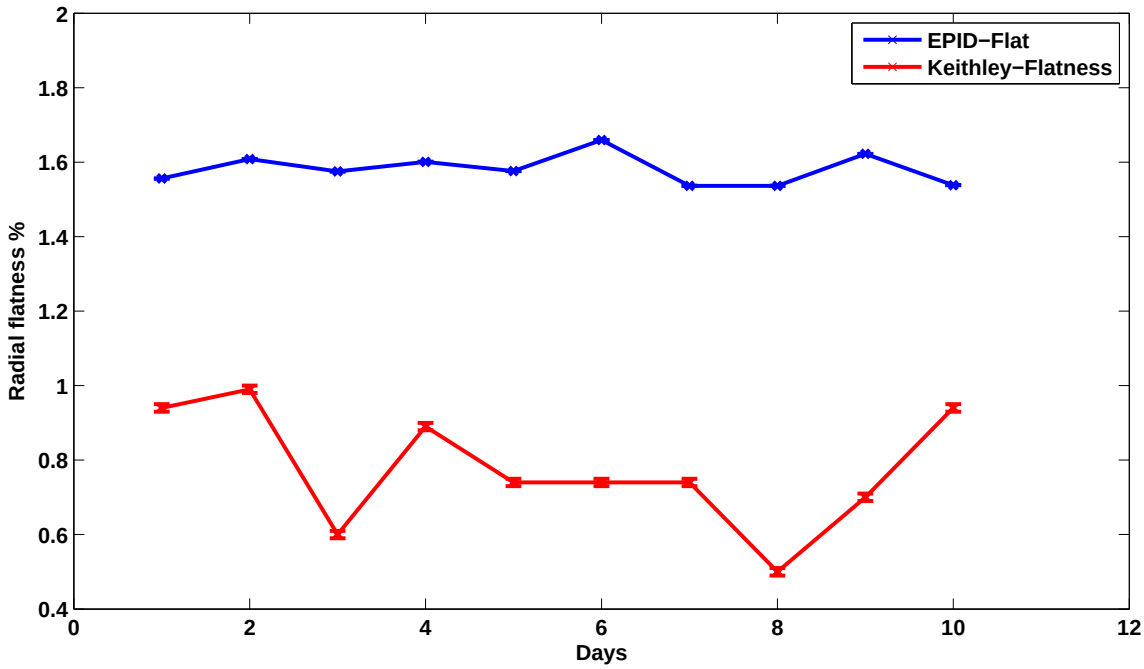

Figure 4.25: Comparison of beam flatness constancy measured using Keithley tracker and EPID

The uncertainty on these measurements were plotted in a similar way to those for output and wedge angle constancy measurements.

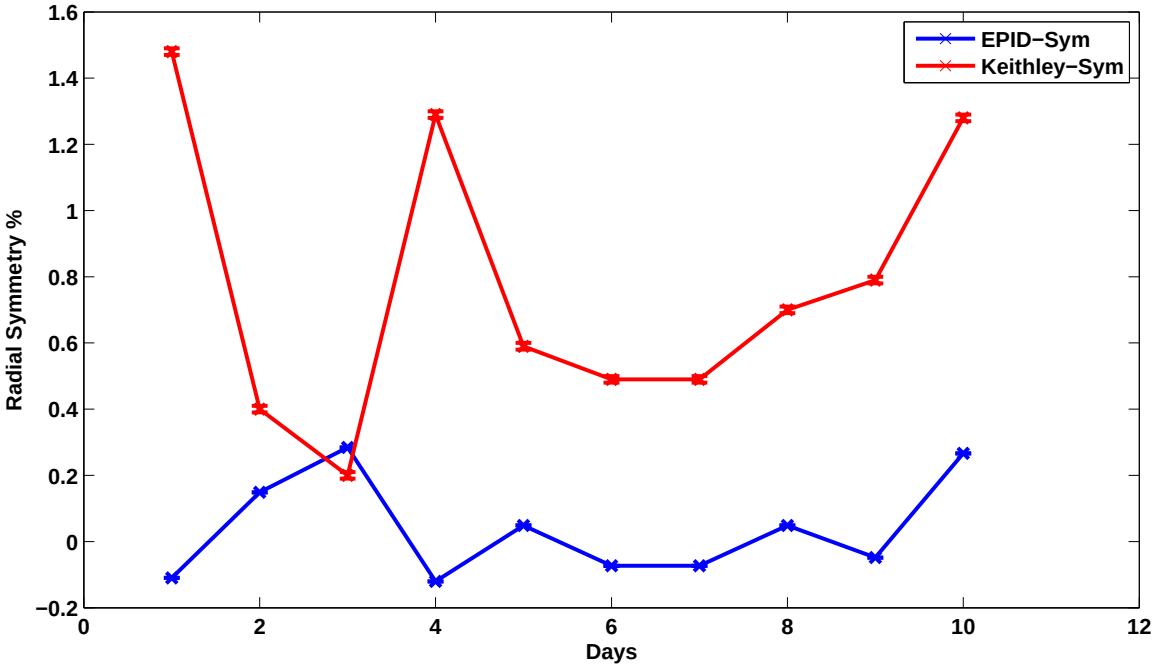

Figure 4.26: Comparison of beam symmetry constancy measured using Keithley tracker and EPID

4.2.5 Coincidence of light field vs radiation field

The 'integrated' and 'after' images acquired using EPID are then analyzed in the review workspace of Vision where various evaluating tools are available. An especially useful feature of the workspace is the edge detection filter which contours the 50% field edge. The 50% edge of the integrated image is automatically contoured on the 'after' image hence enabling us to evaluate the discrepancy between radiation field and light field by measuring the distance between the center of the steel ball and the detected edge. Magnifying the image and using the distance tool helps to accurately measure the distance between the field edge and the centre of the steel ball. The discrepancy between light field and radiation field can therefore be objectively determined using the EPID.

4.2.6 Verification of independent jaw calibration

Images of the gap and overlap of 1cm, 0.4cm, 0.2cm, 0.1cm introduced in the 4 quadrants acquired over a period of a month were analysed. Using the tool to plot dose profile, the co-ordinates of the jaw position were noted. The differences in these co-ordinates give the magnitude of the gap or overlap present between the jaws. These values for the measured

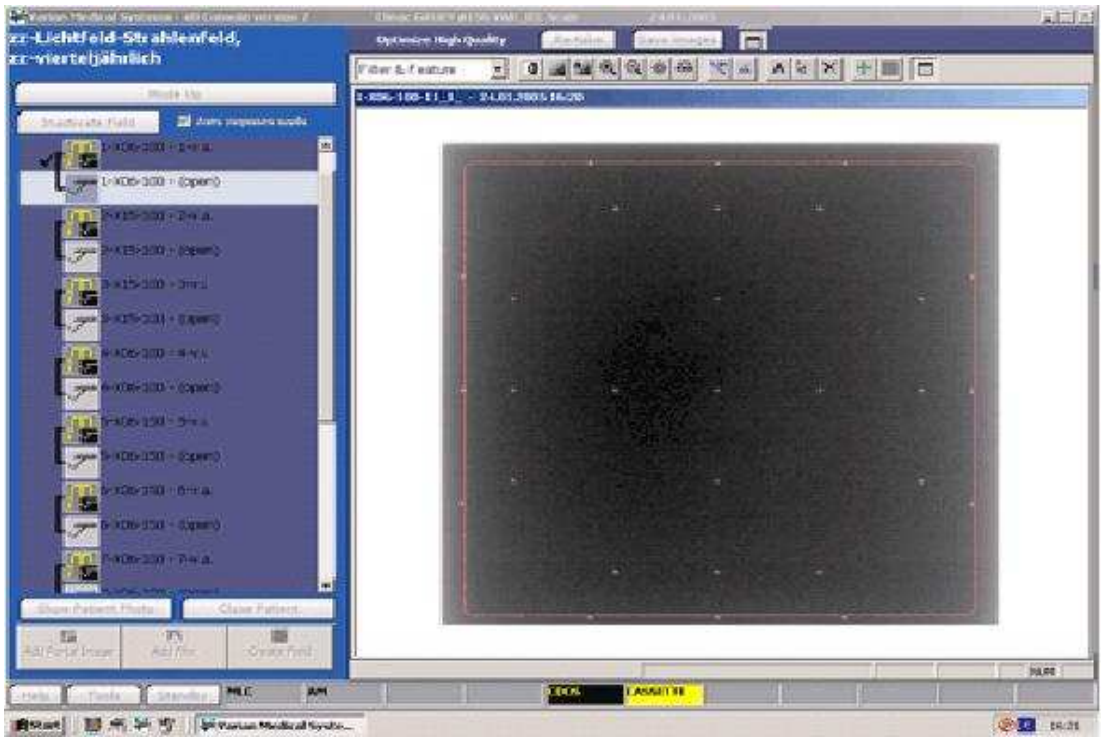

Figure 4.27: 50% edge detected on image for coincidence of light field vs radiation field.

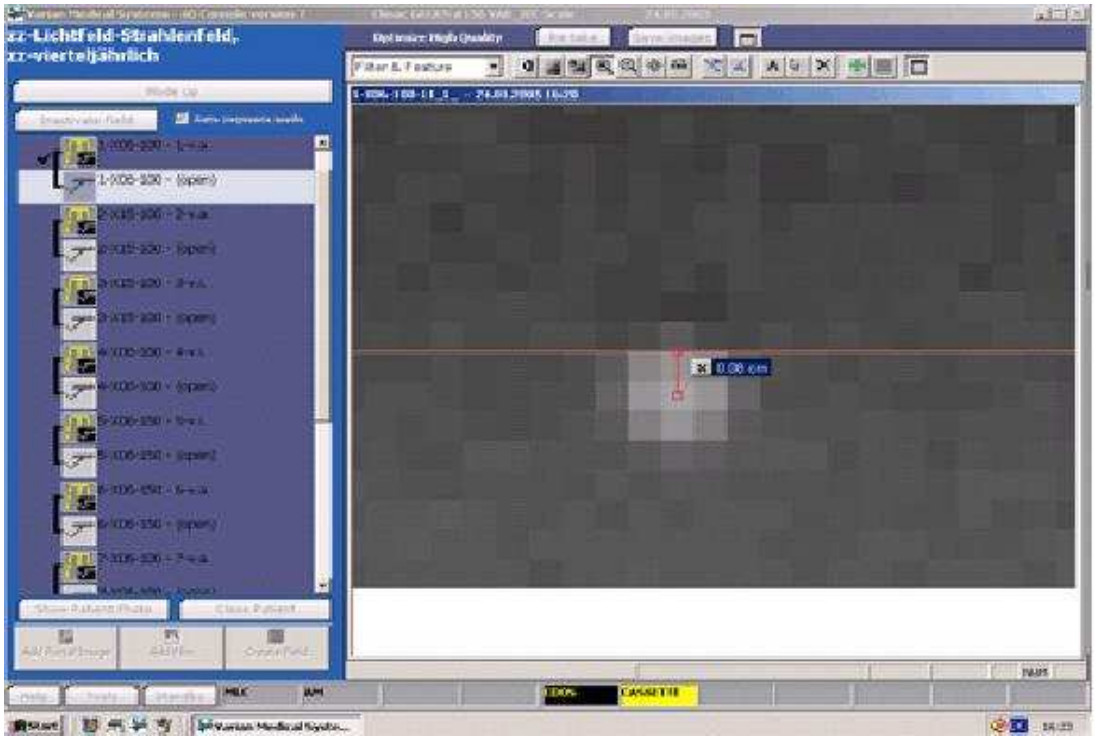

Figure 4.28: Discrepancy measured using the distance tool after magnification for better alignment.

gaps and overlaps of the data were noted and a mean deviation from the set magnitude of gap or overlap was calculated. The standard error was calculated and a student t-test performed for 10 degrees of freedom corresponding to 95% confidence interval. Figures 4.29, 4.30 show the jaw settings or magnitude of gap / overlap introduced between the quadrants plotted against the mean deviation of their respective measurements. The jaw settings for quadrant 1, 2, 3 and 4 are as per Table 3.3

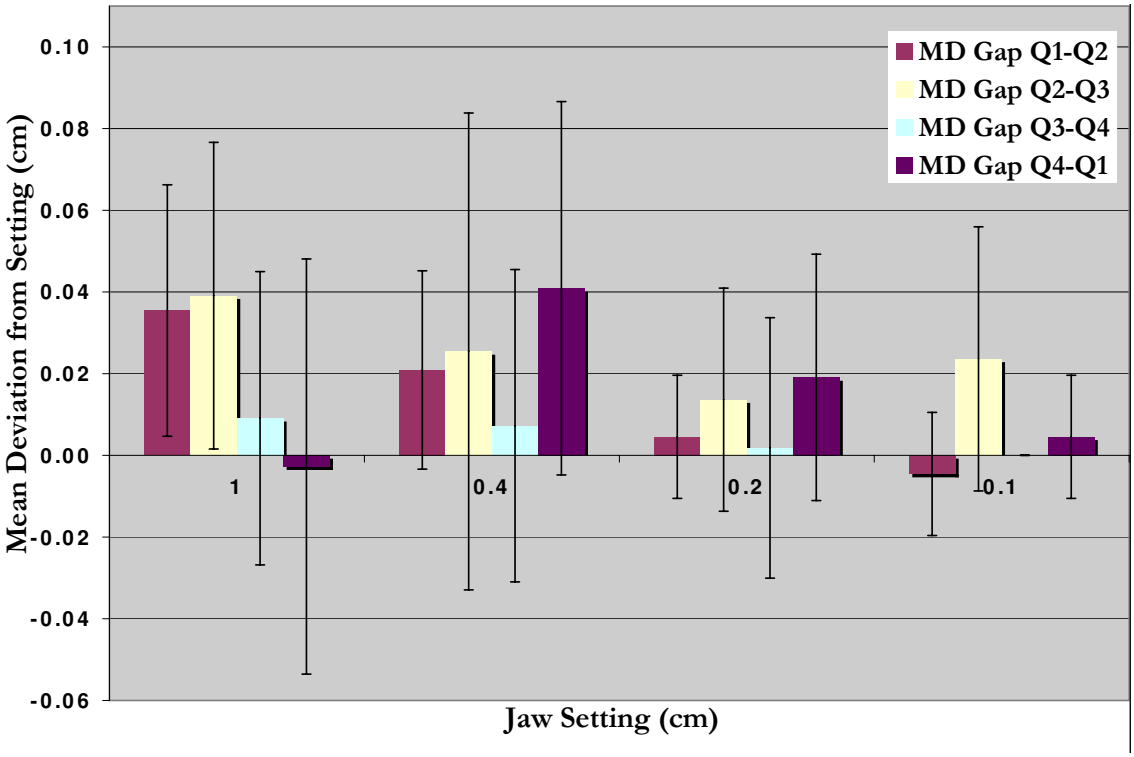

Figure 4.29: Mean deviation of 'gap' measurements

From the graph of gap and overlap measurements (Figures 4.29 and 4.30) of jaw settings against the mean deviation from setting and using standard deviation to plot the error bars, we can state the following:

- No systematic difference between the quadrants was evident.
- Mean differences for the gaps with larger settings (ie 1cm & 0.4cm) tend to be larger.
- Mean differences for the overlaps were independent of the jaw setting.
- Mean differences for the gap tend to be positive (larger than the setting), whereas mean differences for the overlap tend to be negative (smaller than the setting)

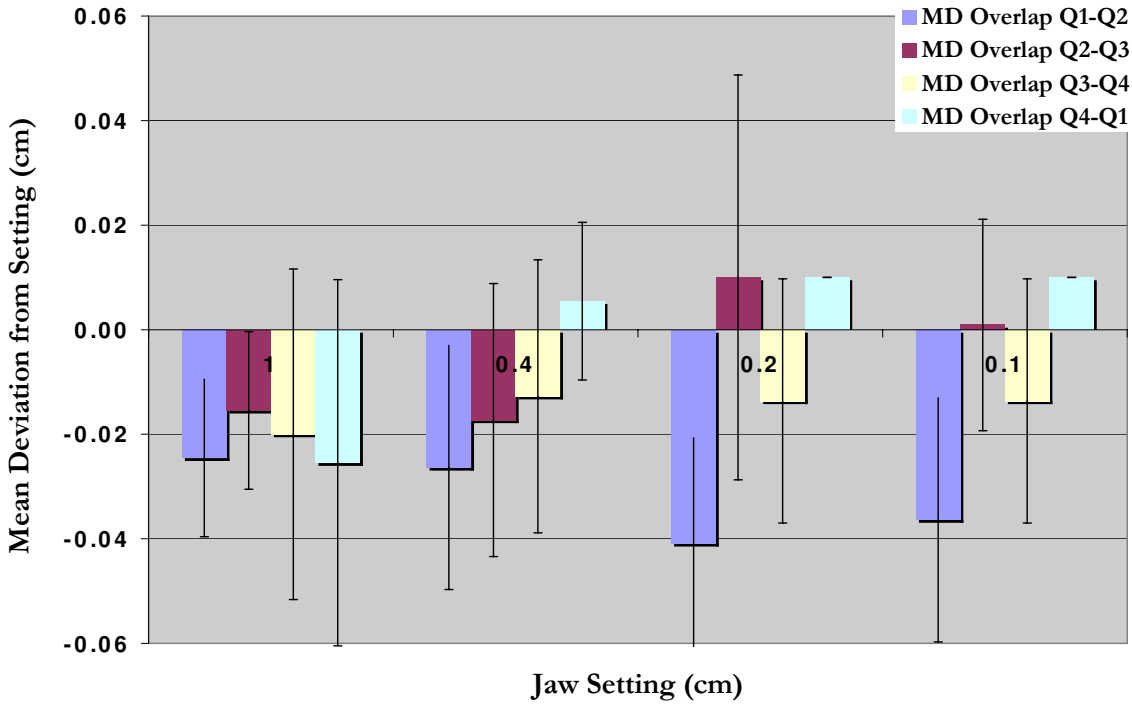

Figure 4.30: Mean deviation of 'overlap' measurements

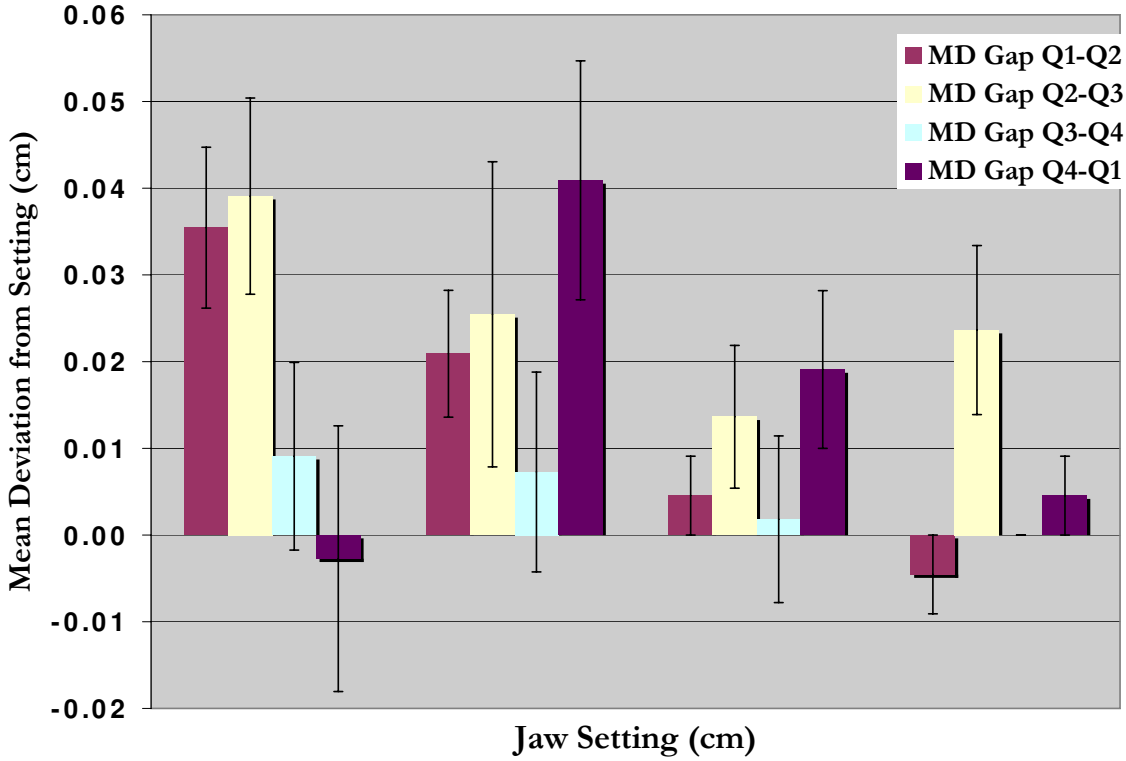

Figure 4.31: Standard error of 'gap' measurements

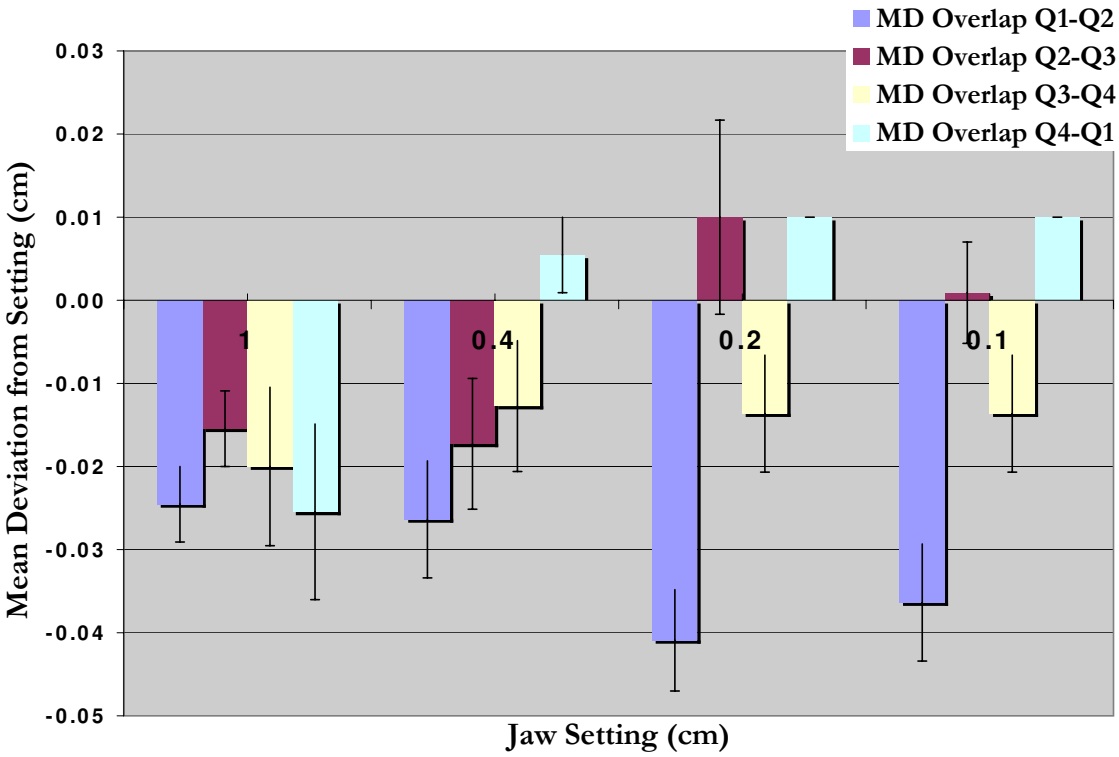

Figure 4.32: Standard error of 'overlap' measurements

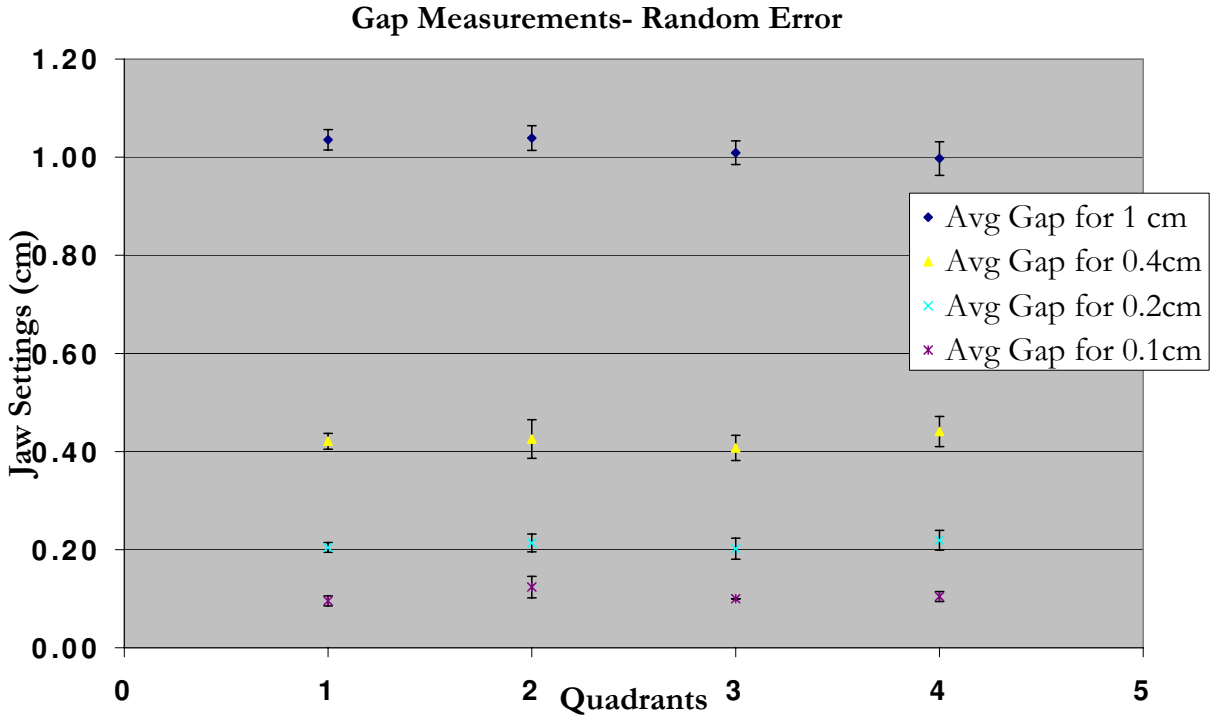

Figure 4.33: Random error of 'gap' measurements

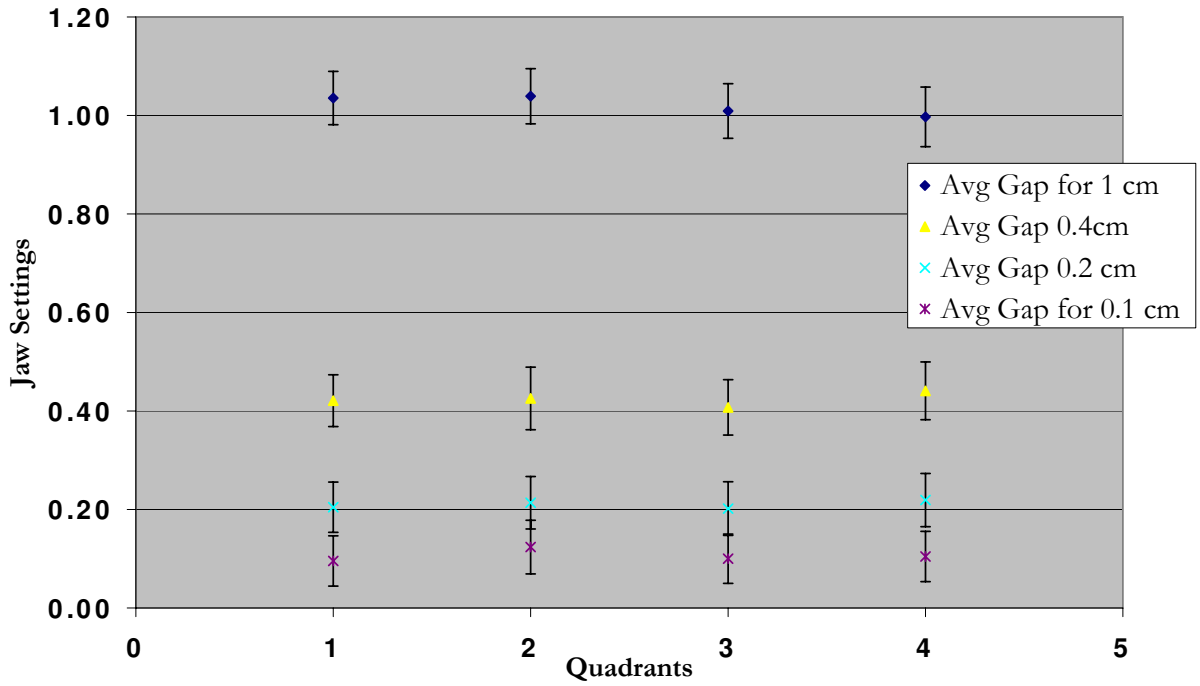

Figure 4.34: Random & systematic error of 'gap' measurements

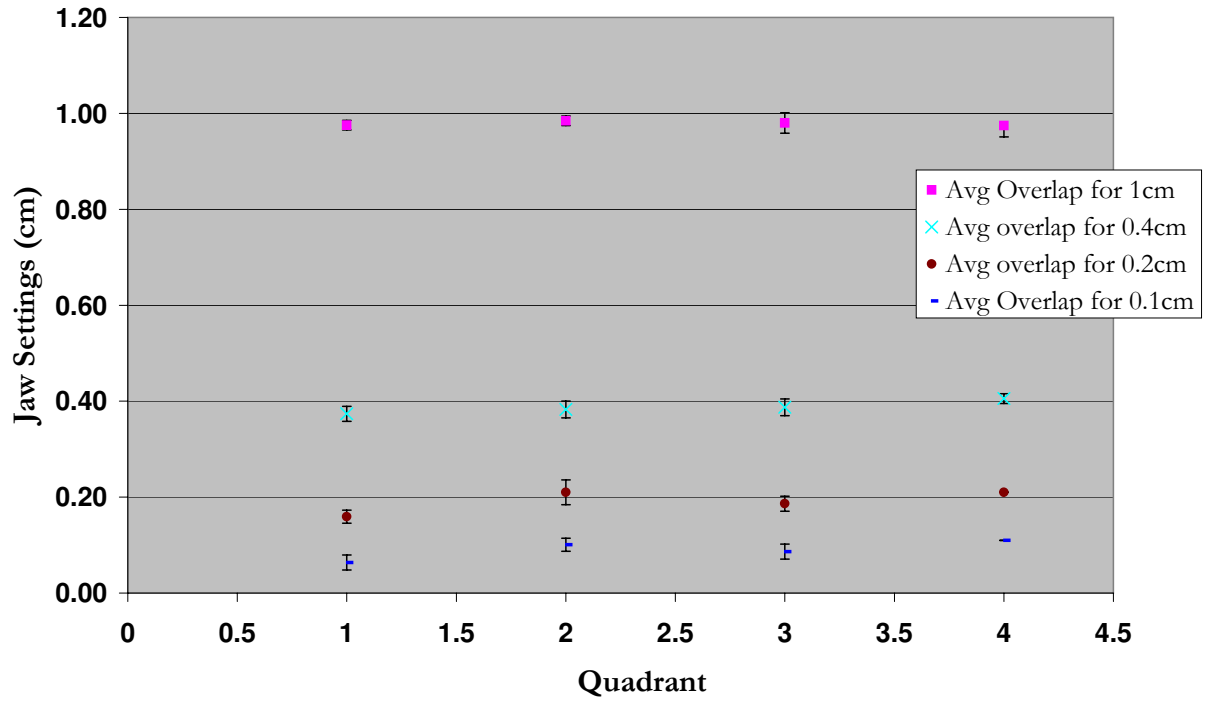

Figure 4.35: Random error of 'overlap' measurements

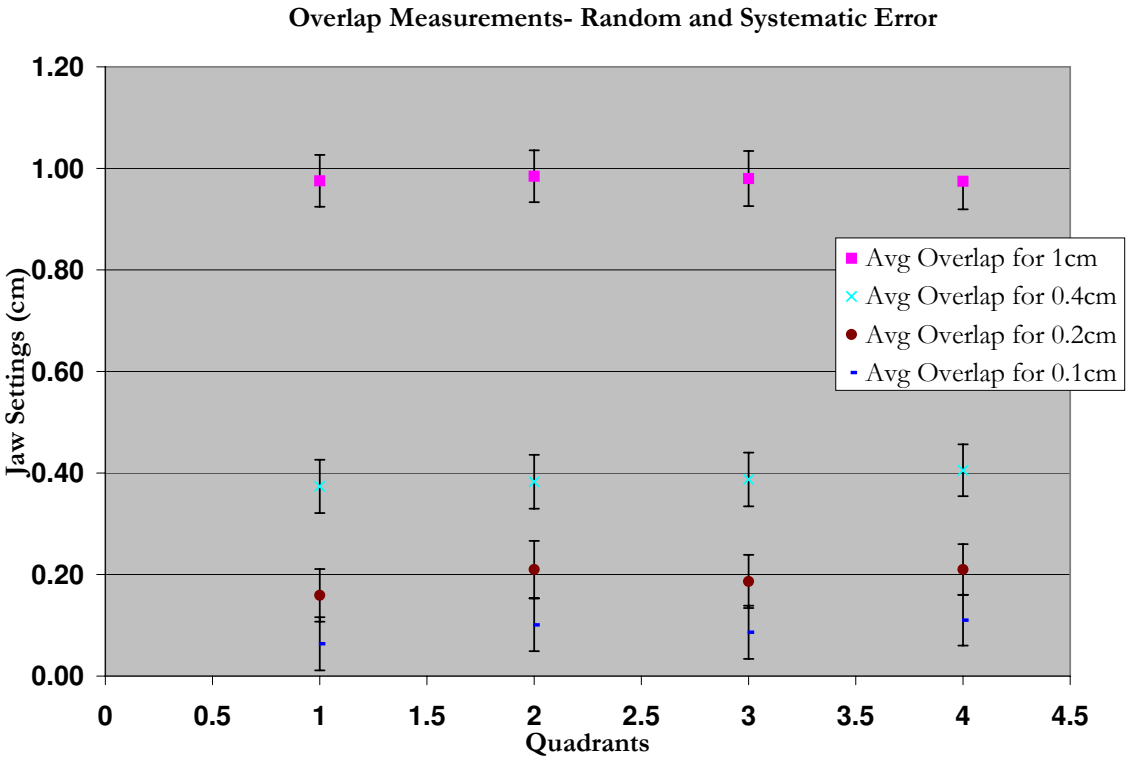

Figure 4.36: Random & systematic error of 'overlap' measurements

All the above statements were confirmed by plotting the standard error of the mean difference against the jaw setting as shown in Figure 4.31 and 4.32. To enable better understanding of the behaviour the student t-test distribution was performed with 10 degrees of freedom and corresponding 95% confidence interval. These uncertainty values were plotted with the average of the data for each quadrant. The results seen above were pronounced by the t-test. A systematic error of 0.25mm on each jaw can be assigned, owing to the measuring device. The systematic error is then added in quadrature with the random error. Random error and systematic error of 'gap' measurements are shown in Figure 4.33 and 4.34 respectively. Similarly 'overlap' measurements are shown in Figure 4.35 and 4.36. On incorporating the systematic and random error the measurements agree to the jaw setting within experimental uncertainty.

4.2.7 Verification of radiation isocentre

Collimator spoke shot

The images acquired using EPID with collimator rotation needs to be combined or added together to enable analysis of the sphere around which the collimator rotates. Vision

allows the combination of images, but converts the image into a grayscale (Figure 4.37) and hence removes the transparency, disabling the ability to view the sphere clearly. Also, plotting the dose profile across it is disabled making it difficult for analysis.

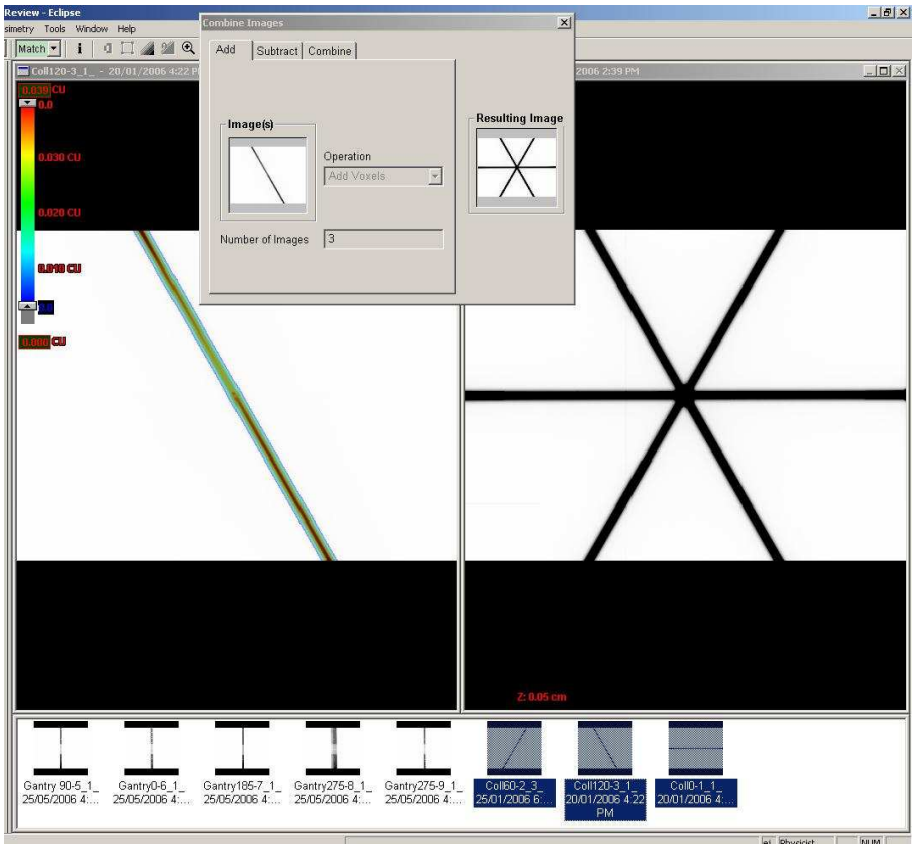

Figure 4.37: Collimator rotation 'added' resultant image.

However, applying filters available in the workspace does enhance the image making the analysis possible. The resultant combined image needs to be scaled for distance. Using the phantom has an advantage of giving an accurate distance between two points on the image. The centre of each image can be found using the measure tool and a line drawn to pass through the centre. This is repeated for image of every collimator angle which forms a triangle in the centre. The length of the longest side of the triangle and correspondingly the diameter of the circle within it can then be measured.This shows that it is feasible to use EPID for Collimator spoke shot test.

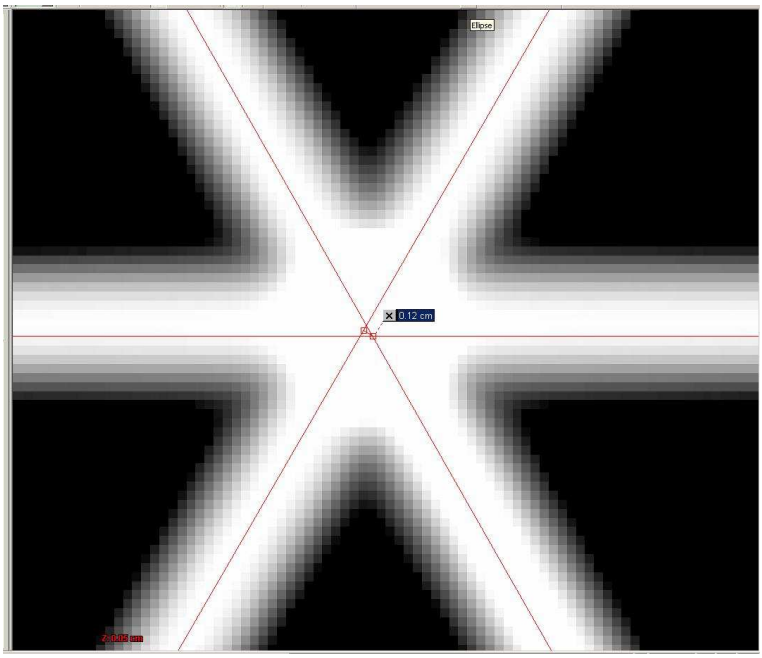

Figure 4.38: Collimator rotation magnified resultant image

Gantry spoke shot

Using a port film graticule and a phantom placed on the couch at SSD=100cm could make the images independent o the EPID sag, by evaluating the relative distance between the image from the port film graticule and that of the phantom on couch.

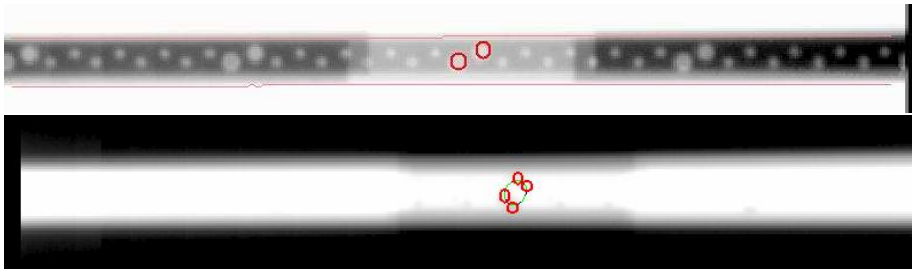

Figure 4.39: Gantry rotation resultant image

This test was not successful due to the diameter of the metal inserts in the port film graticule being bigger than that of the phantom inserts. As it restricts the view of the phantom insert making it difficult to measure the relative distance. But theoretically it seems feasible to find a relative distance between these inserts to eliminating the sag and hence verify the radiation isocentre.

Chapter 5

Discussion

5.1 Dosimetric characteristics

The aSi detector is not water equivalent and thus its response is not linear with dose to water. The measurements obtained using aSi EPID merely displays integrated response of the EPID to the incident fluence. This non-linear response makes it very difficult to get a 1:1 EPID to dose calibration and has a major effect on many of the dosimetric characteristics exhibited by the detector.

The aSi detector is known to saturate at dose rates higher than 300 MU/min. A suggestion for limiting the clinical dose rate to 300 MU/min was made in a previous study [43] to maintain good accuracy of dosimetric data for all SDD's. This is highly restrictive for departments that use 600MU/min as a standard clinical dose rate. The study to evaluate the effect the calibration distance has on dosimetric accuracy proved two ways of eliminating the detector saturation during calibration for the highest dose rate available i.e. 600MU/min. The saturation of the detector can be avoided by reducing the dose incident on the EPID. The dose reaching the EPID can be lowered either by using additional buildup or by increasing the detector distance from the source.

The first calibration method studied here looked at the effects of calibrating with additional buildup for flood field acquisition at short SDD = 105cm and at larger SDD = 150cm. No additional buildup was used for dosimetric calibration or for the measured dosimetric profiles. No saturation effects were noticed in the profiles measured at SDD = 150cm, showing good agreement with ion chamber profiles as shown in Figures 4.7 and 4.8. Though the saturation is avoided by use of buildup in flood field, the additional buildup also modifies the beam profile incident on the EPID. The beam incident on the EPID under calibration conditions after transmitting through the buildup is different from the virtually unchanged energy spectrum used for measurements of dosimetric profiles in this study where no patient or phantom in beam was used. The change of beam spectrum can be attributed to beam hardening caused by the additional buildup in the beam for

calibration. This change in beam spectrum could result in a change in detector response due to a decreased fraction of low-energy photons incident on the EPID during calibration [50]. In addition, a 3mm discrepancy is seen on the 'shoulders' of the profiles acquired with EPID in Figures 4.7 and 4.8, this deviation from the ion chamber profiles can be attributed to the scatter properties of EPID which vary from that of an ion chamber.

The second calibration method studied here was to calibrate the detector without using buildup at short SDD = 105cm and at larger SDD = 150cm. On calibrating the EPID at shorter SDD of 105cm without using buildup showed a discrepancy of upto 8% on the outer edges of the beam profile with respect to ion chamber profiles as seen in Figures 4.9 and 4.10. But the WBCC method of calibrating at SDD = 150cm showed excellent agreement with ion chamber over the entire profile, without exhibiting any noticeable saturation effects. Since there is no attenuating material in the beam used either for dosimetric measurement or for calibration, the detector response is not altered. This method of calibration at larger SDD = 150cm would therefore seem to be preferable when there is no phantom or patient in beam as is the case for pre-treatment IMRT field verification.

The EPID is also known to over respond to low energy photons such as scatter from the beam defining system, this is demonstrated in the penumbral tails of the profiles showing a deviation from ion chamber profiles of Figures 4.7, 4.8, 4.9 and 4.10. The penumbra region in the profiles also show some discrepancy which can be explained by the low resolution of ion chamber. The shorter tails of EPID profiles for larger field size (18 x 18cm^2) as compared to ion chamber is due to the detector size. Since these are radial profiles, the detector is not big enough to encompass the trailing edge of the larger fields which are further magnified at larger SDD's. This would not be of any dosimetric concern for field sizes smaller than 18x18cm^2 measured at SDD=150cm.

The behaviour of EPID under varying accelerator dose rate was investigated. Since accelerator dose rate is varied dynamically during an EDW delivery this study was performed by comparing EDW profiles acquired using EPID and ion chamber. Inconsistency in EDW profile agreement between EPID and ion chamber was found. Factors affecting these profiles potentially include accelerator dose rate, calibration method, wedge angle, field size, scatter properties of EPID. Since previous studies [42] have proved that the calibration and synchronisation of the EPID at a fixed accelerator dose rate does not limit the accuracy of the EPID when the accelerator dose rate is varied, the effect due to accelerator dose rate can be ruled out. From the study of open field profiles we know that calibrating

the detector without buildup at short SDD's distorts the profiles due to saturation. Therefore the EDW profiles acquired when EPID was calibrated without buildup at short SDD were not included in our analysis ruling out the saturation effects. Since the discrepancy was seen for all wedge angles, it can be concluded to be independent of the wedge angles. The scatter properties of the EPID not equivalent to water could be one possible cause. The discrepancy seen on the 'shoulders' of the open field profiles, could be translated to the 'hot edge' due to the high dose gradient. However, the dependence on field size or the effect due to the calibration method cannot be ruled out, as there seems to be a trend of better agreement with the larger field sizes. But this dependence on field size cannot be conclusively attributed to any known detector characteristic without further investigation.

The asymmetric field profiles acquired using EPID vary in shape and magnitude from the ion chamber profiles as shown in Figures 4.21 and 4.22. The discrepancy in asymmetric field profiles is complicated and a result of the detector displacement to encompass the entire field. Calibrating the EPID under asymmetric conditions to mirror the measurement set-up proved to be of little advantage. Theoretically, calibrating the EPID at the measurement position should give a relatively flat EPID profile, then the diagonal profile correction should put the beam profile back in. However, on doing so, the diagonal profile adds the beam profile back in, but it centers the profile at the EPID centre instead of the central axis of the beam and hence gives a symmetric profile for an asymmetric field. Further investigation is required to study small asymmetric fields which do not require the detector to be moved from the central axis position.

On calibrating the EPID using a symmetric open field without displacing the detector, the beam shape is maintained but there are huge discrepancies in magnitude of dose. These discrepancies are due to the difference in pixel sensitivities of individual pixels and off-axis energy response. As the flood field and the EPID dosimetric image contains the beam profile information, a displacement of the detector position between the flood field and dosimetric image acquisition causes a misalignment of these for FF division. In addition, there is also misalignment of the off-axis differential energy response. The off-axis differential energy response is dependant on the distance of the pixel from the central axis. Consequently, a displacement of EPID by every cm is shown to cause 1-2% errors in profiles by Greer et al [51]. They resolved this issue by correcting the pixel sensitivity variation and off axis differential energy response while retaining the beam profile information. The results presented in the study showed that their method makes the detector response virtually independent of the EPID position. Although the study shows

good agreement with the ion chamber profiles independent of the EPID position, the displacement of the EPID has only been studied in the lateral direction. The longitudinal displacement could produce different results due to the presence of the support arm. As another study [52] showed that the backscatter from the components of the EPID support arm downstream from the detector influences the signal to the detector by up to 5%. The effect of backscatter on the these off-axis energy response and pixel sensitivity corrections remains to be verified.

5.2 Applications for linac QA

The variability on the linacs central axis output measurements acquired using an EPID is small relative to the Keithley tracker with two standard deviations (95% confidence interval) of 0.1% and 0.5% respectively. The Keithley tracker has a strong dependence on environmental conditions such as temperature and pressure. In addition to these, the day to day variation in set-up conditions makes the Keithley tracker highly variable. Use of EPID can eliminate many of these set-up errors since little or no set-up is required for measurements with EPID. Its independence from pressure and temperature is advantageous in verifying the constancy of the linac on a daily basis.

The EDW factors measured using EPID for 7 consecutive days show good constancy. These also agree within 1% to the calculated EDW factors, which is a surprising result. The EDW factors are measured at the reference depth. But the images for this study have been acquired at extended SSD and the inherent depth of the EPID which is approximately 8mm water equivalent. Due to the strong dependence of EDW factors on the field size at depth, they were expected to differ from the theoretical value. However, studies [53, 54] have shown that the EDW central axis depth doses and buildup doses differ only marginally from open field depth doses, suggesting that the effective EDW factors are independent of depth. The factor is a ratio of open field and wedged field, hence cancelling out any effects from extended SSD. This explains the agreement within 1% of the calculated factors. Thus it can be concluded that the EPID is capable of measuring the wedge factors accurately and also shows good constancy. It demonstrates feasibility and reproducibility of the factors over a week, which is comparable to ion chamber measurements as demonstrated in a previous study [48].

The wedge angle constancy verification based on the ratio of two equidistant points

from central axis of the EDW profile obtained using EPID agrees to the Keithley tracker within experimental uncertainty. With the use of EPID it is possible to verify the wedge angle accurately as the EPID acquires the entire profile. Although an algorithm needs to be developed to facilitate this effectively.

The flatness and symmetry of the linac beam needs to be verified on a daily basis. Current practice uses Keithley tracker for measuring output at 5 positions including the central axis and determines the constancy of flatness and symmetry based on those 5 positions. This method looks at the ratio of outputs at two equidistant points, making it prone to set-up variations. Since the fixed detector position on the Keithley tracker samples the beam profile incident only on those points and does not evaluate the entire profile it is highly dependent on the beam position incident on the detector. The EPID on the other hand has the ability to acquire the entire beam profile to evaluate the flatness and symmetry. This difference, in addition to the variability of the Keithley tracker could account for the offset seen between Keithley tracker and EPID. EPID is also independent of the set-up errors and environmental conditions, making it a very easy and efficient tool for daily QA.

EPID is also a very useful tool in performing routine optical tests performed on linac as a film replacement. Quantification of discrepancy between radiation field and light field is simplified by the detected edge, removing the subjectivity introduced by the human eye in conventional film based methods. We could potentially look at inserting steel balls/wires of 0.5mm thickness for better accuracy. Also, maximum resolution of EPID can be obtained by using the EPID at SSD = 180cm. Measurements in this study were performed and evaluated in Vision. The pixel values are re-scaled to distance in 'Review' workspace and many useful analysing tools are available.

The study to verify the calibration of independent jaws showed a positive difference for gaps and negative for overlap. The difference could be a reflection of the test method used but cannot be conclusively explained. There also appeared to be a bias in the measurements showing random uncertainty. As having plotted the error bars, they did not agree within experimental uncertainty to the set positions. A systematic bias could be introduced in calibration of the independent jaws. As the jaw settings are only as good as the calibration of the jaws, to which a systematic uncertainty of approximately 0.05cm (0.025cm on each jaw) can be attributed owing to the measuring device (a ruler) used for the calibrations. Other factors that could contribute to the uncertainty also include the

person's ability for calibration, jaw resolution in terms of engineering specifications and the uncertainty on position readouts (PRO). In addition, as the edge detection algorithm detects the 50% line based on the dosimetric data, the algorithm could also be a source of systematic uncertainty.

The EPID is a feasible tool for use in collimator spoke shot test to verify the radiation isocentre of the linac. This test verifies that the collimator rotates about a sphere of 1mm radius. Although the test is feasible it cannot be accurately evaluated with the present analytical tools available in Vision. It limits the number of images for merging, or 'blending' to only two. Whereas the collimator spoke shot test requires images to be acquired for at least 5 different collimator angles and merged together. Improving the analysis tools to incorporate merging of more than two images and plotting of the dose profile on the resultant image would be beneficial. Improved tools to analyse these images will eliminate the need for any external software to be used.

Theoretically, verifying the radiation isocentre with gantry rotation using EPID seems feasible. However it could not be performed experimentally due to the port film graticule center being larger than the steel ball inserted in the phantom not allowing the phantom ball to be viewed. However, this test would have the same obstacles with analysis as the collimator spoke shot. Thus, although the EPID is proven to be useful and feasible, the tests could be simplified to a great extent by making some minor changes in the Review workspace.

Chapter 6

Conclusion

In this thesis some dosimetric characteristics of the aSi detector aS500 and some of its potential applications for linac QA have been studied.

The study on effect of calibration distance demonstrated that calibrating the detector at distances more typical of the measurement position (SDD = 150cm) avoids detector saturation for the highest dose rate available i.e 600MU/min improving the dosimetric accuracy. Although, the detector saturation can be avoided with the use of buildup for flood field acquisition, this is not the preferred way due to the change in detector response in absence of a phantom in beam. Therefore, calibrating the detector without additional buildup at larger SDD's like 150cm is suggested for accurate dosimetry using dose rates higher than 300MU/min, when an unattenuated beam is measured.

The study of EPID's ability to acquire EDW profiles showed that the detector exhibits a field size dependence, but seems to be independent of the wedge angles. Further investigation of field size dependence is required to understand the optimal calibration for accurate dosimetry. Also, the discrepancy on the 'hot edge' of the profiles needs further investigation.

Currently, the portal dosimetry system is not equipped for use at any position other than the central axis. The investigation of asymmetric field profiles demonstrated that the displacement of the detector from the calibrated position on the central axis causes discrepancies. This is a limitation for measurements at any non central positions. The pixel sensitivity and off axis energy response corrections are shown to make the detector independent of the position [51]. Therefore the corrections for pixel sensitivity and off axis energy response needs to be incorporated in the portal dosimetry system available commercially for ease of use and improved dosimetric accuracy at all detector positions.

The excellent short term repeatability, linearity of the detector, and reproducibility make EPID an attractive option for daily linac QA. The EPID's capability to give constant

output, flatness, symmetry, wedge angle and wedge factors with high level of accuracy and reproducibility is demonstrated. In addition to these capabilities, it is extremely easy to use, does not require any set-up and hence eliminates set-up errors. EPID is also independent of environmental conditions. However, this could be simplified further with better software tools to analyse EPID measurements. One way of simplifying analysis would be to develop an integration environment between the EPID and a QA analysing software like Argus. This will automate the calculation process increasing efficiency and reducing the QA time considerably.

Apart from QA of beam properties, EPID is also capable of performing optical and mechanical QA of linac. The ability of EPID to give high resolution images for minimal dose, in real time makes it an attractive option for optical QA of linac in an environment where use of film and wet processing is being rapidly phased out. As clinical imaging moves away from use of films the need to reduce film dependence for linac QA intensifies. The work here shows the feasibility of EPID in verifying the coincidence of light field and radiation field, verifying the calibration of independent jaws and radiation isocentre objectively, with ease and efficiency. The limitations in performing these tests lies in the ability of the software applications to perform the analysis. The application has some very useful analytical tools to enable most analysis. However, it limits the number of images for merging, or 'blending' to only two. Improving the analysis tools to incorporate merging of more than two images would be beneficial. Also, enabling the saving of the resultant image would help in many aspects such as reducing dependence on port films in clinical settings. Presently, the dose profiles in Vision can only be plotted for the 'dosimetric' image. If the tool can be enabled for plotting profiles across the merged resultant images, that would simplify all the optical QA analysis considerably. Although there are softwares available that analytically verify all the above tests, efforts in this project were to simplify the current practices by restricting the number of softwares used for analysis in a radiation therapy department.

To summarise, better understanding of the dosimetric characteristics of the EPID mainly due to its water non-equivalence is required. Recognising the limitations of EPID caused due to its dosimetric characteristics and effective resolutions to work around the limitations is vital. The portal dosimetry system still has some challenges to resolve in order to perform accurate dosimetry using EPID. Future work requires improved calibration methods to be incorporated, algorithms for dosimetric verification to be developed and some resolved dosimetric issues to be implemented in the commercially available system.

Better software analysis tools would be highly beneficial in its routine use.

Appendix A

Image Orientation

Image Orientation on the screen in respect to the treatment unit is shown in Fig A.1 below.[34]

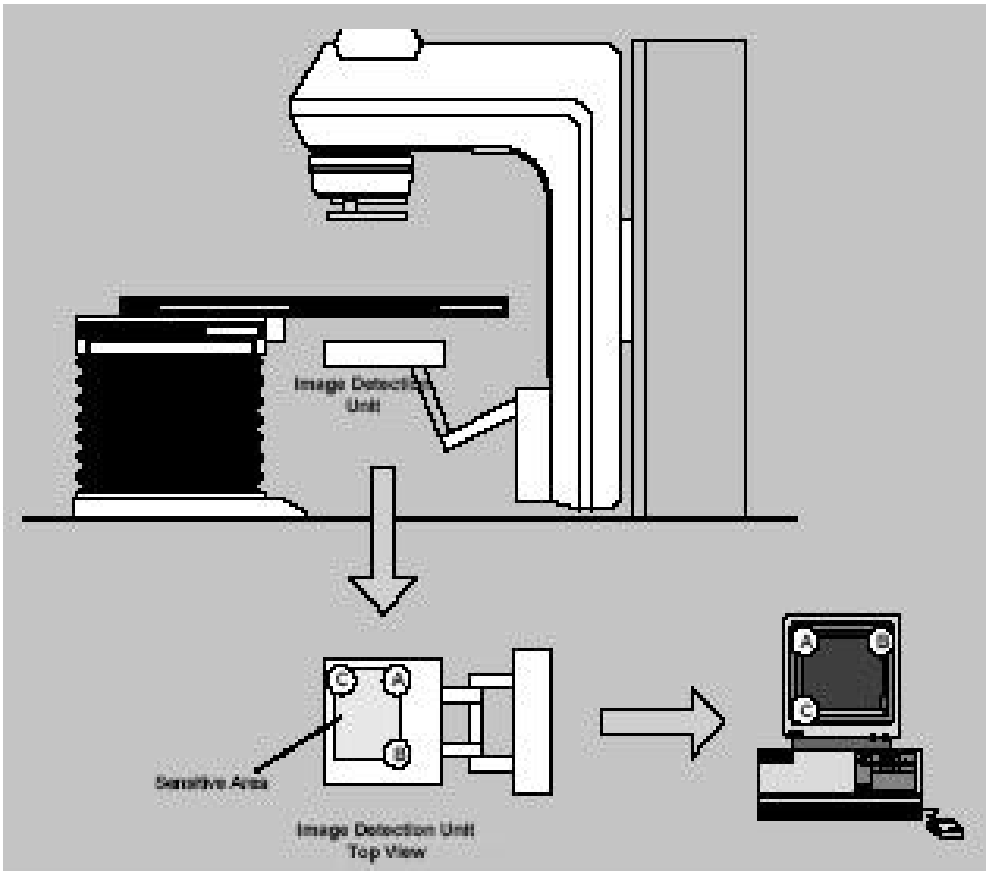

Figure A.1: Image orientation

Image co-ordinates according to Fig A.1 are

Co-ordinate	Row	Column
A	1	1
B	1	512
C	384	1

Appendix B

Clinac Modifications

To enable image acquisition during the dynamic phase of an EDW treatment we needed to make the following modification to the Clinac setting.

Initially the Clinac was set to position 1-2 on the W16 jumper Fig B.1 of the PCB board on the Clinac. This setting was changed to the required 2-3 position as seen on the jumpertable provided in Fig B.2.

This change in the jumper settings facilitates the image acquisition even when the Clinac is under the control of Pulse Drop Servo, which is used for varying the dose rate during the dynamic phase of an EDW treatment. Following the change, image acquisition for EDW treatment was enabled.

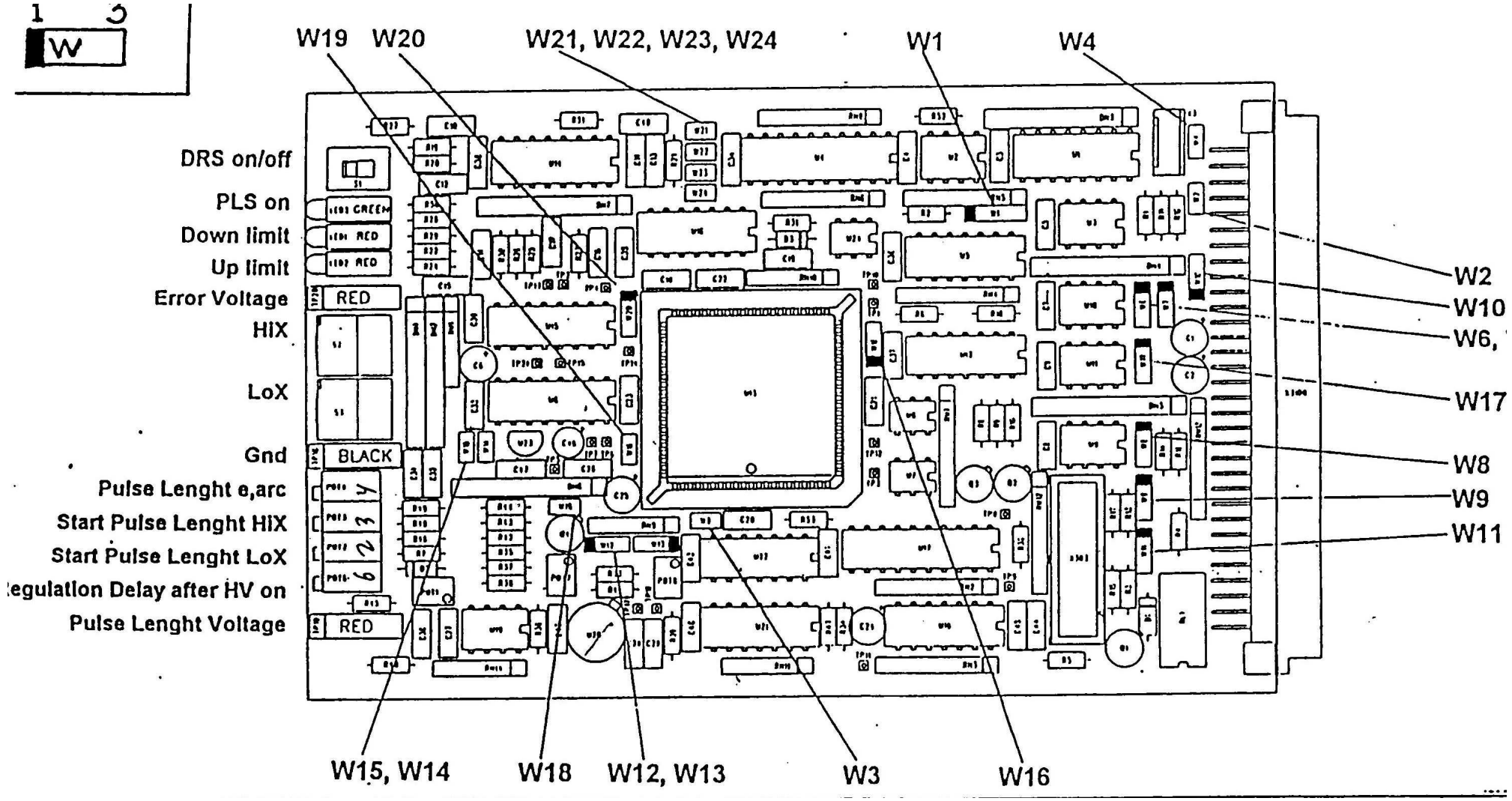
1 3
W
W19
W20
W21, W22, W23, W24
W1
W4
DRS on/off
PLS on
Down limit
Up limit
Error Voltage
HIX
LoX
Gnd
Pulse Lenght e,arc
Start Pulse Lenght HIX
Start Pulse Lenght LoX
egulation Delay after HV on
Pulse Lenght Voltage
GREEN
RED
RED
RED
BLACK
W2
W10
W6,
W17
W8
W9
W11
W15, W14
W18
W12, W13
W3
W16

* Column E applies only for DR step size 100. For step size 80, use column D, 60Hz entries.
\# Column H applies only for DR step size 100. For step size 80, use column G, 60Hz entries.
$ Column J, K, L (Clinacs 4/10MV): DR at Lo-X (4MV) is step size 50, max. 250MU/min.
Ψ Column J (Clinacs 4/10MV S/W Rel. 4): Rep Rates 2 (50) to 6 (250) for Lo-X only.

			A	B	C	D	E *	F	G	H #	J Ψ	K	L
Clinac Type:			18 20	1800 2500	C	C	**C/D**	C	C	C/D	C	C	C/D
Special Energies [MV]:								6/10	6/10	6/10	4/10	4/10	4/10
Clinac S/W Rel.:			N/A	N/A	2/3/5	3/4/5	**3/4/5**	2/3/5	4/5	4/5	4	5	5
DR:	Lo-X: Step Size:		100	80	80	80	**100**	80	80	100	50$	50$	50$
	Hi-X: Step Size:										80	80	100
	Lo-X: Max.:		500	400	400	400	**600**	400	400	600	250$	250$	250$
	Hi-X: Max.:										400	400	600
60Hz Supply:	Sync Hi-X:		180	180	180	180	**180**	360	360	360	360	360	360
	Sync Lo-X:		360	360	360	360	**360**				400	400	400
50Hz Supply:	Sync Hi-X:		150	150	150	180	**180**	300	360	360	360	360	360
	Sync Lo-X:		300	300	300	360	**360**				400	400	400
Function:		**Control:**	**Settings:**										
SVEN		W1	1-2	1-2	3-4	3-4	**3-4**	3-4	3-4	3-4	3-4	3-4	3-4
GND		W2	On	On	Off	Off	**Off**	Off	Off	Off	Off	Off	Off
HOLD		W3	Off	Off	Off	Off	**Off**	Off	Off	Off	Off	Off	Off
PFNSERVO		W4	Off	Off	Off	Off	**Off**	Off	Off	Off	Off	Off	Off
PLSITB		W6	1-2	1-2	2-3	2-3	**2-3**	2-3	2-3	2-3	2-3	2-3	2-3
GPRF		W7	1-2	1-2	2-3	2-3	**2-3**	2-3	2-3	2-3	2-3	2-3	2-3
CENTIMU		W8	1-2	1-2	2-3	2-3	**2-3**	2-3	2-3	2-3	2-3	2-3	2-3
ACQEN		W9	1-2	1-2	2-3	2-3	**2-3**	2-3	2-3	2-3	2-3	2-3	2-3
HVON		W10	1-2	1-2	2-3	2-3	**2-3**	2-3	2-3	2-3	2-3	2-3	2-3
HVON		W11	1-2	1-2	2-3	2-3	**2-3**	2-3	2-3	2-3	2-3	2-3	2-3
HE DIVIDER		W13	1-2	1-2	1-2	1-2	**1-2**	2-3	2-3	2-3	2-3	2-3	2-3
LE DIVIDER		W12	1-2	1-2	1-2	1-2	**1-2**	1-2	1-2	1-2	2-3	2-3	2-3
PVEN		W16	2-3		2-3		2-3	2-3		2-3	2-3		2-3
DRSEN		W17	1-2	1-2	2-3	2-3	**2-3**	2-3	2-3	2-3	2-3	2-3	2-3
60Hz Hi-X:	INC	W21	On	Off	Off	Off	**On**	Off	Off	On	Off	Off	On
	DEC	W23	Off	On	On	On	**Off**	On	On	Off	On	On	Off
	+ 16	W14	Off	On	On	On	**Off**	On	On	Off	On	On	Off
	HEX	S2	7	4	4	4	7	4	4	7	4	4	7
60Hz Lo-X:	INC	W22	N/A	Off	Off	Off	**On**	Off	Off	On	Off	Off	Off
	DEC	W24	N/A	On	On	On	**Off**	On	On	Off	On	On	On
	+ 16	W15	N/A	On	On	On	**Off**	On	On	Off	On	On	On
	HEX	S3	N/A	4	4	4	7	4	4	7	E	E	E
50Hz Hi-X:	INC	W21	On	Off	Off	Off	**On**	Off	On	On	Off	Off	On
	DEC	W23	Off	Off	Off	On	**Off**	Off	Off	Off	On	On	Off
	+ 16	W14	On	On	On	On	**Off**	On	Off	Off	On	On	Off
	HEX	S2	4	N/A	N/A	4	7	N/A	7	7	4	4	7
50Hz Lo-X:	INC	W22	N/A	Off	Off	Off	**On**	Off	On	On	Off	Off	Off
	DEC	W24	N/A	Off	Off	On	**Off**	Off	Off	Off	On	On	On
	+ 16	W15	N/A	On	On	On	**Off**	On	Off	Off	On	On	On
	HEX	S3	N/A	N/A	N/A	4	7	N/A	7	7	E	E	E
4/10MV Offset:		W18	Off	Off	Off	Off	**Off**	Off	Off	Off	On	Off	Off
4/10MV:		W19	Off	Off	Off	Off	**Off**	Off	Off	Off	On	Off	Off
4/10MV:		W20	1-2	1-2	1-2	1-2	**1-2**	1-2	1-2	1-2	2-3	1-2	1-2

Figure B.2: Jumper table

Appendix C

Linear accelerator & enhanced dynamic wedges

C.1 Introduction

In this chapter we will discuss the beam production and modification. As mentioned in the previous chapter the radiation beam is produced by linear accelerators which has been contracted to the term 'linac'.

Linac is a device that uses high-frequency electromagnetic waves to accelerate charged particles such as electrons to high energies through a linear tube. The evolution of linac was a direct consequence of radar development work that resulted in production of microwave generators in the form of magnetrons and klystrons. These devices are capable of establishing intense electromagnetic fields in microwave cavities. This enables for acceleration of electrons to relativistic velocities when incorporated with suitable waveguide structures [55, 56, 57].

C.2 General overview

The block diagram (Figure C.1) shows major components and auxiliary systems of a medical linear accelerator. DC power is supplied to the *modulator* via a power supply. The modulator includes the *pulse-forming network* and a switch tube known as *hydrogen thyratron*. High-voltage pulses from the modulator section are flat-topped DC pulses of a few microseconds in duration. These pulses are delivered to the microwave source: *magnetron* or *klystron* and simultaneously to the electron gun [59].

Pulsed microwaves from the magnetron or klystron are injected into the accelerator tube or structure via a waveguide system. At the proper instant, electrons produced by an *electron gun* are also pulse injected into the *accelerator structure*. The accelerator waveguide consists of a copper tube with its interior divided by copper discs or diaphragms of varying aperture and spacing. This section is evacuated to a high vacuum. As the electrons are injected into the accelerator structure with an initial energy of about 50 keV,

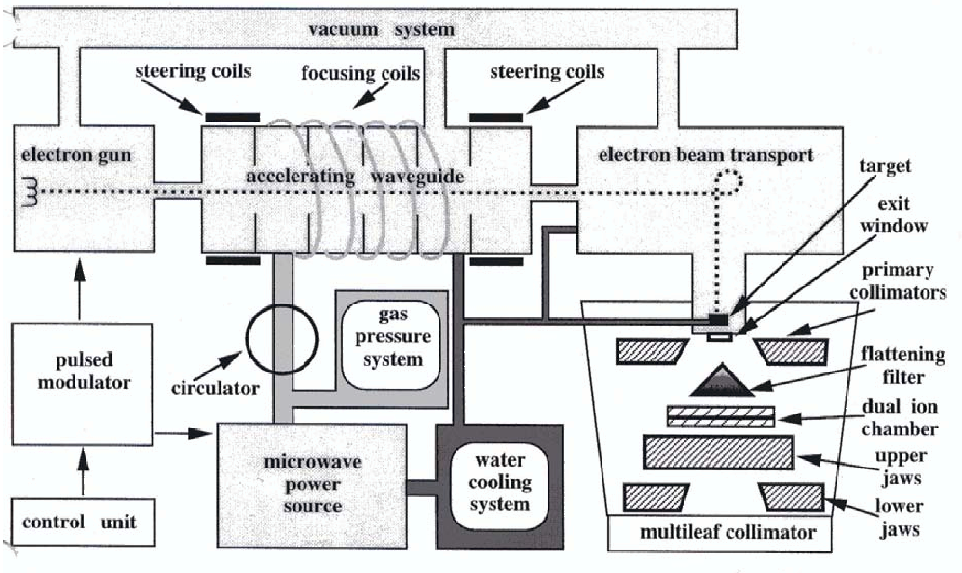

Figure C.1: Major components and auxiliary systems of linear accelerator [58]

the electrons interact with the electromagnetic field of the microwaves. The electrons gain energy from the sinusoidal electric field by an acceleration process. As the high energy electrons emerge from the exit window of the accelerator structure, they are in the form of a pencil beam of about 3mm in diameter.

C.2.1 Target and flattening filter

A broad x-ray beam is produced from the narrow electron beam by bremsstrahlung production in a target (usually made of copper) shown in Figure C.2. This high x-ray beam emerging from the target has fluence, energy and angular distributions; are forward peaked in a bullet-shaped lobe that is further collimated by a fixed primary collimator. The x-ray dose profile is flattened by a flattening filter. This filter is cone shaped with the point of the cone facing the target. The design helps creating a uniform beam. Flattening filter is made either of tungsten, steel or a lead/steel combination.

If the patient requires electron treatment, instead of x-rays, the target and flattening filters are replaced by an electron scattering foil. The target is retracted during the change of mode from x-rays to electrons, the flattening filter is driven out of the beam, the foil is placed in the beam path, and the beam gun current is significantly reduced. The flattening filter and electron foils generally sit below the target on a circular mechanism, which is referred to as the *carousel*. These motions are usually pneumatically controlled and driven into position. All these operations are monitored and interlocked to ensure that the correct programming is achieved [55]. Useful treatment beam emerges from the

Figure C.2: Target

radiation head (often called treatment head). The characteristics of the x-ray and electron treatment beams are strongly influenced by the design of the radiation head. The characteristics that significantly influence radiation treatment are often assessed from the central axis depth dose and isodose curves of x-ray and electron treatment fields [59].

A representative radiation head design is illustrated in Figure C.3. This is a layout used by Varian high-energy dual modality family of linacs, which are capable of producing x-ray and electron beams. The head houses a number of beam-shaping, localizing and monitoring devices. They include bending magnet, fixed shielding, the x-ray target, flattening filter, a series of scattering foils, often mounted on a large carousel, and finally large movable collimator jaws. Also included in the radiation head are a field light with a sizable mirror for illumination up to a full field size and an optical distance indicator, parallel plate, transmission type ionization chamber assembly for monitoring of the full field for control, and interlocking [60].

There are other important component systems and auxiliary support systems that are critical to linac function. The auxiliary support systems of the linac consists of:

- A water cooling system to regulate the temperature of linac components e.g bending magnet
- A vacuum ion pump system to provide vacuum for accelerating waveguide
- An air pressure system for pneumatic drives, e.g., target
- A gas system to improve the dielectric strength of the transmission waveguide.

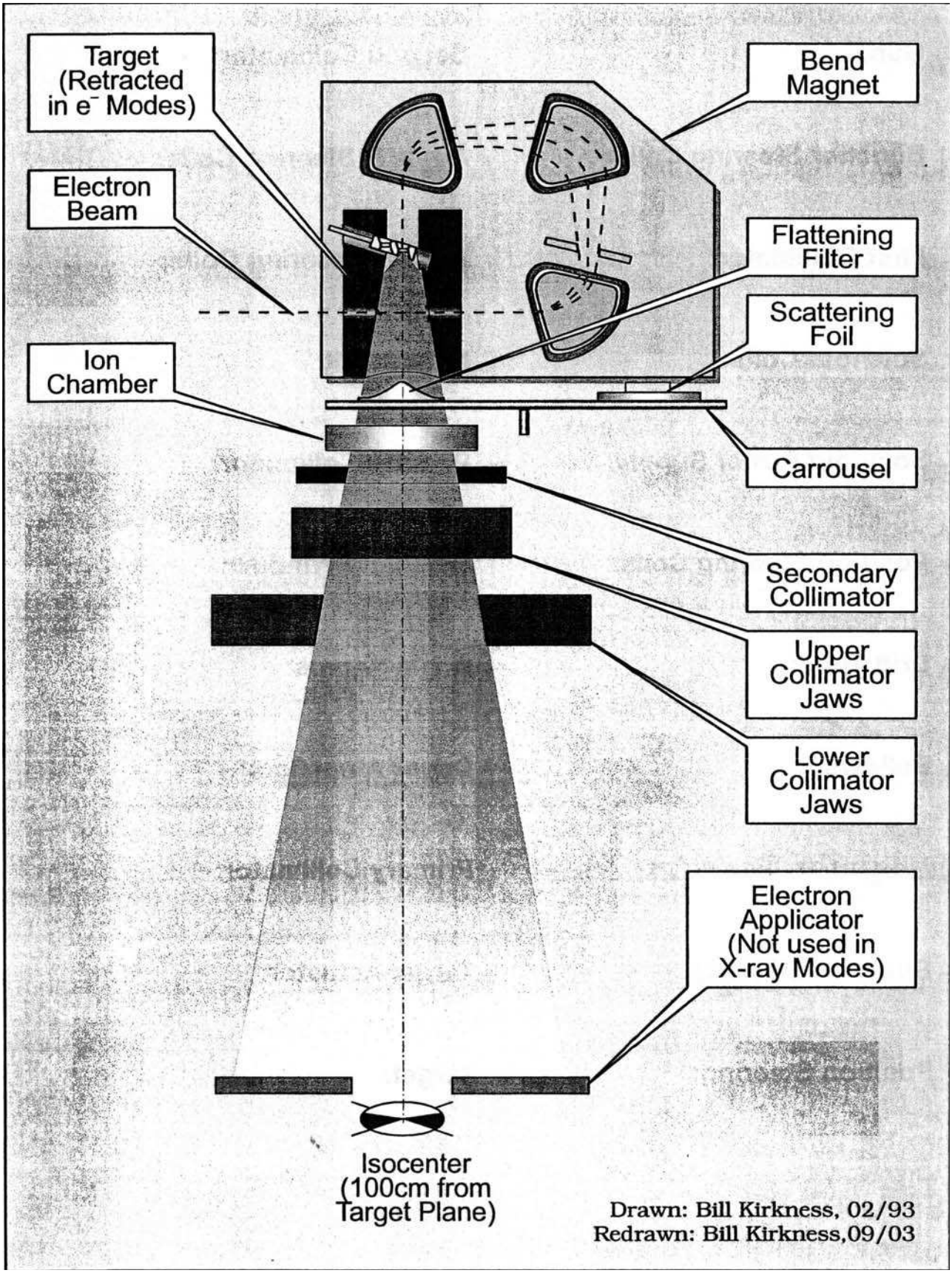

Figure C.3: Beam definition system [60]

C.3 Beam dosimetry

Linear accelerators beam dosimetry system monitors the useful beam of radiation and displays readings related to the dose, dose rate and uniformity (symmetry). The dose monitoring system of a contemporary high-energy linac incorporates a transmission ionization chamber. The transmission chamber is constructed of several plates or electrodes. The areas of these parallel plates are divided into sectors to serve two different monitoring purposes:

- dosimetry of the x-ray and electron treatment beams, and
- monitoring of the intensity distribution of the radiation field.

The resulting signals are fed to the automatic feedback circuits to steer the beam through the accelerator, bending magnet and onto the target in order to ensure beam flatness and symmetry.

Reproducible delivery of the prescribed dose to for each patient is vital to radiation therapy. This is achieved routinely by one set of monitor ionization chamber plates (the inner plates). These are used to monitor dose output. The units of dose recorded by these plates are referred to as monitor units (MU); one MU of dose has been delivered when the monitor chambers have detected a pre-calibrated dose. Because these chambers are located above the final beam collimation system, a MU setting is calibrated to a standard dose for a standard field size [55, 59, 60].

The two dose channels are completely independent, either can terminate the preset exposure. The second channel lags the first by a small margin and serves as a back-up to ensure that if the primary channel fails this will terminate dose. A timer further regulates the dose by terminating the beam at a preset time. This ensures that the treatment will terminate due to a time interlock if both ionization chambers fail.

C.3.1 Beam control

In the 21EX the injector current is rapidly switched off using the grid in the triode gun. The microwave system and injector are operated at a constant PRF. At nominal max dose rate of 600 MU/min, this yields approximately 0.03 and 0.06 MU/pulse for low-X, and high-X, respectively. The injected pulse timing is either made coincident or delayed with respect to the RF pulse timing in order to control the dose rate pulse-to-pulse basis. During the delayed injector pulse periods, dark current is suppressed by the focussing

solenoid that encloses the accelerator. Dose rate is selected by delaying some or all of the pulses in a 6-pulse train. Maximum dose rate is achieved when all 6 of the pulses in the train are coincident. The dose rate servo functions by delaying pulses based on dosimetry data during a 50-mSec control window. Once the proper dose has been recorded during a control window, the remainder of the injector pulses are delayed for that window [60]. There are three different dose rate servos (DRS):

- Pulse Drop Servo (PDS).
- Pulse Length Servo (PLS)
- Pulse Frequency Servo (PFS).

These servos used by Varian clinacs and their purpose will be discussed in the chapter 3.

C.4 Beam collimation

A number of devices are used to collimate and modify the intensity of the beam. The treatment head provides two treatment beam collimators for x-rays as shown in fig C.3. A fixed primary collimator, and an adjustable secondary collimator. Various other devices such as blocks, compensators, multileaf collimators, wedges etc are used to account for the contours of a patient's anatomical structures, to compensate for the missing tissue and also to shield the organs at risk and healthy tissue. These devices collimate and modify the intensity of the x-ray beam and are hence known as *beam modifiers*. Tungsten is the material of choice for both primary and secondary collimators. Space is at a premium in this location and tungsten collimators take up less space than lead. Also, where the x-ray energy is high enough for neutron production, tungsten attenuates the neutrons to a much lower energy than does lead [55, 59].

C.4.1 Primary collimators

A primary fixed collimator is mounted below the target and above the flattening filter. These are slightly diverging cone shaped, open at both ends. This device allows only forward scattered x-rays to escape the linac. The primary beam collimator defines the maximum angular spread of the x-ray beam. The dimensions of this collimator are generally such that in absence of secondary collimators a circular beam of approximately 50cm diameter would be incident at 100cm SSD [55, 59].

C.4.2 Secondary collimators

Secondary collimators are also termed as beam limiting device or 'jaws'. These adjustable collimators consist of two pairs of jaws of about 8cm thickness. The transmission through the jaws is about 0.4% of the dose due to the unshielded incident beam. The jaws are designed so that they drive at an angle to the beam traversing an arc such that the angle closely matches the angle of beam divergence at different field sizes. This ensures that the inner faces are parallel to the edge of the x-ray beam or approximately tangential to the x-ray beam emanating from the x-ray target thereby reducing the penumbra.

The collimators are mounted at a source to collimator distance (SCD) of about 40cm. Because of the thickness of the collimator one set is mounted above the other. This appears to have negligible effect on beam dose profiles. In normal use, each pair of jaw is coupled to provide symmetric rectangular fields from 0 cm to 40cm centered about the axis. The light field that is illuminated to represent the radiation field or the field opened by these collimators needs to be coincident. This coincidence needs to be verified routinely. Hence a test called 'Coincidence of light field vs radiation field' is performed to monitor these fields. The collimators are also able to rotate around the beam's central axis; this is referred to as collimator rotation. They act in combination with the electron applicator to produce a properly shaped electron treatment field dose distribution. [55, 59].

C.4.3 Asymmetric collimators

Modern linacs have independent drives for each set of jaws , which enables definition of asymmetric fields desirable in some treatment techniques. This simplifies the abutment of adjacent fields with negligible field overlap but necessitates precise patient positioning and accurate jaw calibrations. Hence a comprehensive QA test to verify the correct jaw positions and calibration of jaws in asymmetric mode needs to be performed. A test called 4-Quadrant test or Split Field test is very sensitive to changes in the above parameters and hence is a good verification. This test will be described later and a method to perform the test using EPID to replace films will be studied.

C.4.4 Wedge filters

Wedges are variable thickness absorbers that are placed in the beam and cause a progressive decrease in dose intensity across the beam. This results in tilting of isodose curves under normal beam incidence. Three types of wedge filters are in use. Physical wedges, motorized wedges and dynamic wedges.

Physical wedges

Physical Wedges are angled blocks of brass, lead or steel that are placed in the beam at a distance of 40cm from the source. These reduce the beam transmission (attenuation) producing a gradient in the radiation beam intensity. The physical wedges need to be placed on the treatment machine manually, hence intervention is required each time.

Motorized wedges

A motorized wedge is similar to a physical wedge, but is integrated into the treatment head and is sometimes called an internal wedge or a flying wedge. These wedges are driven into the field for part of the treatment and are controlled remotely. The dynamic movement of the wedges produces the resultant dose distributions similar to the physical wedge but determined by the time the wedge is retained in the beam in relation with the open beam. This enhances the capability of wedges, enabling multiple wedge angles.

Dynamic wedges (DW)

The fundamental principle of wedged dose distribution and angled isodose curves remains the same. The key difference between the motorized wedge and a dynamic wedge is movement of jaws. The motorized wedge is an external block of lead that is controlled remotely whereas a dynamic wedge is the sweeping motion of a collimator jaw across the beam. Dynamic wedges are capable of creating multiple number of wedge angles without any apparent beam hardening.

The resultant dose distribution is accrued over time of the treatment, hence limiting the use of point dose measurements using ionization chambers. For sufficient collection of dose profile data, point-by-point acquisition is time consuming therefore film dosimetry or multiple detector arrays are used till date to analyze dynamic wedge profile data. We have explored the possibility to use the electronic portal imager to do the same, as it is convenient and has the potential to acquire dose. However, the system was initially disabled to acquire images for varying dose rates. The following section details the working of Enhanced Dynamic Wedges (EDW) and the varying dose rates.

C.5 Enhanced Dynamic Wedges (EDW)

The enhanced dynamic wedge (EDW) is a Varian trade name for a clinac treatment modality to deliver wedge-shaped photon dose distributions. This modality uses computer-

Table C.1: Key differences between physical, dynamic and enhanced dynamic wedges (Reproduced from [61]

	Physical Wedge	Dynamic Wedge	Enhanced Dynamic Wedge
Asymmetric field sizes	allowed	not allowed	allowed
Wedge Angles	15°, 30°, 45°, 60°	15°, 30°, 45°, 60°	10°, 15°, 20°, 25°,30°,45°, 60°
Field Width Limits	20 (15)cm for 15°, 30°, 45°(60°)	20cm	30cm
Wedge Directions	In, Out, Left, Right	Y1-In, Y2-Out	Y1-In, Y2-Out
Wedge Factors	smooth and nearly constant	smooth and nearly constant	smooth
STT-Tables		132 per photon energy	1 per photon energy

controlled dose delivery combined with upper jaw motion. The wedged dose profiles are created by the sweeping motion of the collimator jaw from open to closed position during the beam on time. The dose deposited during the sweeping jaw motion is integrated to create a wedged isodose profile. Since the jaw motion exposes different parts of the fields to the primary beam for different lengths of time a wedged dose gradient is produced across the field [61].

C.5.1 General capabilities

Enhanced Dynamic Wedges have proven to be a very convenient and elegant alternative of physical wedges. As these provide the capability for symmetric and asymmetric fields of up to 30cm wide(20cm off-axis in the heel and 10cm off axis in the toe direction of EDW) fig C.6 . In addition to allowing multiple wedge angles, these give an effective wedge factor which is smooth and continuous function of field size. Enhanced dynamic wedges give a lower peripheral dose as compared to the physical wedges, resulting in lower dose to surrounding healthy tissue or sensitive structures. Use of EDW also eliminates the beam hardening effects which are known to be common with physical wedges.

Wedge Angle Definitions

Physical Wedge Definition: The nominal wedge angle is defined as the angle through which the 80% isodose contour has been turned at the central axis. The 80% isodose

contours varies in depth between 5 and 10cm, depending on the x-ray energy. Because the isodose contours of a physical edge are curved, this is generally interpreted to mean the tangent to the isodose contour at central axis. [61]

The present physical wedges are optimized to produce the desired nominal wedge angle at the largest field size that the wedge covers (20cm for the 15°, 30°, and 45° wedges and 15cm for the 60° wedges).

Table C.2: Key Differences in wedge angle definition

	Enhanced Dynamic Wedge	Physical Wedge
Depth	Fixed depth of 10cm	Variable depth of 80% isodose contour
Wedge Angle	Line drawn through two points a quarter of a field size on either side of central axis which lie on the isodose contour that intersects the central axis at a 10cm depth	Tangent to the 80% isodose contour on central axis

Enhanced Dynamic Wedge Definition: The wedge angle definition for enhanced dynamic wedges follows IEC Report 976 and ICRU Report 24 Fig C.4 is used to illustrate the key differences between the two and the definition used for enhanced dynamic wedge feature. [61]

C.5.2 Wedge factors

The wedge factor is defined as the ratio of dose at a specified depth (usually Z_{max}) on the central axis with the wedge in the beam to the dose under the same conditions without the wedge. This factor is used in monitor unit calculations to compensate for the reduction in beam transmission produced by the wedge. The wedge factor depends on depth and field size.

The EDW factors appear to be independent of the non-wedged field dimension (X dimension) [62]. They are also found to be machine-independent [63]. Unlike DW, where a strong non-monotonic field size dependence appears [64], the EDW effective wedge factors show a smooth and continuous decrease with increasing field size. Figure C.5 illustrates the measured and calculated effective wedge factors versus square field size and wedge angle [53].

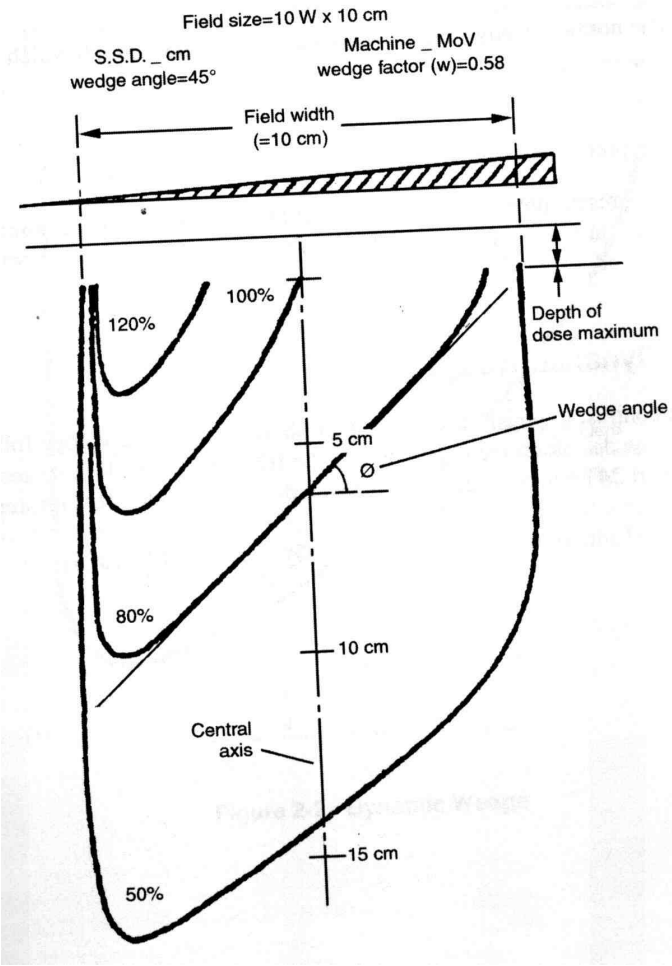

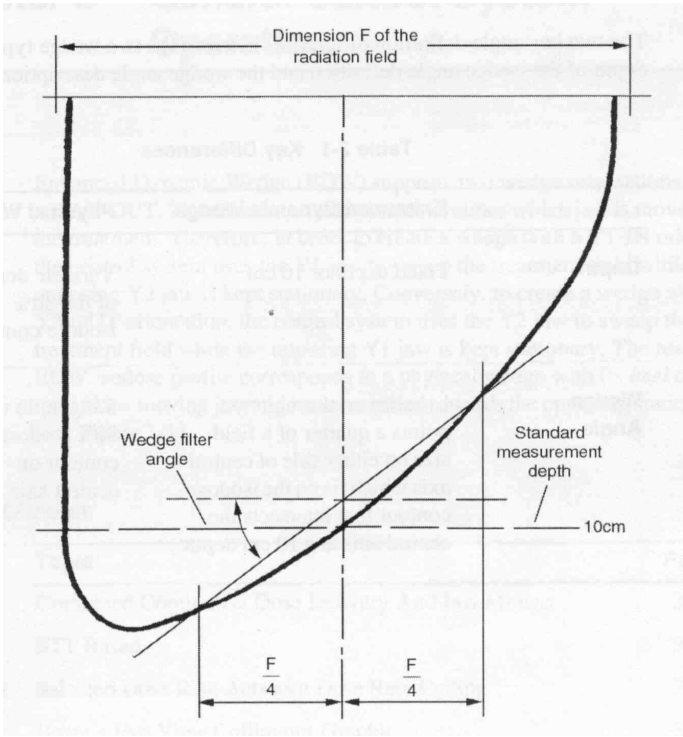

Figure C.4: Physical wedge & dynamic wedge

Since EDW central axis depth dose is practically identical to that of the open field, the effective wedge factor can be considered as independent of the depth as well. Thus, the effective wedge factor can be introduced as a normalization factor characterizing the output for the EDW, which is extremely useful for quality assurance [53].

C.6 EDW treatment summary

An EDW treatment progresses completely under computer control. A pre-calculated pattern that prescribes the dose distribution determines the dose delivered and jaw movements. EDW supports two wedge orientations: Y1-IN and Y2-OUT. The user selects the orientation required which determines which jaw is moved during the treatment. The resulting EDW isodose profile corresponds to a physical wedge with its *heel* oriented towards the moving jaw (Fig C.6) and its *toe* oriented towards the opposing stationary jaw.

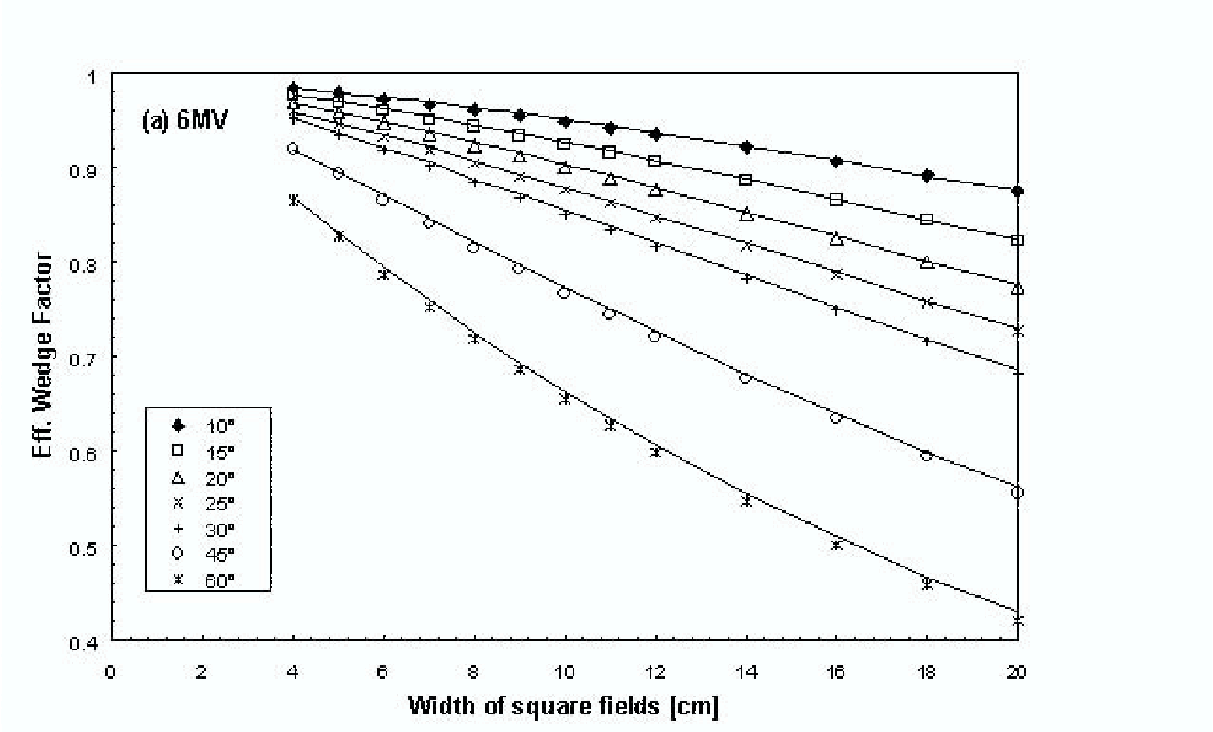

Figure C.5: Calculated and measured effective wedge factors versus square field size for all seven wedge angles for 6MV photons [53]

Computer control ensures that both dose rate and jaw speed are modulated according to the dose versus jaw position table referred to as *Segmented Treatment Table (STT)*. Each STT contains information on the moving jaw position versus cumulative weighting of monitor units which uniquely determines the dose profile. One reference STT is needed per photon energy. This reference STT corresponds to the full field width of 30cm and a wedge angle of 60° and is referred to as the 'Golden' STT because all other field sizes and wedge angles can be derived from this STT.

C.6.1 STT generation

STT generation begins when all the following parameters required for the calculation are entered by the operator.

- Energy
- Monitor Units
- Wedge Orientation
- Field Size

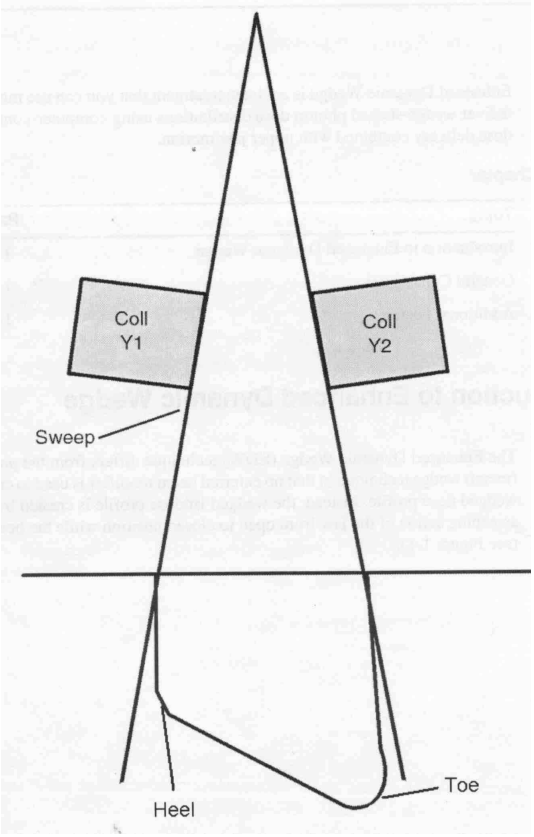

Figure C.6: Jaw sweeping action [61]

- Wedge Angle

STT generation consists of five steps which are represented in the flow diagram (Figure C.8)

STT's of other wedge angles Q can be derived by weighted averaging of the 'open field STT' and the Golden STT. The weights are calculated [53] by using the ratio of tangents method:

$$STT_{\Theta} = (1 - \frac{tan\Theta}{tan60^{\circ}}) \cdot STT_{0^{\circ}} + \frac{tan\Theta}{tan60^{\circ}} \cdot STT_{60^{\circ}} \tag{C.1}$$

The resulting STT is then truncated to the actual field size and normalized so that the final dose is the total dose delivered at the end of the treatment.

An EDW treatment consists of two phases: an open field phase and a jaw sweep phase.

Open field phase

Most EDW treatments start with jaws being stationary before starting to sweep the field. A fraction of the dose is delivered to the full field at this static phase of jaws. This portion

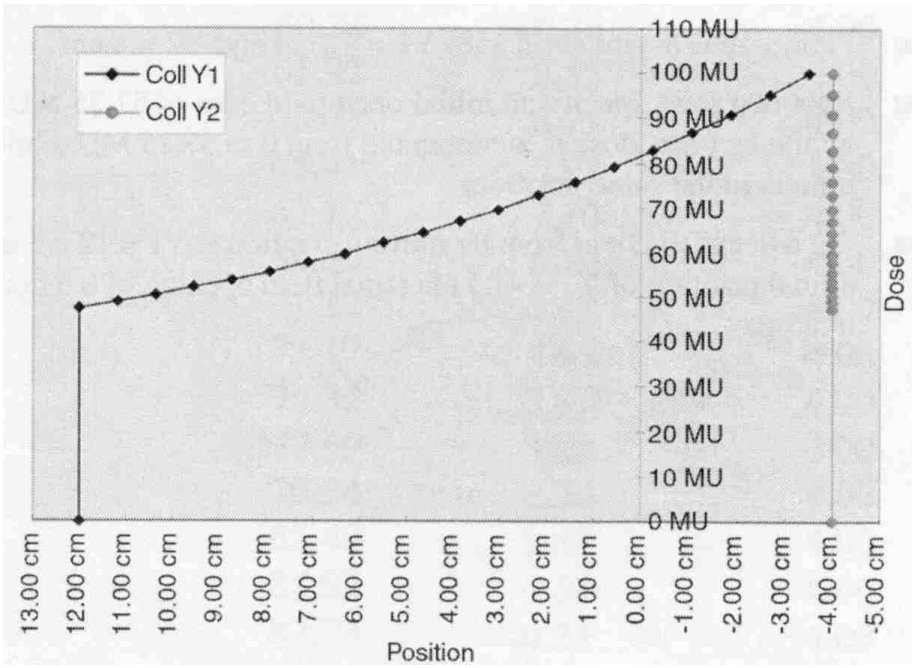

Figure C.7: Graphical representation of an STT [61]

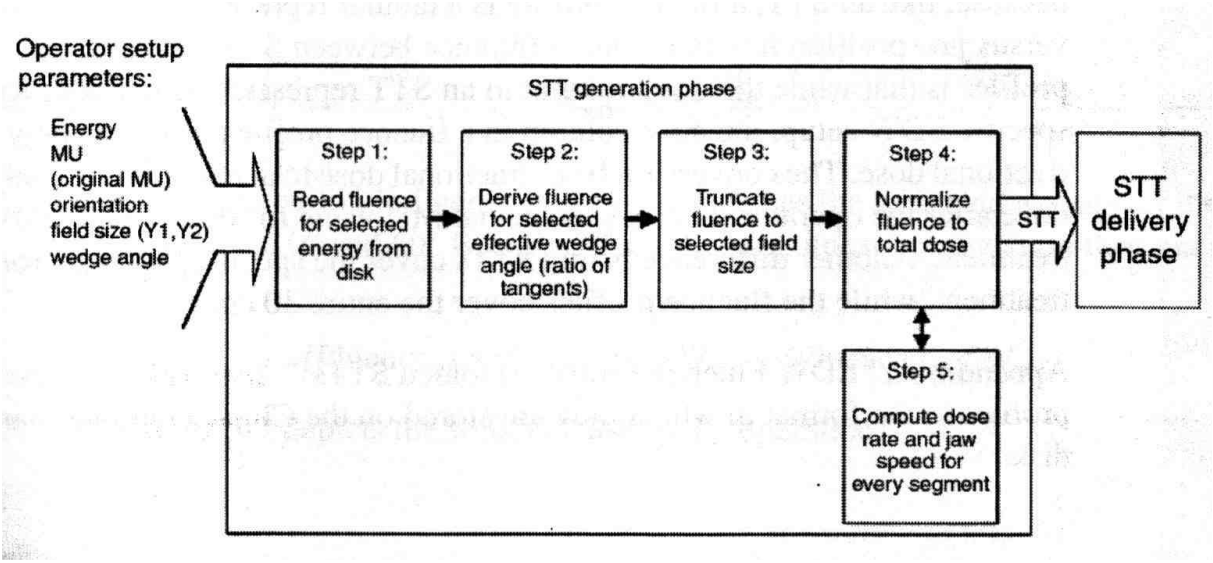

Figure C.8: STT generation [61]

of the treatment is referred to as open field phase of the treatment.

During the open field phase the dose rate is constant and equals the dose rate selected by the operator for the treatment [61]. Hence this phase is carried out under the control of the Pulse Length Servo (PLS). Pulse Length Servo has been explained in detail Chapter 3.

The dose delivered during the open field phase can be described by the following equation [63]. Assuming that a total of K MU is delivered by the EDW, then part of MU $\mathrm{K_{open}}$ to be delivered with the jaws in the fully open position is given as:

$$K_{\mathrm{open}} = \frac{K \cdot N(Y_0)}{N(Y_{\mathrm{FIN}})} = D_{max} \cdot T_0, \tag{C.2}$$

where $\mathrm{Y_0}$ is the initial moving jaw position, D_{max} is the maximum dose rate, and $\mathrm{T_0}$ is the length of irradiation time during which the moving jaw is fully open.

Dynamic phase or jaw sweep phase

Following the delivery of the open field phase of the beam, the jaw starts sweeping the field to move towards the stationary jaw. The treatment is always finished with 0.5cm as the final field size at the end of the sweep. This phase is aptly named as dynamic or jaw sweep phase of the treatment. During the dynamic phase the jaw initiates motion usually at its maximum speed, while the dose rate is reduced. As the sweep progresses, the jaw speed is typically reduced and the dose rate gradually increases, but never exceeds the selected dose rate. The dynamic phase is governed by the Pulse Drop Servo as dose rate modulation is required [61].

The remaining MU after the open field phase are delivered by the following rules on the Varian EDW :

- A constant speed applies between each segment;
- if possible, a maximum speed, V_{max}, will be used for the moving jaw while the dose rate varies according to the NGSTT; and
- if the EDW requires the maximum dose rate D_{max}, D_{max} will be used, and the speed of the moving jaw will be reduced to V [61] according to the following equation:

$$\frac{K \cdot (N(Y_{i+1}) - N(Y_i))}{N(Y_{FIN})(Y_{i+1}Y_i)} = \frac{D_{max}(Y_{i+1})}{V(Y_{i+1})}, if D(Y_{i+1}) = D_{max}, \tag{C.3}$$

where Y_i is the i^{th} segment of the moving jaw position described in the NGSTT. The time travelled during each segment, T_i, is

$$(Y_{i+1} - Y_i) = V(Y_{i+1}) \cdot T_i. \tag{C.4}$$

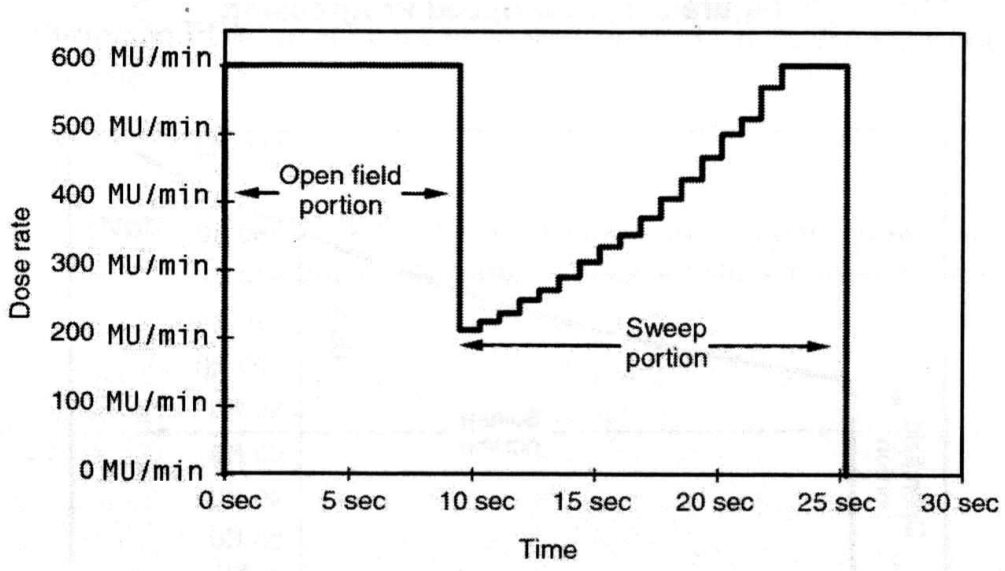

Figure C.9: Dose Rate Progression [61]

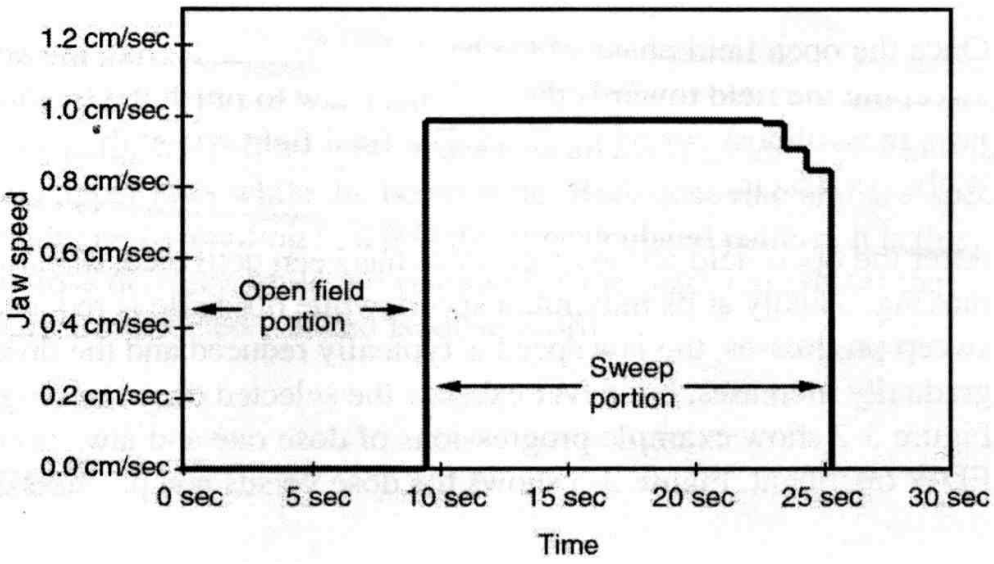

Figure C.10: Jaw speed progression [61]

An important point to note for an EDW treatment is that the operator set dose rate acts as a Dose Rate Ceiling and cannot be viewed as an absolute dose rate due to the dose rate modulation necessary for the EDW treatment. This modulation does not directly affect the dose distribution, nor does the jaw speed and acceleration. The only significant parameter from a clinical perspective is the dose delivered versus jaw position relation which is enforced by the control system. This relationship governs the resulting wedged

isodose profile as long as the system adheres to the predefined calculations [61].

C.6.2 Jaw velocity, dose rate and treatment time

The dose rate and jaw speed for each segment is individually calculated by the control system such that the segment is delivered in the shortest possible time. The treatment time can be minimized by choosing the maximum jaw velocity for each field segment that allows delivery of the required monitor units within that segment. Thus in segments requiring small number of monitor units to be delivered maximum jaw velocity is set, while the set dose rate is less than the maximum you select. For segments requiring a large number of monitor units, a slower jaw velocity is set, while the set dose rate is changed to the maximum you select [61].

C.6.3 Continuous dose delivery

The STT specifies dose and position at discrete points which are connected by line segments to represent the true dose versus jaw position path. The control system enforces a linear progression of dose and position from one STT row to the next. All EDW STT's are generated with 20 segments regardless of the field size. The continuous method of the motion makes this more than adequate to specify a precise dose versus jaw position path. In effect STT rows are needed only to describe inflection points. For each segment the dose rate and jaw speed are calculated so that either the dose rate or the jaw speed are at maximum resulting in the shortest possible treatment time. For a particular dose to target volume, the treatment time for EDW is usually shorter than the time required to deliver the same dose using a physical wedge.

The operator selected wedge angle, field size, total monitor units, and beam energy determines the exact progression of dose rate and jaw speed. These factors also determine the total dose to be delivered as an open field.The dose rate and jaw speed to be used is calculated at each point before the treatment starts. Hence the progression of dose rate and jaw speed is always determined and follow the same precalculated pattern for the same EDW setup. (that is for the same beam energy, monitor units, wedge angle and field size) [61].

C.7 Electronic Portal Imaging Device (EPID)

Early studies based on port films indicated the benefits of portal verification for accurate day-to-day treatment set-up and accurate delivery of treatment to the physical location

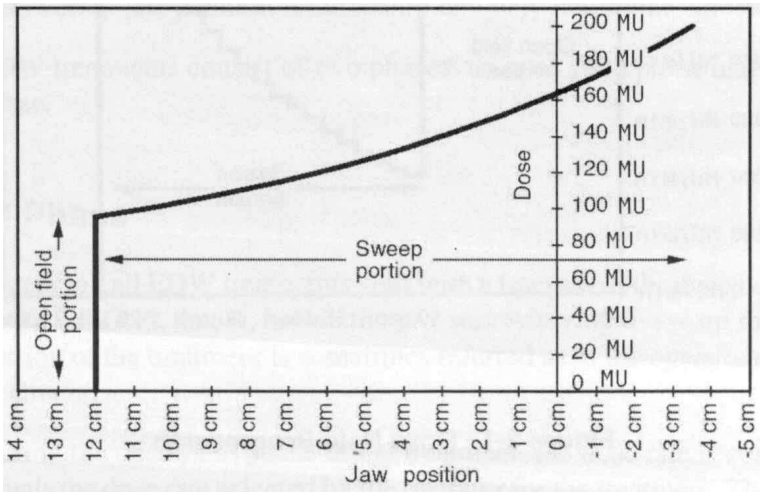

Figure C.11: Dose versus jaw position(Total dose is 200 MU) [61]

as defined by the patient anatomy [5, 6, 7, 65, 66]. Hence, the accepted way to ensure that the physical location of the treatment beam is correct, is to take an x-ray portal view. An x-ray portal is the opening defined by the collimators and blocks through which the beam escapes. By placing a detector array or film on the beam exit side of the patient, a beam's eye view (BEV) of the x-ray portal in relation to the patient's bony landmarks is recorded. The image produced is known as a portal image [55].

Modern linacs now come with an electronic portal imaging device (EPID) as an option. EPID consists of a flat plate detector array placed on the opposite side of the rotating gantry from the treatment beam portal. They are mounted on a retractable arm and designed to replace the historical method of treatment position validation which is to place film in this position [55].

References

[1] J Van Dyk, editor. *The Modern Technology of Radiation Oncology.* Medical Physics Publishing, 1999.

[2] J. R Williams and D.I Thwaites, editors. *Radiotherapy Physics in Practice.* Oxford University Press, second edition, 2000.

[3] M Hulshof, L Vanuytssel, W Van den Bogaert, and E Van der Schuren. Localization errors in mantle-field irradiationn for hodgkin's disease. *Int. J. Radiat. Oncol., Biol., Phys.*, 17:679–683, 1989.

[4] R.A Huddart et al. Accuracy of pelvic radiotherapy: prospective analysis of 90 patients in a randomised trial of blocked versus standard radiotherapy. *Radiother. Oncol.*, 39:19–29, 1996.

[5] I Rabinowitz, J Broomberg, M Goitein, K McCarthy, and J Leong. Accuracy of radiation field alignment in clinical practice. *Int. J. Radiation Oncology Biol., Phys.*, 11:1857–67, 1985.

[6] S.A Rosenthal, J.M Galvin, J.W Goldwein, A. R Smith, and P.H Blitzer. Improved methods for determination of variability in patient positioning for radiation therapy using simulation and serial portal film measurements. *Int. J. Radiation Oncology Biol., Phys.*, 23:621–625, 1992.

[7] J.M Balter, H.M Sandler, K Lam, R.L Bree, A.S Lichter, and R.K Haken. Measurement of prostate movement over the course of routine radiatherapy using implanted markers. *Int. J. Radiation Oncology Biol., Phys.*, 31:113–8, 1995.

[8] J.E Marks, A.G Haus, H.G Sutton, and M. L Griem. The value of frequent treatment verification films in reducing localization error in irradiation of complex fields. *Cancer*, 37:2755–61, 1976.

[9] P Munro, J.A Rawlinson, and A Fenster. Therapy imaging: a signal-to-noise analysis of a fluoroscopic imaging system for radiotherapy localization. *Med. Phys.*, 17:763–72, 1990.

[10] Kruse Jon J. and M.G Herman et al. Electronic and film portal images: A comparison of landmark visibility and review accuracy. *Int. J Radiation Oncology Biol. Phys.*, 54(2):584–591, 202.

[11] O Pradier, A Hille, H Schmidberger, and CF Hess. The role of high-energy imaging in a radiotherapy service and its incorporation in a network. *Cancer Radiotherapy*, 5(3):246–54, Jun 2001.

[12] D Vetterli. Introduction of a novel dose saving acquisition mode for portalvision$^{\text{tm}}$ as500 epid to facilitate on-line patient setup verification. *Medical Physics*, 31(4):828–831, April 2004.

[13] J. Leong. Use of digital fluoroscopy as an on-line verification device in radiation therapy. *Phys. Med. Biol.*, 31:985–992, 1986.

[14] J.W Wong, E.D Slessinger, R.E Hermes, and C.J Offutt et al. Portal dose images i: quantitative treatment plan verification. *Int. J. Radiat. Oncol., Biol., Phys.*, 18:1455–1463, 1990.

[15] X. Ying, L.Y Greer, and J.W Wong. Portal dose images i: patient dose estimation. *Int. J. Radiat. Oncol., Biol., Phys.*, 18:1465–1472, 1990.

[16] V.N Hansen, P.M Evans, and W Swindell. The application of transit dosimetry to precision radiotherapy. *Med. Phys.*, 23:713–721, 1996.

[17] M.C Kirby and P.C Williams. The use of an electronic portal imaging device for exit dosimetry and quality control measurements. *Int. J. Radiat. Oncol., Biol., Phys.*, 31:593–603, 1995.

[18] M.C Kirby and P.C Williams. Measurement possibilities using an electronic portal imaging device. *Radiother. Oncol.*, 29:237–243, 1993.

[19] B.J.M Heijmen and K.L Pasma et al. Portal dose measurement in radiotherapy using an electronic portal imaging device (epid). *Phys. Med. Biol.*, 40:1943–1955, 1995.

[20] K.L Pasma, M.L.P Dirkx, M Kroonwijk, A.G Visser, and B.J.M Heijmen. Dosimetric verification of intensity modulated beams produced with dynamic multileaf collimation using an electronic portal imaging device. *Med. Phys.*, 26:2373–2378, 1999.

[21] Van Esch A, B Vanstraelen, J Verstraete, G Kutcher, and D Huyskens. Pretreatment dosimetric verification by means of a liquid-filled electronic portal imaging device during dynamic delivery of intensity modulated treatment fields. *Radiother. Oncol.*, 60:181–190, 2001.

[22] R.J.W Louwe, L.N McDermott, J.J Sonke, R Tielenburg, M. Wendling, M.B van Herk, and B.J Mijnheer. The long term stability of amorphous silicon flat panel imaging devices for dosimetry purposes. *Med. Phys.*, 31:2989–2995, 2004.

[23] L. E Antonuk, Y El-Mohri, W Huang, K.-W. Jee, J.H Siewersden, M Maolinbay, V.E Scarpine, H Sandler, and J Yorkston. Initial performance evaluation of an indirect-detection,active matrix flat-panel imager prototype for megavoltage imaging. *Int. J. Radiat. Oncol., Biol., Phys.*, 42:437–452, 1998.

[24] Y El-Mohri, L. E Antonuk, J Yorkston, K.-W. Jee, M Maolinbay, K. L Lam, and J.H Siewersden. Relative dosimetry using active matrix flat panel imager (amfpi) technology. *Med. Phys.*, 26:1530–1541, 1999.

[25] M.A Hunt, T.E Schultheiss, G.E Desobry, M Hakki, and G.E Hanks. An evaluation of set-up uncertainties for patients treated to pelvic sites. *Int. J. Radiat. Oncol., Biol., Phys.*, 32:227–33, 1995.

[26] S. Shalev et al. Video techniques for on-line portal imaging. *Comput. Med. Imaging Graph.*, 13:217–26, 1989.

[27] H Meertens, M van Herk, J Bijhold, and H Bartelink. First clinical experience with a newly developed electronic portal imaging device. *Int. J. Radiat. Oncol., Biol., Phys.*, 18:1173–81, 1990.

[28] M.G Herman, R.A Abrams, and R.R Mayer. Clinical use of on-line portal imaging for daily patient treatment verification. *Int. J. Radiat. Oncol., Biol., Phys.*, 28:1017–23, 1994.

[29] F. F Yin et al. An observer study for direct comparison of clinical efficacy of electronic to film portal images. *Int. J. Radiat. Oncol., Biol., Phys.*, 35:985–91, 1996.

[30] V Thompson, M Bidmead, and C. Mubata. Pictorial review: comparison of portal imaging and megavoltage verification films for conformal pelvic irradiation. *Br. J. Radiol. Suppl*, 69:1191–5, 1996.

[31] M Essers, R Boellaard, M van Herk, J.H Lanson, and B.J Mijnheer. Transmission dosimetry with a liquid-filled electronic portal imaging device. *Int. J Radiation Oncology Biol. Phys.*, 34:931–941, 1996.

[32] Van Esch A and D.P Huysken. Qa of imrt planning by means of portal vision. University of Leuven, Department of Radiotherapy and Radiation Physics.

[33] G.V Menon and R.S Sloboda. Compensator quality control with an amorphous silicon epid. *Med. Phys.*, 30(7):1816–1824, July 2003.

[34] Varian Medical Systems. Image acquisition system. Document Library.

[35] J Pouliot and M Aubin. Tutorial on epid. Radiation Onclogy UCSF.

[36] Varian Medical Systems. Portalvision$^{\text{tm}}$ as500 electronic portal imaging device. Brochure, 1999. Specifications.

[37] Varian Medical Systems. *PortalVision*$^{\text{TM}}$ *aS500 System Manual*. Varian medical Systems.

[38] Varian Medical Systems. Portalvision$^{\text{tm}}$ and dosimetry 6.5. Document Library.

[39] L. N McDermott, R.J.W. Louwe, J.-J. Sonke, M.B van Herk, and B.J Mijnheer. Dose-response and ghosting effects of an amporphous silicon electronic portal imaging device. *Med. Phys.*, 31(2):285–295, February 2004.

[40] B.M.C McCurdy and S Pistorius. A two-step algorithm for predicting portal dose images in arbitraty detectors. *Med. Phys.*, 27(9):2109–2116, September 2000.

[41] D.A Jaffray, J.J Battista, and A Fenster. X-ray scatter in megavoltage transmission radiography: Physical characteristics and influence on image quality. *Med. Phys.*, 21(1):45–60, January 1994.

[42] P Greer and Carmen Popescu. Dosimetric properties of an amorphous silicon electronic portl imaging device for transit dosimetry. *Med. Phys*, 30(7):1618–1627, July 2003.

[43] Van Esch A, T Depuydt, and D.P Huysken. The use of asi-based epid for routine absolute dosimetric pre-treatment verification of dynamic imrt fields. *Radiatherapy and Oncology*, 71(2):223–234, May 2004.

[44] B.M.C McCurdy, K Luchka, and Pistorius S. Dosimetric investigation and portal dose image prediction using an amorphous silicon electronic imaging device. *Med. Phys.*, 28(6):911–924, June 2001.

[45] E Grein, R Lee, and K Luchka. An investigation of new amporphous silicon electronic portal imaging device for transit dosimetry. *Med. Phys.*, 29(10):2262–2268, October 2002.

[46] P Winkler, A Hefner, and D Georg. Dose-response characteristics of n amorphous silicon epid. *Med. Phys.*, 32(10):3095–3105, October 2005.

[47] The IRO Medical Physics and Engineering Group (MPEG). Coincidence of light beam with radiation beam. KFJ-MPEG.

[48] P Greer. Assessment of an amorphous silicon epid for quality assurance of enhanced dynamic wedge. EPSM, 2004.

[49] J. P Gibbons. Calculation of enhanced dynamic wedge factors for symmetric and asymmetric photon fields. *Med. Phys.*, 25(8):1411–1418, August 1998.

[50] C Kirby and R Sloboda. Consequences of the spectral response of an asi epid and implications for dosimetric calibration. *Med. Phys.*, 32(8):2649–2658, August 2005.

[51] P. Greer. Correction of pixel sensitivity variation and off-axis response for amorphous silicon epid dosimetry. *Med. Phys.*, 32(12):3558–3568, December 2005.

[52] L Ko, J. O Kim, and J.V Siebers. Investigation of the optimal backscatter for an asi electronic portal imaging device. *Phys. Med. Biol.*, 49:1723–1738, 2004.

[53] J Salk, P Blank, U Machold, E Rau, and Rottinger E.M Scheider, E. Physical aspects in the clinical implementation of the enhanced dynamic wedge.

[54] D. D Leavitt, W. L Lee, D.K Gaffney, J.H Moeller, and J.H O'Rear. Dosimetric parameters of enhanced dynamic wedge for treatment planning and verification. *Medical Dosimetry*, 22(3):177–183, 1997.

[55] Peter Metcalfe, Tomas Kron, and Peter Hoban. *The Physics of Radiotherapy X-rays from Linear Accelerators*. Medical Physics Publishing, 2004.

[56] H. E Johns and John Cunningham. *The Physics of Radiology*. Charles C Thomas, fourth edition, 1983.

[57] Faiz M. Khan. *The Physics of Radiation Therapy*. Lippincott Williams & Wilkins, third edition, 2003.

[58] Review of radiation oncology physics: A handbook for teachers and students. Vienna, Austria, May 2003.

[59] C. J Karzmark, C.S Nunan, and E Tanabe. *Medical Electron Accelerators*. McGraw-Hill, Inc, 1993.

[60] Varian Medical Systems. *High Energy C-Series Clinac Customer Support Course*, July 2004.

[61] Varian Medical Systems. *C-Series Clinac, Enhanced Dynamic Wedge ^{TM}, Implementation Guide*, January 2002.

[62] S.X Chang and J.P Gibbons. Clinical implementation of non-physical wedges. 1999.

[63] C Liu, Z Li, and J Palta. Characterizing output for the varian enhanced dynamic wedge field. *Medical Physics*, 25(1):64–70, January 1998.

[64] Liu, T. C. Zhu, and J Palta. Characterizing output factor for dynamic wedge. *Medical Physics*, 23:1213–1218, 1996.

[65] M.G Herman, J.M Balter, D.A Jaffray, K.P McGee, P Munro, S Shalev, M Van Herk, and J Wong. Clinical use of electronic portal imaging. AAPM Task Group 58, American Association of Physicists in Medicine, May 2001.

[66] J.E Marks, A.G Jaus, H.G Sutton, and M.L Griem. Localization error in the radiotherapy of hodgkin's disease and malignant lymphoma with extended mantle fields. *Cancer (N.Y.)*, 34:83–90, 1974.